Synthesis and studies of transition metal borides and carbides under high pressure

By

A N Arpita Aparajita

PHYS 02 2014 04 002

Indira Gandhi Centre for Atomic Research,

Kalpakkam, India

A thesis submitted to the
Board of Studies in Physical Sciences

In partial fulfillment of requirements
for the Degree of
DOCTOR OF PHILOSOPHY
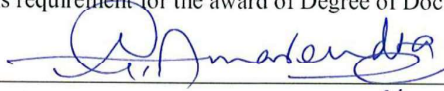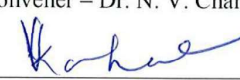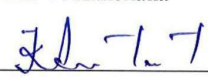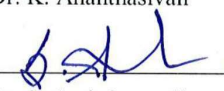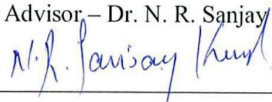
of

HOMI BHABHA NATIONAL INSTITUTE

August, 2019

Homi Bhabha National Institute
Recommendations of the Viva Voce Committee

As members of the Viva Voce Committee, we certify that we have read the dissertation prepared by A N Arpita Aparajita entitled "Synthesis and studies of transition metal borides and carbides under high pressure" and recommend that it may be accepted as fulfilling the thesis requirement for the award of Degree of Doctor of Philosophy.

Chairman – Dr. G. Amarendra   Jan 20, 2020   Date

Guide / Convener – Dr. N. V. Chandra Shekar   20/1/2020   Date

Examiner - Dr. V. Kanchana   Date

Member 1- Dr. K. Ananthasivan   Jan 20, 2020   Date

Member 2- Dr. S. Amirthapandian   Date 20/1/20

Technology Advisor – Dr. N. R. Sanjay Kumar   Date 20/01/2020

Final approval and acceptance of this thesis is contingent upon the candidate's submission of the final copies of the thesis to HBNI.

I hereby certify that I have read this thesis prepared under my direction and recommend that it may be accepted as fulfilling the thesis requirement.

Date: 20/1/2020

Place: IGCAR, Kalpakkam

N.V. Chandra Sh

Signature

Guide

iii

STATEMENT BY AUTHOR

This dissertation has been submitted in partial fulfillment of requirements for an advanced degree at Homi Bhabha National Institute (HBNI) and is deposited in the Library to be made available to the borrowers under rules of the HBNI.

Brief quotations from this dissertation are allowable without special permission, provided that accurate acknowledgement of source is made. Requests for permission for extended quotation from or reproduction of this manuscript in whole or in part may be granted by the Competent Authority of HBNI when in his or her judgment the proposed use of the material is in the interests of scholarship. In all other instances, however, permission must be obtained from the author.

20.01.2020

A N Arpita Aparajita

DECLARATION

I, hereby declare that the investigation presented in the thesis has been carried out by me. The work is original and has not been submitted earlier as a whole or in part for a degree / diploma at this or any other Institution / University.

Arpita 20.01.2020

A N Arpita Aparajita

List of Publications arising from the thesis

Journal

1. Compressibility behaviour of conducting ceramic TiB_2. **A N Arpita Aparajita,** N R Sanjay Kumar, N V Chandra Shekar and S. Kalavathi, Material Research Express **4**, 096508 (2017).

   doi: https://doi.org/10.1088/2053-1591/aa8a8f

2. High-Pressure Synthesis of Manganese Monocarbide: A Potential Superhard Material, **A. N. Arpita Aparajita,** N. R. Sanjay Kumar, Sharat Chandra, S. Amirthapandian, N. V. Chandra Shekar, and Kalavathi Sridhar, Inorganic Chemistry, **57,** 14178-14185 (2018)

   doi: https://doi.org/10.1021/acs.inorgchem.8b02148

3. Bond length anomaly in TiB_2 at high pressure: first principles calculations. G Shwetha, **A N Arpita Aparajita,** Sharat Chandra, N V Chandra Shekar and S. Kalavathi, Material Research Express, **6,** 026531 (2019).

   doi: https://doi.org/10.1088/2053-1591/aaed7b

4. Study of Group 5B Transition Metal Monoborides under High Pressure. **A N Arpita Aparajita,** G. Shwetha, N. R. Sanjay Kumar, V. Srihari, N. V. Chandra Shekar, S. Kalavathi **(under review)**

5. High pressure synthesis of novel chromium carbide. **A. N. Arpita Aparajita,** N. R. Sanjay Kumar, Sharat Chandra, N. V. Chandra Shekar, and S. Kalavathi **(under preparation)**

Conferences

1. High pressure synthesis of novel manganese carbide, **A. N. Arpita Aparajita,** N. R. Sanjay Kumar, S. Amirtha Pandian, N. V. Chandra Shekar, S. Kalavthi, 9th National Conference on Thermophysical Properties, November 6-8, 2017, IGCAR, Kalpakkam.

2. Anomalous bond compression behavior of TiB_2: Experiment and Computation, **A N. Arpita Aparajita,** G. Shwetha, N. R. Sanjay Kumar, N. V. Chandra Shekar, and S. Kalavathi, 2nd International Conference on Condensed Matter and Applied Physics, Nov 24-25, 2017, Govt. Engineering College, Bikaner, Rajasthanm

---

3. Formation of ZnS type MnC using Laser Heated Diamond Anvil Cell, **A N Arpita Aparajita,** N.R. Sanjay Kumar, Sharat Chandra, S. Amirtha Pandian, N. V. Chandra Shekar, and S. Kalavathi, 1st HBNI - Research Scholars Meet on Material Science and Engineering of Nuclear Materials, May 7-9, 2018, IGCAR, Kalpakkam.

Publications not included in the thesis

1. High pressure synthesis of iridium carbide, N R. Sanjay Kumar, **A N Arpita Aparajita** and N. V. Chandra Shekar, Condensed Matter at Extreme conditions April 13-16, 2016, BARC, Mumbai

A N Arpita Aparajita

DEDICATIONS

This thesis is dedicated to my

FAMILY

ACKNOWLEDGEMENTS

TABLE OF CONTENTS

ABSTRACT

Optimized insertion of light elements like boron and carbon to transition metal (TM) lattice to obtain transition metal boride (TMB) and transition metal carbide (TMC) is one of the approaches to get ultraincompresible and superhard materials. Boron readily combines with TMs to form TMBs with stoichiometry ranging from TM_3B to TMB_{12}. With impressive thermomechanical properties and low weight to strength ratio, TMBs find application in energy storage devices, reactors and abrasive industry and, the wide range of stoichiometries provide a fertile ground for exploration. TMBs have a favourable energy of formation and hence are formable using high temperature methods. However, due to degeneracy in formation energy multiphase formation is a problem faced during their synthesis. Among the borides, for stoichiometries like TMB_2 and TM_3B_4, it is seen that the cohesive energy which represents stability, is highest for the 4B elements and decreases along the series. Hence, the group 4B and 5B borides *viz.* TiB_2, VB and TaB were studied under high pressure using high pressure X-ray diffraction (HPXRD) and *ab initio* electronic structure calculation. VB in pure phase was synthesized using arc melting method followed by repeated annealings and, TaB and TiB_2 were procured. All the studied borides were found to be ultraincompresible with bulk modulus more than 300 GPa. Pseudogap which indicates high stability was observed in the density of states (DOS) plots for all of them and they are metallic.

In the case of TiB_2, there is a high spread in the reported bulk modulus i.e. from 193 to 399 GPa. With the result obtained in this work i.e. 333(6) GPa and the reported experimental values for other diborides it was observed that the bulk modulus follows the trend of cohesive energy along *3d* series and 4B group. The lattice was structurally stable up to 23 GPa and *c*-axis was seen to be more compressible compared to *a*-axis showing anisotropic behaviour. A change in rate of bond compression was seen for the Ti-B and B-

B bonds. A significant redistribution of charge along B-B bond and the increase in degree of covalency of Ti-B bond was understood to be the reasons.

The group 5B monoborides VB and TaB were studied and compared. It was seen that TaB is more incompressible with bulk modulus of 366(17) GPa as compared to VB with bulk modulus 301(5) GPa. For both VB and TaB, the lattice was more compressible along the *a*-axis due to predominant presence of metallic bond. VB was least compressible along *b*-axis and TaB along the *c*-axis, which is in accordance with the respective bonds along these directions.

In the case of TMCs, due to lack of balance between strength of TM-C and TM-TM bonds, the carbon rich TMC phases which may show better mechanical properties, are not formable only with application of high temperature. With the objective to synthesize novel superhard materials, manganese monocarbide (MnC) and chromium monocarbide (CrC) were synthesized for the first time using laser heated diamond anvil cell (LHDAC). MnC was found to be a high temperature phase which crystallizes in ZnS structure with lattice parameter 4.4294(2) Å. The bulk modulus was estimated to be 170(5) GPa using HPXRD. Study of DOS and charge density showed that MnC is metallic and the Mn-C bond has a mixture of covalent and ionic nature. Empirical estimation of hardness showed that MnC has potential high hardness. The hardness owes to the short Mn-C bond length, high valency of Mn and the tetrahedral bonds between Mn and C atoms. The structure of CrC was found to be hexagonal with lattice parameters parameter $a = 2.7496(2)$ Å and $c = 8.7010(4)$ Å. The bulk modulus of CrC was estimated to be 269.8 GPa. The hardness of CrC was found to be lower than that of MnC which may be because of the graphite like carbon layers present in the structure. Both MnC and CrC are formable at moderate pressure of 5 GPa and hence, can be synthesized in bulk using belt type or multi-anvil apparatus.

LIST OF FIGURES

LIST OF TABLES

Chapter 1

Transition metal borides and carbides: Equilibrium and non-equilibrium synthesis and study under high pressure

1.1. Introduction

Diamond as a gemstone has fascinated humans for centuries with its lustre and brilliance. But, for a material scientist, this allotrope of carbon is interesting for its highest hardness, wear resistance, resistance in acid, toughness, yield strength, highest thermal conductivity and electrical properties[1]. With the highest hardness (about 100 GPa), it holds the widest application in the abrasive industry. However, apart from being costly, diamond reacts with iron and hence, machining ferrous materials with diamond becomes a problem [2]. Nevertheless, cubic boron nitride (hardness of about 50 GPa) complies for this shortcoming of diamond. Another commonly known superhard material is heterodiamond (c-BC_2N) which is more incompressible and harder than boron nitride [3]. The aforementioned compounds are strong covalent compounds formed out of light elements like boron, carbon and nitrogen. They are metastable and are synthesized with simultaneous application of high pressure and high temperature.

With the rapid advance in technology, there is an increased demand for materials which can be used for machining (shaping, cutting, grinding) and can withstand harsh conditions of pressure, temperature, chemicals and radiation. The hard refractory materials have met these expectations to a good extent. For example, silicon carbide and alumina are used in high-temperature furnaces. In nuclear reactors, the neutron shields are comprised of steel and B_4C. Tungsten carbide, steel, agate are widely used for crushing, milling and not surprisingly there is a thrust area of research for the improvement of mechanical properties of such materials. This has led to pursuit for new superhard materials. A

proposed way of designing superhard material is incorporation of light elements to a transition metal (TM) lattice to obtain transition metal borides (TMB), transition metal carbides (TMC) and transition metal nitrides (TMN). In this approach, the high valency of TM and high covalency offered by the light elements play the key roles. The high valency resists compression and the high covalency resists elastic and plastic deformation so that high hardness can be achieved [2, 4]. With this background, this thesis presents detailed studies on some of the TMBs and TMCs. In the following sections, TMBs and TMCs are discussed independently.

1.2. Transition metal borides

Due to electron deficiency boron readily combines with transition metals (TM) to form transition metal borides of various stoichiometries like TM_3B, TM_2B, TM_3B_2, TM_3B_4, TM_2B_3, TMB, TMB_2, TMB_3, TMB_4, TMB_6 and TMB_{12} [5]. A wide range of studies have been carried out on TMBs and many interesting results have been reported [6-10]. Moreover, the extensive range of stoichiometries of TMBs present a fertile ground for exploration of their structural stability with pressure. In the following subsections, structure and properties of TMBs have been described in detail.

1.2.1. Structure of transition metal borides

Depending on the stoichiometry, transition metal borides adopt different structures. TM_3B type boride adopts cementite structure (orthorhombic, spacegroup Pnma). TM_2B type borides have been observed to adopt three prototypes $viz.$ Mg_2Cu, Al_2Cu and Cl_2Ca. However, for Pt_2B a new monoclinic structure has been observed [11]. Not many TM_2B_3 are reported to be synthesized. However, Cr_2B_3 crystallizes in V_2B_3 structure [12]. The monoborides are orthorhombic (FeB or TlI type) or tetragonal MoB type in structures. The $4d$ and $5d$ monoborides have been studied with first-principle calculations in B1 (NaCl) type, WC-type and NiAs type structures [13]. For diborides, the structure which broadly

occurs is AlB_2 type. Few such examples are TiB_2, VB_2, ZrB_2, TaB_2, NbB_2, MoB_2 etc. ReB_2 has a different structure type. Both AlB_2 and ReB_2 are hexagonal with space group P6/mmm (191) and $P6_3$/mmc (194), respectively. These structures are comprised of metal layers with intercalated boron layers. But, in AlB_2 type structure the planar metal layer (A) and the planar boron layer (H) are stacked in the sequence AHAH------. In the case of ReB_2 structure type, there are two types of planar metal layers (A and B) and the boron layers (H) are puckered. The stacking sequence is AHBHAHBH-----[5]. Studies using density functional theory on some of the diborides have shown that ReB_2 type structure shows better hardness as compared to AlB_2 type structure. ReB_2 type MnB_2 is predicted to be superhard [14, 15]. RuB_2 is another prototype for diboride and OsB_2 is seen to adopt RuB_2 type structure [16]. Not many tetraborides have been studied experimentally but have been explored mainly by first-principle calculations. Synthesis of MnB_4, CrB_4, FeB_4 and WB_4 have been reported in literature [17-20]. Hexaborides and dodecaborides crystallize in cubic structure. For a quick look, this discussion is summarized in table 1.1 [21].

1.2.2. Properties and Applications

With good durability, oxidation resistance, corrosion resistance and impressive thermal shock resistance, transition metal borides are used as surface protection coating and they find application in aviation, abrasive and combustion chambers [5, 22]. Boride coatings can be obtained by the methods of boriding or boronizing (diffusion of boron atoms into metal surface to form metal borides), powder immersion reaction assisted coating (PIRAC), vapour deposition, electrodeposition, air plasma spray or high-velocity oxy-fuel (HVOF) spray [5, 23, 24]. Some of the boriding methods have been patented [25, 26]. In recent years, studies on iron boride coating on cast iron, tungsten boride coating on AISI D2 steel and iron borides on AISI M2 steel have been reported [27-29]. Boriding of pure titanium has been seen to enhance the surface properties and has bioimplant application [30].

In the case of boriding of cemented tungsten carbide, boride surface layers are formed and they act as a diffusion barrier against cobalt as well as strengthen the material by improving hardness and elastic modulus [31].

Table 1.1:   Structure of selected stoichiometries of transition metal borides

Compound type	Prototype	Structure		Examples
		Crystal System	Space Group	
TM_3B	Fe_3C	Orthorhombic	Pnma (62)	Fe_3B, Co_3B, Ni_3B
TM_2B	Mg_2Cu	Orthorhombic	Fddd (70)	Cr_2B, Mn_2B
	Al_2Cu	Tetragonal	I4/mcm (140)	Fe_2B, Co_2B, Ni_2B, Mo_2B, Ta_2B, W_2B
	--	Monoclinic	C2/m (12)	Pt_2B
	Cl_2Ca	Orthorhombic	Pnnm (58)	Pd_2B
TM_2B_3	V_2B_3	Orthorhombic	Cmcm (63)	Cr_2B_3
TMB	FeB	Orthorhombic	Pnma (62)	TiB, MnB, CoB, HfB
	TlI	Orthorhombic	Cmcm (63)	VB, TaB, CrB, NiB, NbB,
	MoB	Tetragonal	I4$_1$/amd (141)	WB
TM_3B_4	Ta_3B_4	Orthorhombic	Immm (71)	Mn_3B_4, Cr_3B_4, V_3B_4, Nb_3B_4
TMB_2	AlB_2	Hexagonal	P6/mmm (191)	VB_2, TaB_2, CrB_2, MnB_2, NbB_2, WB_2
	ReB_2	Hexagonal	P6$_3$/mmc (194)	High temperature– WB_2
	RuB_2	Orthorhombic	Pmmn (59)	OsB_2
TMB_4	CrB_4	Orthorhombic	Pnnm (58)	FeB_4
	MnB_4	Monoclinic	P2$_1$/c (14)	--
	WB_4	Hexagonal	P6$_3$/mmc (194)	--

Due to the high melting point and good thermal stability, TMBs act as a diffusion barrier. With good adhesion to silicon and as a diffusion barrier, titanium boride, zirconium boride and hafnium boride find application in making of semiconductor devices [32]. Evolutionary algorithm with first-principle calculations has predicted that multilayer 2D iron borides FeB_x with x = 4, 6, 8 and 10 are wide-bandgap semiconductors and can have application in ultraviolet/ blue optoelectronic devices [33]. With high neutron capture cross-section boron compounds like TiB_2 and ZrB_2 act as control rods in nuclear reactors and also as thermocouple protection tube [5, 34, 35].

With high density, low weight to strength ratio and good electrical conductivity, TMBs have gained huge attention as energy storage material. A patent dating back to 1999 was made with the title "high energy density boride batteries". In the patent, it is discussed that titanium and vanadium diborides are preferred as anodic elements; and the cathodes can comprise of FeB and NiB_2 [36]. Some of the studies in recent years have reported that TaB, TaB_2 and TiB_2 as anode materials of batteries and iron borides as the cathode material, show high capacity [37]. VB_2 based electrochemical energy storage supersedes the capacity of lithium-ion battery [38, 39]. It is even seen that insertion of boron into V by high energy ball milling enhances the anodic activity of V impressively and improves the discharge capability [40].

Among binary TMBs, semiborides like Mo_2B, Re_2B and W_2B are observed to be superconductors [21]. Monoborides like ZrB, HfB, NbB, TaB and diborides like MoB_2, NbB_2 also show superconductivity. However, MoB_2 and NbB_2 with exact stoichiometry do not show superconductivity [21]. FeB_4 (orthorhombic, Pnnm) was first predicted to be a phonon mediated superconductor and later on it was synthesized using high pressure (8 GPa) and high temperature [19, 41]. FeB_4 becomes a superconductor below 2.9 K and has a nano-

indentation hardness of 62(5) GPa [19]. Among hexaborides and dodecaborides, YB_6, ScB_{12}, YB_{12} and ZrB_{12} show superconductivity [21].

Considering the huge application and tremendous possibilities TMBs offer, it is of interest to synthesize and study their various properties. In the present thesis, the study of compressibility behaviour of TMBs is on focus. Hence, a survey on hardness, phase stability and high pressure behaviour of TMBs as well as various synthesis methods is apt here.

1.2.3. Hardness, phase stability and high pressure behaviour of TMBs

The present literature concerning studies of TMBs under high pressure is scattered and there is scope for systematic studies. Among the TMBs, borides of *5d* TMs *viz.* ReB_2, OsB_2 and IrB_2 are found to show superior mechanical properties [17, 18, 42-47]. With not much thought, this can be connected to the higher valence densities *5d* transition metals offer. However, there are claims and conflict that the *3d* TMB i.e. CrB_4 is also superhard [18, 48, 49]. This makes the study of *3d* TMBs important and interesting.

Some of the transition metal borides like TiB_2, ZrB_2, HfB_2, TaB_2, MoB_2, Ni_2B, Mo_2B, Fe_2B, FeB, CrB, CrB_2, MnB_4, CrB_4, OsB, WB, WB_2, WB_4, ReB_2 and OsB_2 have been studied experimentally under high pressure [6, 7, 10, 43, 44, 50-57]. The mentioned borides were found to be structurally stable in the pressure range studied and a bulk modulus range of 170 GPa (for MnB_2) to 453 GPa (for OsB) was observed for them. It is noteworthy that the bulk modulus of OsB and WB are comparable to that of diamond. Certain *ab initio* calculations have predicted structural transitions of TMBs under high pressure. For example in the case of VB_4, the *Cmcm* structure may undergo a transition to *Amm2* structure type at 12 GPa [58]. A structural transition of rhombohedral to tetragonal $ThSi_2$ structure has been predicted at 68 GPa for MoB_2. In this case, the high pressure phase is quenchable to

ambient condition [59]. Also, in the case of ScB_2, YB_2 and TiB_2, structural transitions are predicted at 208, 163 and 215 GPa, respectively [60]. First principle based electronic structure calculation of FeB_4 has shown that metallic FeB_4 undergoes a transition to semiconducting phase at 53.7 GPa [61].

For the present work, the cohesive energy of TMB, which reflects the stability of a phase was considered as a parameter for study under high pressure. Not many systematic studies on compressibility or mechanical properties have been reported. However, both in the case of TMB_2 and TM_3B_4, studies based on density functional theory have shown that stability is the highest for group 4B transition metals (Ti, Zr and Hf), second highest for 5B elements (V, Nb, Ta) and it keeps on decreasing along the period [62, 63]. Hence, some of the borides of these elements *viz.* VB, TaB and TiB_2 were studied under high pressure which may show better incompressibility behaviour. These studies will be discussed in chapter 3. Now, the various methods which can be adopted for the synthesis of TMBs, and the challenges therein are discussed in the following subsections.

1.2.3.1. Synthesis Methods

Transition metal borides are generally synthesized either from a direct reaction between elements or by use of precursors. The methods with the help of examples are discussed below.

From Elements:

Some of the methods which are used to synthesize TMBs from elements are described below.

i. Solid state reaction method:

In solid state reaction method, crystalline samples can be synthesized starting from solid reactants at high temperature (below the melting point of the starting elements). The

elements diffuse into each other to form compounds. Synthesis of single crystal of Cr_2B is described in reference 64. For the synthesis, first of all, Cr in weight percent of 86.5 % and B were mixed in a B_4C mortar and then the mixture was pelletized. The pellet was placed in an alumina crucible in argon environment and heated up to 1923 K at a rate of 100K/hr, held for 5 hr at that temperature and then cooled to 1273 K at a rate of 10K/hr. Then, the furnace was turned off to obtain the product [64].

ii.   Combustion Synthesis:

Combustion synthesis relies on exothermic reactions and can be illustrated with the synthesis of various niobium borides and vanadium borides. In the case of synthesis of NbB starting from Nb and B, a single phase of NbB formed along with unreacted Nb [65]. For the synthesis of vanadium boride, elemental vanadium and amorphous boron were taken in the ratio 1:1, 5:6, 3:4, 2:3 and 1:2. The mixtures were ball milled for 10 hr at 120 rpm. Then self-propagating high-temperature synthesis (SHS) was carried out in a combustion chamber in an argon atmosphere. In the attempts to synthesize, VB, V_5B_6 and V_3B_4, only VB phase formed. With the starting ratio of V:B = 2:3, the final product contained only VB and V_3B_4 and, in the attempt to synthesize VB_2, the product had VB and V_3B_4 along with VB_2 [66].

iii.   Mechanochemical synthesis:

Some borides are synthesized by mechanical alloying using the ball mill method. With the use of planetary ball mill, NbB and NbB_2 were synthesized by milling Nb and B for 60 hours. However, with the planetary ball mill, chromium boride did not form even after 60 hour milling and, only amorphization of chromium was observed [67]. However, CrB and CrB_2 were synthesized by ball milling for 40 hr followed by annealing at 1000 °C and with milling time of 30 hr followed by annealing at 900°C, respectively [68].

iv.   **Arc Melting:**

Arc melting method is generally adopted for the synthesis of TMBs as they require very high temperature. Cr_2B and Mn_2B were synthesized with Arc melting method followed by heat treatment of the melted ingot. For the synthesis of TiB also, arc melted method was adopted. Wherein excess metal was used and TiB formed as needles embedded in excess titanium. The excess titanium was melted in hot sulphuric acid to recover single crystals of TiB [69].

From precursor:

TMBs are also synthesized from precursors and in general, they have comparatively lower reaction temperature than that in the case of synthesis from elements.

i.   **Metal flux method:**

The common precursors are metal oxide or metal chloride. They can form transition metal borides by reaction with boron. Nanorods of FeB and OsB_2 crystals were synthesized starting from the Fe_2O_3, and $OsCl_3$ and, a mixed phase of RuB_2 and Ru_2B_3 was obtained from $RuCl_3$ [70]. Nano-sized single phase TMBs could be synthesized by heating the pellet of the mixture of metal chloride and elemental Sn. In this case, Sn acts to reduce the reaction temperature [71].

ii.   **Mechanochemical combustion method:**

TMB can also be synthesized by mechanochemical combustion method. Vanadium monoboride was synthesized by taking a mixture of Mg, V_2O_5, B_2O_3 in the ratio 1:1:8 and the mixture was ball milled for 100 minutes. Then, the by-product i.e MgO was removed by leaching [72]. NbB was also synthesized by the similar method with Mg, Nb_2O_5 and Mg

as the starting materials [73]. Some of the other methods for synthesizing TMB starting with precursors are discussed below.

iii.   Hydrothermal Synthesis:

Typical example of the synthesis of boride using this method is discussed as follows. For the synthesis of TiB_2, ZrB_2 and NbB_2, respective metal oxides such as TiO_2, ZrO_2 and Nb_2O_5 along with amorphous boron, metallic sodium and sulfur were mixed in pre-decided stoichiometry and placed in an autoclave and heated. Then after cooling, the raw product was washed with absolute ethanol, distilled water, hydrochloric acid and then again with distilled water. The product was then dried in vacuum to obtain boride [74].

1.2.3.2.   Challenges in the synthesis of TMBs

Due to favourable formation energy and high stability, TMBs form easily at high temperature. However, due to degeneracy in the energy of formation, synthesizing single phase is a difficult task. Also, due to a high difference in atomic weight between TM and B, getting exact stoichiometry is difficult. As it could be seen in the case of synthesis of vanadium borides by combustion methods, with different starting stoichiometries, only VB was formed and with starting stoichiometry of V:B = 2:3, only V_3B_4 and VB formed [66]. In the attempt to synthesize cobalt boride using radiofrequency thermal plasma, with starting ratio of Co:B = 1:2 and 1:3, multi-phases of Co_2B and CoB formed [75]. These problems were also faced in the attempts to synthesize chromium borides (not included in the thesis) and vanadium borides by ball milling, solid-state method and arc melting during the course of the present thesis work.

1.3. Transition metal carbide

Like TMBs, transition metal carbides have immense application as hard refractory materials. Accordingly, their synthesis and studies are also a thrust area of research in the field of material science. For the synthesis of TMCs, solid-state reaction method, mechanochemical synthesis or their combination are adopted generally [75-78]. In addition, chemical vapour deposition and ion implantation methods are also adopted for synthesis of certain TMCs [79, 80].

1.3.1. Importance of carbon rich TMCs and challenges in synthesis

There is a common proposition that when more boron or carbon is inserted into a TM lattice, due to increased covalency, the mechanical properties improve. In the case of TMBs, it was seen that boron rich phases are formable due to favourable formation energy and they can be synthesized using high-temperature methods. But, that is not the case with TMCs. A survey on the phases adopted by various transition metals was carried out and they are listed in table 1.2. The elements which are coloured green in the table do not form any carbide phase and the compounds which are coloured blue are synthesized by high-temperature methods. It can be noted here that, among these reported compounds, there are hardly any carbon-rich phases, i.e, TM_xC_y where $y > x$.

The instability of carbon-rich carbide phases can be understood in terms of how TMCs form. Generally, the carbon atoms are considered as interstitials in the TM lattice. When C atoms are put into the TM lattice, TM-TM bond weakens and TM-C bonds start forming. The stability of a particular phase is dependent on the balance between the strength of TM-TM and TM-C bonds [81]. Formation and strength of TM-C bonds can be understood in terms of overlapping of the electronic states of the respective atoms. There are two phenomena involved in the overlapping process. One is Pauli repulsion which costs energy,

and another is hybridization forming bonding and anti-bonding states. For bonding states, as the hybridization effect is attractive, it compensates for the energy cost of Pauli repulsion. For the anti-bonding states, the opposite effect is seen. So, the TM-C bonds with only the bonding states filled, are the strongest [82]. In the case of transition metal carbides, the filling of anti-bonding states increases towards the latter part of a TM series making the respective TM-C bonds weaker. This hinders inclusion of more carbon and is the cause of the absence of carbon-rich carbide phases for the TM present in the latter part of a series. Nonetheless, high-pressure synthesis has been found to mitigate such issues and many exotic compounds have been reported to be synthesized under high pressure, which are not formable otherwise. Those compounds are briefly reviewed below.

Table 1.2:   Compounds formed by transition metals with carbon. The compounds which are synthesizable using high temperature methods are coloured blue. The compounds which are coloured red have been reported to be synthesized by high pressure high temperature method. The green colour elements do not form any carbide.

$Sc_{23}C_6$ ScC_2 Sc_2C_3	TiC	V_2C VC	$Cr_{23}C_6$ Cr_7C_3 Cr_3C_2	$Mn_{23}C_6$ Mn_3C Mn_5C_2 Mn_7C_3	Fe_3C	Co_3C	Ni_3C	Cu	Zn
Y_2C Y_2C_3 YC_2	ZrC	Nb_2C NbC	Mo_2C Mo_3C_2	Tc	Ru_2C	Rh	Pd	Ag	Cd
	HfC	Ta_2C TaC	W_2C W_3C_2 WC	Re_2C	Os_2C	Ir	PtC	Au	Hg

1.3.2. Synthesis of novel materials using high pressure technique

The most well-known examples of synthesis of materials using high pressure and high-temperature technique are the synthesis of metastable phases like diamond, boron nitride, and stishovite [83]. Synthesis of new functional materials like multiferroics and

materials for thermoelectric applications have been possible under high-pressure [84-87]. Recently, compound formation by noble helium, argon and xenon under high pressure has been reported [88-90]. Counterintuitive phases like Na_3Cl, $NaCl_3$ and KCl_3 have also been synthesized [61, 91]. In the search for high energy density materials, nitrogen-rich compounds are promising candidates. However, like carbon-rich TMCs, the synthesis is challenging. But, recently, polynitrogen iron compounds have been synthesized using laser-heated diamond anvil cell [92].

The breakthrough discovery of extraordinarily high-temperature superconductivity in sulfur hydride system has given great boost to the exploration for newer materials. Computational studies have predicted superconductivity in the family of pnictogen hydride [93, 94]. In the journey towards room temperature superconductivity lanthanum superhydride which was synthesized at 170 GPa and 1000 K is observed to be superconductor at 260 K and 200 GPa [95, 96]. In the case of TMC in particular, high pressure synthesis of Ru_2C, Os_2C, Re_2C and PtC have been reported. These compounds are also included in table 1.2 and are marked in red [97-100].

As discussed before, the design of superhard TMCs, requires combination of a transition metal with high valency and incorporation of more carbon. Among the *3d* transition metals, Mn can have highest valence state and chromium can have the second highest valence state. Hence, for the present thesis, the objective was to synthesize carbon rich novel phases of manganese carbide and chromium carbide. These studies will be discussed in chapter 4 and chapter 5, respectively.

1.4. Objective of the thesis

In the light of the above discussion the objective of the thesis is outlined as follows.

1. Experimental and computational study of group 4B and 5B transition metal borides *viz.* VB, TaB and TiB$_2$ under high pressure to understand their compressibility behaviour. These studies will be discussed in chapter 3

2. HPHT synthesis of novel TMCs *viz.* manganese and chromium carbide using laser heated diamond anvil cell. The syntheses and further studies will be discussed in chapter 4 and 5, respectively.

Chapter 2

Experimental and computational techniques

2.1. Introduction

This chapter briefly describes the methodologies adopted for carrying out the work presented in the thesis. This involves synthesis of transition metal borides and novel transition metal carbides using high temperature and high pressure-high temperature (HPHT) method, respectively. For synthesis of vanadium monoboride, arc melting method was adopted. Diamond anvil cell (DAC) was used for generation of high pressure. HPHT syntheses were carried out using laser heated diamond anvil cell (LHDAC). The TMBs and TMCs were studied under high pressure using high pressure X-ray diffraction (HPXRD) technique as well as *ab initio* density functional theory. HPXRD experiments were performed using both lab sources and synchrotron source in combination with DAC. For characterization of LHDAC synthesized sample, along with XRD, micro-Raman spectroscopy and selected area electron diffraction were used. The above mentioned methods are discussed in the following sections.

2.2. Synthesis methods

2.2.1. Arc melting with tri-arc furnace

Arc melting method is a very useful tool with which temperature as high as 3000°C can be achieved. With the ease of operation and the inert environment it provides, the method is utilized to synthesize compounds and alloys from pure elements. The picture of the tri-arc electric furnace in our lab is shown in figure 2.1(a). The melting chamber is made up of pyrex glass which is connected to two brass bases at the top and the bottom. Three copper stingers with three tungsten electrodes (cathodes) are held by the top base and, the bottom

base holds the copper hearth (anode). In figure 2.1 (b), the titanium getter and the starting elements placed in the copper hearth are shown and in 2.1(c), the picture of the arc is presented.
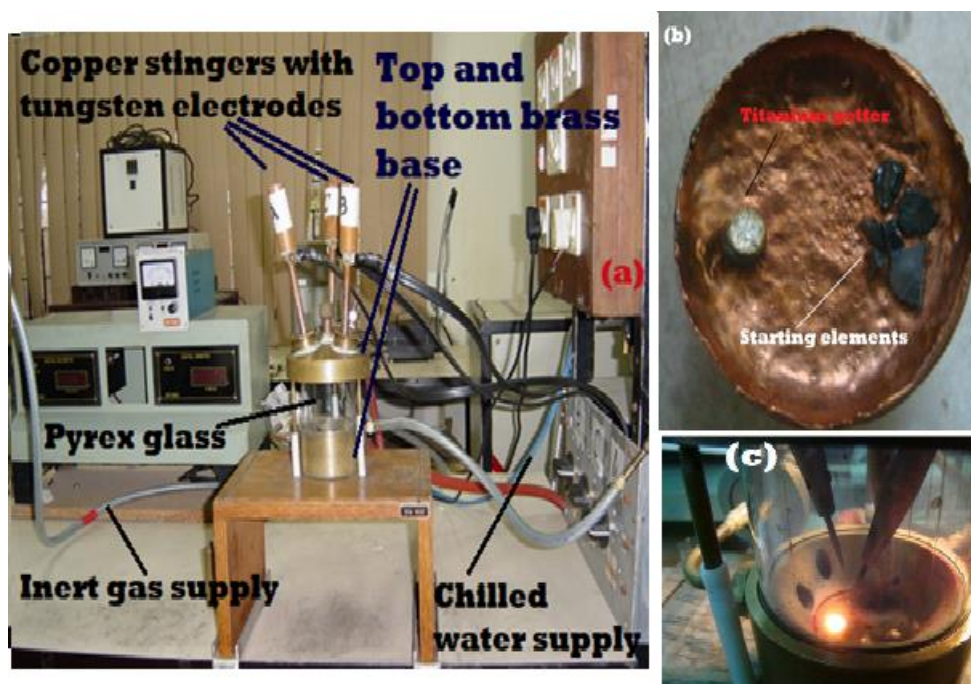
Figure 2.1:   (a) Photograph of the tri-arc furnace in our lab in which different parts of the furnace have been labelled, (b) the titanium getter and the starting elements, (c) the struck arc.

The melting chamber is sealed with o-rings and valves. A DC power supply to the electrodes provides the necessary power to strike the arc. The heating is done by striking electric arc between the tungsten electrode and the metal to be melted placed on the copper hearth. There is provision for chilled water circulation to prevent overheating and destruction of the electrodes. Prior to melting, the furnace is evacuated to a pressure of 10^{-2} torr and then purging is carried out by flowing inert gases like helium or argon. This action is performed repeatedly and before the melting of the desired sample, a titanium getter is melted to remove any possible oxygen left in the chamber. The melting is

performed in inert gas environment. The sample is melted and the obtained ingot is flipped and melted repeatedly (3 to 4 times) to improve the homogeneity of the sample.

2.2.2. High pressure-high temperature (HPHT) methods

Historically, the first high P, T experiments were carried out during the quest to achieve laboratory synthesis of diamond [101, 102]. There are several methods for high pressure generation and they will be briefly discussed here followed by the techniques to couple high temperature for HPHT synthesis.

2.2.2.1. High pressure Devices

The high pressure devices can be broadly classified into 1: piston-cylinder type, 2: opposed anvil apparatus and 3: multi-anvil apparatus. In a piston-cylinder type device, the pressure vessel is a cylinder that is closed at one end by a rigid plate. Piston, generally constructed of cemented tungsten carbide is advanced into the cylinder at the other end. The pressure achievable with this is ~ 3 GPa. Simultaneously temperature can be achieved with this device by including a resistance furnace to the sample assembly. Controlled high temperature (~1700°C) can be generated by applying a regulated voltage to the sample. Temperature is monitored using a thermocouple which is inserted through a small hole in the rigid plate [103].

Bridgman introduced an high pressure apparatus which is based on two opposed anvils [104, 105]. The sample is compressed between the flat tips of the anvils which are made from hard materials like tungsten carbide or sintered diamond, supported with a steel binding ring. The gasket can be pyrophyllite, catlinite or a metal, depending on the type of measurements. This kind of anvil assembly exploits the method of massive support provided by the anvil materials around the sample chamber [106]. Pressure up to 25 GPa can

be achieved using Bridgman cell. Drickamer anvils, profiled anvils (toroidal cell and cupped cell) and diamond anvil cell are the other variants of opposed anvil cell.

Diamond anvil cell is the workhorse for the high pressure experiments presented in this thesis and the details of this cell would be presented in the later part of this section. Drickamer cell was invented by Forsgren and Drickamer in 1965 [103, 107, 108]. This consists of a pair of opposed anvils and containment ring. It is a large volume cell which provides optical access and might still be useful for certain applications which rely on large sample volumes. Generally used anvils are tungsten carbide, but good sintered diamond can be used to achieve pressure up to ~40 GPa. Sintered anvils made from c-BN (transparent for X-ray) can also be used. Profiled cells give room for more sample volume (about 100 cm^3) at the cost of maximum pressure achievable. The belt apparatus, invented in 1954 by the scientist Tracy Hall of the General Electric Company for use in the company's diamond-making program, incorporates features of both opposed-anvil and piston-cylinder designs [109]. The equipment makes use of conical Carboloy pistons that push into each end of a specially shaped Carboloy chamber. Both chamber and pistons receive lateral support from binding rings. The chamber and binding rings form a toroidal "belt" around the sample, hence the name of this apparatus. Axial motion of the conical pistons in and out of the chamber is accomplished (while still maintaining a pressure seal) by the use of a specially shaped sandwich gasket made up of naturally occurring pyrophyllite and a steel cone. The arrangement gives a multistaging effect in a single stage. Pyrophyllite in addition to its use in the gasket, is also used as pressure transmitting medium, thermal insulation, and electrical insulation [109]. The pressure attainability of this apparatus is in the 5-10 GPa range, but Bundy reported measurements up to 20 GPa [110].

Multi anvil apparatuses are devices consisting of more than two anvils and in almost all cases, these apparatuses allow to probe "large volume" of samples (~ 1 mm^3 or more). These cells require considerable forces typically ~500-2000 ton of load. Multi anvil cells can be classified according to the geometry of pressure chamber. The different types are tetrahedral, cubic or octahedral anvil cells. The force is usually applied by hydraulic press [103].

In a diamond anvil cell (DAC), high pressure is created by trapping the sample between the culets (flat) of two diamonds. The force applied across the table of the diamond generates tremendous pressure on the culet, which is smaller in area. As diamond is the hardest material and is transparent to electromagnetic radiations, highest pressures of the order of 100 GPa can be achieved as well as in-situ high pressure measurements can be performed on the sample. Different types of DACs have been constructed depending on the probe to be used for characterization or investigation. Broadly, there are five types of DACs. They are Bassett cell, Mao-Bell cell, NBS cell, Syassen-Holzapfel cell and Merrill-Bassett cell [111]. Other recent types are the toroidal-DAC and membrane cell DAC. In toroidal-DAC, the diamond anvil tips are of toroid shape and with that static pressure of the order of teraPascal can be achieved [112]. In membrane cell DAC, pressurized helium is used to generate the force on the piston and the piston pushes an annular membrane [113]. Also For the present thesis work, a Mao-Bell type DAC fabricated in-house, has been used for the high pressure and high temperature experiments [114, 115]

Mao-Bell type DAC:

Mao-Bell type DAC is a combination of opposed anvil and piston cylinder mechanism. It uses a lever arm mechanism to generate force. In figure 2.2 (a) and (b), the schematic and the picture of the DAC in our lab are shown. The diamond anvils used have

a culet size of about 500 micron and the tables have diameter of about 2 mm. Identical diamonds of almost equal dimension are mounted on the hemispherical tungsten carbide (WC) rocker and cylindrical tungsten carbide seat. They are fixed to the cylinder (1) and piston (2), respectively with the screws provided. In figure 2.2 (c) and (d), the diamonds mounted on the tungsten carbide rocker and seat are presented. The photographs of the piston and cylinder are shown in figure 2.2 (e). The sample is placed in a hole drilled in the gasket and the gasket stays confined between the culets of the two diamonds. The piston cylinder assembly is held by a pressure cell holder (6) and is in contact with the thrust block (3) of the lever arm (5). The lever-arm (5) loaded with Belleville springs (8), exerts force on the cylinder-piston assembly by the mechanical driving of the screws (7). A pressure of 100 GPa can be achieved with the in-house DAC.

Alignment of DAC:

The alignment of DAC is crucial for the stability of DAC as well as for carrying out the diffraction experiment. The alignment methods are described below.

Lateral alignment: The culets of the two diamonds mounted on the piston and cylinder should be laterally matched. Lateral alignment is essential to achieve high pressure. In figure 2.3 (a), laterally misaligned diamonds are shown. The diamonds are aligned using the screws that hold the tungsten carbide seat and rockers placed in the piston and cylinder respectively.
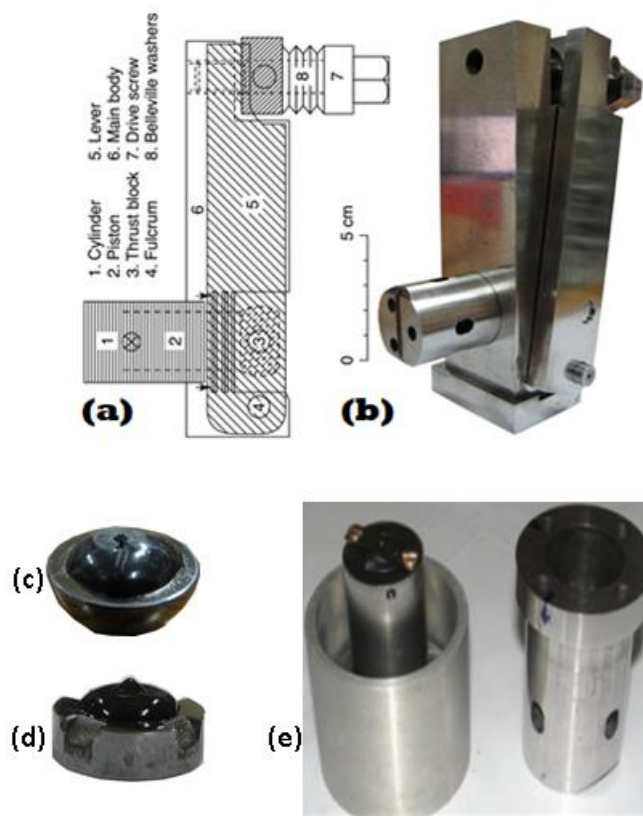
Figure 2.2: (a) Schematic of the in-house Mao-Bell type DAC, (b) photograph of the DAC in our laboratory, (c) the diamond mounted on the WC rocker, (d) the diamond mounted on the WC seat, (e) photograph of the piston and cylinder with the anvils installed.

Tilt alignment: The culets should be absolutely parallel to each other and any wedge between them leads to breakage of diamond at high pressure. The misalignment, if any, is removed as follows. The diamonds are kept face to face and a source of white light is passed through the bottom of the cylinder. The culet face is observed under microscope through the piston. In case of misalignment, interference fringes (Newton's rings) are seen.
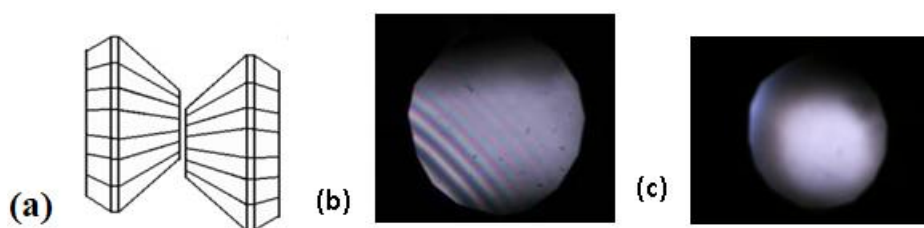
Figure 2.3: (a) Laterally misaligned diamonds, (b) presence of fringes due to wedge between diamond culets and (c) tilt aligned diamonds

This fringe is eliminated by tilt adjustments of the cylinder rocker. In figure 2.3 (b), the presence of fringes due to misalignment is shown and the photograph with fringes removed by proper alignment is presented in 2.3(c).

2.2.2.2.   Coupling of high temperature

Sample between the anvils can be heated either by internal or external method. In internal method, current is passed through the sample by a wire made up of the same sample. The phase diagram of iron was studied up to a pressure of 43 GPa by Boehler *et al*.(1986) and up to 36 GPa by Mao et al (1987) at temperature up to 1400°C [116]. But this method demands the sample to be electrically conducting and hence imposes a limitation. In external heating, either the device (in case of DAC) as a whole is heated by placing it in a furnace, or the cavity just around anvils is heated with a heater coil [103]. Another non-contact method of heating the squeezed sample in DAC is laser heating.

Laser Heated Diamond Anvil Cell:

LHDAC is a unique tool to simulate high pressure and high temperature conditions simultaneously. At high pressure the electronic structure changes and this is generally expected to enhance chemical reactivity leading to novel reaction pathways [83, 117, 118]. Hence many novel and exotic phases which are not synthesizable in ambient pressure condition can be synthesized and characterized. Application of LHDAC also include investigation of melting phenomena and structural transitions of variety of materials, investigation of P-T behavior of geophysically important minerals like silicate, sulphates, oxides etc [118]. LHDAC technique was first attempted successfully by Basset and Ming in early 1970s [119, 120]. The advantages of this technique are; (a) extremely localized direct heating of sample, (b) contamination free sample chamber while using inert gas as pressure medium, (c) large range of pressure and temperature. The challenges in setting up this

facility is focusing the invisible infrared laser beam into the ultra-tiny sample (~100 μm) sandwiched between the anvils by a careful optical arrangement without causing any damage to diamonds and other supporting materials. The important tasks are to enable simultaneous viewing of the sample being heated and estimation of temperature and pressure.

Description of the LHDAC facility:

A brief description of the LHDAC facility in our laboratory is given below. Pressure ~100 GPa and T ~5000 K can be achieved simultaneously using this LHDAC. The facility consists of (a) Mao-Bell type diamond anvil cell, (b) 120 W CO_2 laser(λ=10.6 μm ; TEM_{00} mode), (c) A CCD based spectrometer, (d) X-Y-Z nanomotion system, (d) CCD based imaging system. The schematic diagram and the photograph of the in-house developed LHDAC are shown in figure 2.4 and 2.5, respectively.
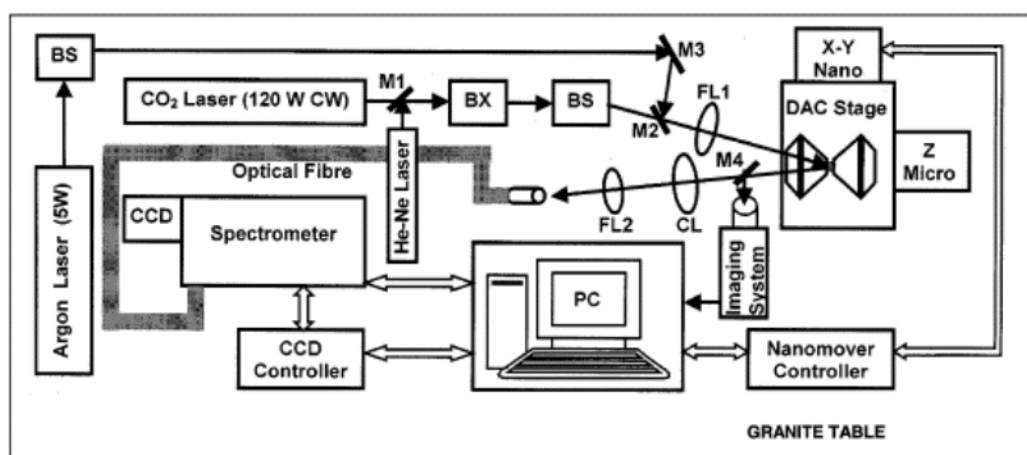
Figure 2.4:   Schematic of the LHDAC facility at IGCAR

CO_2 laser is invisible, so the preliminary alignment is carried out with visible He-Ne laser. Towards the He-Ne laser, M1 is kept (a silicon mirror) such that He-Ne laser traverses the same path as the CO_2 laser. BX (beam expander), BS-Beam Steerer, mirror M2 and FL1 (ZnSe coated focusing lens) are used to obtain a fine focused spot on the

sample. The spot size is related to the focal length (f) of FL1 and beam diameter D of the IR laser by the relation $4\lambda f/D$ for TEM_{00} mode. The spot size obtained on the sample is of the order of 40 μm. The sample is heated uniformly in rastering manner by moving the XYZ stage on which DAC is mounted.
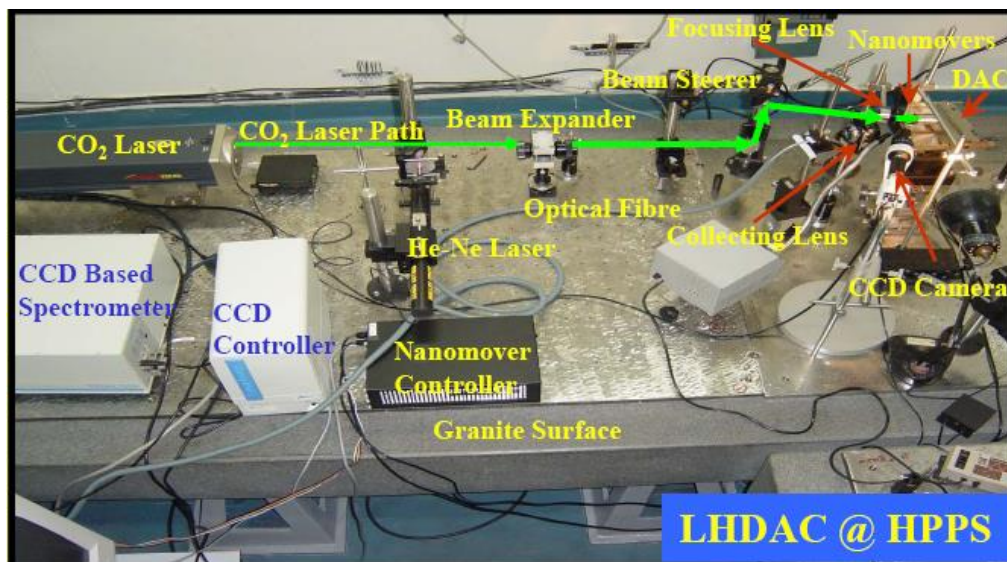
Figure 2.5:   Photograph of the LHDAC facility at IGCAR. The parts of the setup has been marked in the picture.

Sample assembly for LHDAC experiment

A schematic diagram of the sample assembly for laser heating is shown in figure 2.6. First of all, a gasket is chosen. Different kinds of gasket materials are used *viz.* rhenium, tungsten carbide, stainless steel, pyrophilite etc depending upon the experiment to be performed and the highest pressure to be achieved. The gasket is pre-indented by squeezing it between the aligned diamonds. Then, a hole is drilled using drill bits or by electro discharge machining (EDM), which functions as the sample chamber. The sample is loaded along with pressure transmitting medium (PTM) and pressure calibrant. Different kinds of PTMs like silicone oil, methanol-ethanol-water (MEW), inert gases like neon and argon or solids like KBr and NaCl can be used in high pressure experiments.
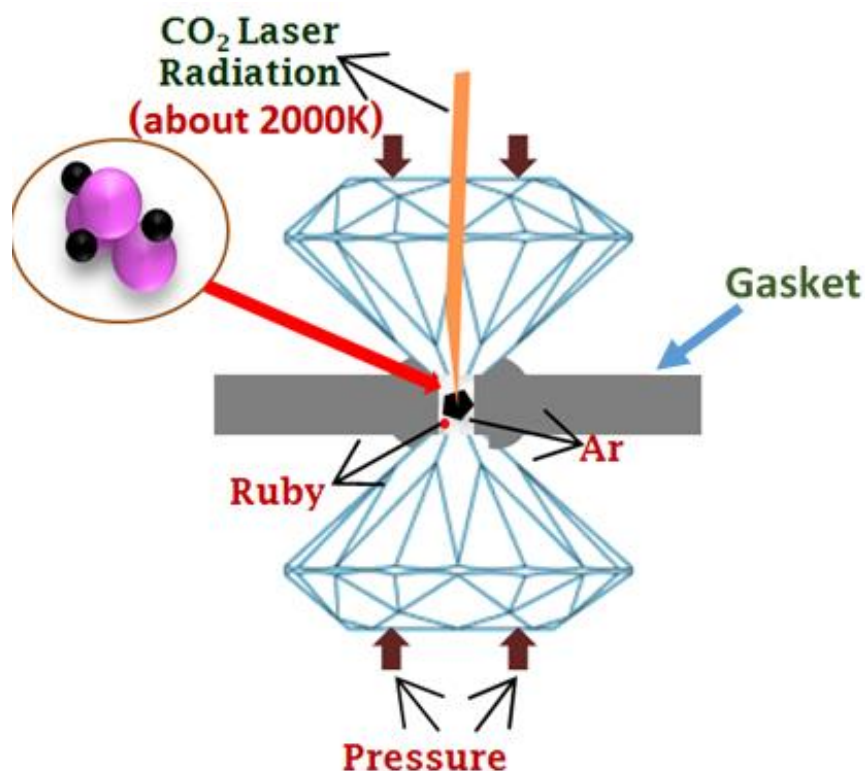
Figure 2.6:   Schematic of sample assembly for LHDAC synthesis

Various PTMs have various hydrostatic limits [121]. For pressure calibration, ruby fluorescence method or equation of states (EOS) of metal marker like silver, gold or platinum can be used. However, in the case of LHDAC experiments, the PTM must be inert to avoid reaction of PTM with sample at high temperature and should also be insulating to prevent graphitization of diamond. Hence, for the LHDAC synthesis presented in this thesis, liquefied argon was used as PTM and ruby as pressure calibrant.

2.3.   Characterization and investigation methods

2.3.1.   High Pressure X-ray Diffraction

2.3.1.1.   Sample assembly

The sample assembly method for HPXRD experiments is similar to that for LHDAC synthesis experiment which consists of drilled gasket, PTM and pressure calibrant. For the HPXRD presented in the thesis, MEW was used as PTM and ruby as well as platinum were used for pressure determination.

2.3.1.2. X-ray Sources

Both lab and synchrotron sources have been used for carrying out HPXRD experiments.

Synchrotron X-ray source:

With high flux, good resolution, broad spectrum and highly collimated beam, synchrotron radiation is ideal for XRD characterization. The HPXRD studies on VB and TaB have been carried out at beamline 11, Indus-2, RRCAT, Indore, India. Indus-2 synchrotron source is a booster cum storage ring with a nominal electron energy of 2.5 GeV and a critical wavelength of about 1.98 Å where electrons are injected at 550 MeV and accelerated to 2.5 GeV [122]. The facility has a beam current of 200 mA at which angle dispersive XRD experiments can be carried out. A Si(111) channel cut monochromator is used to tune the wavelength. In order to avoid diffraction peaks from the gasket material used for high pressure measurements, a Kirkpatrick-Baez (KB) mirror arrangement is used to focus the direct beam.

Laboratory X-ray source based diffraction:

For XRD experiments at the laboratory, a Rigaku ULTRAX18 (18 kW) rotating anode X-ray generator (RAXRG) was used. The X-ray generator with a graphite monochromator produces Mo Kα radiation of wavelength 0.7107Å. The photograph of the RAXRG is shown in figure 2.7.For HPXRD experiments using lab source, the X-ray beam of ~100 μm is collimated on to the pressurized sample. This is done to avoid gasket reflections in the diffractogram. The collimation method is described below.

Collimation of X-ray beam to the sample:

To ensure the passage of X-ray beam through the middle of the sample, an internal slit is used. To achieve this, the slit is installed in the piston. A photographic film is placed between the diamonds in a dark room. The piston cylinder assembly is made light-proof with insulation tape around the access ports. The culet impression is made on the film by applying slight pressure on it. This assembly is exposed to X-ray for 30 sec. The exposed film is then developed in the dark room and visualized under microscope. The control screws of the internal slit (figure 2.8 (a)) are adjusted and the whole procedure is repeated until the X-ray falls at the centre of the culet. Optical images of the film in which the collimator is misaligned and aligned are shown in the fig. 2.8 (b) and (c) respectively.

Figure 2.7: Rigaku ULTRAX18 (18 kW) rotating anode X-ray generator with Mao-Bell type DAC loaded.
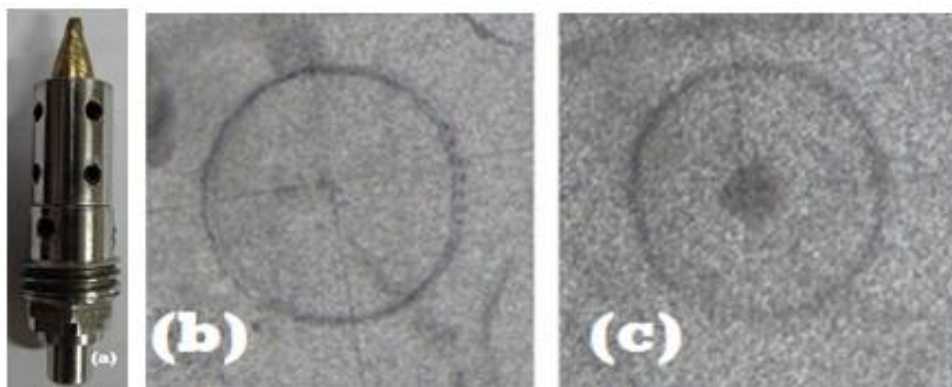
Figure 2.8: (a) Photograph of the internal slit, (b) optical image of the developed photographic film where the collimator is not aligned and the X-ray spot (dark spot) is outside the culet region. (c) X-ray spot at the centre of the culet showing an aligned collimator

Collection of diffraction pattern:

Both in the case of laboratory and synchrotron based X-ray sources, the X-ray diffraction patterns were collected on a 2D image plate. Mar345 dtb image plates were used for the HPXRD experiments.

2.3.2. Selected Area Electron Diffraction and TEM imaging

Both selected area electron diffraction (SAED) and TEM imaging are performed in a Transmission Electron Microscope (TEM). In a TEM, a sample of thickness ~100 nm is subjected to a high energy electron (order of hundred kilo electron volt) beam. The electron wave interacts with the sample and when it exits, there are both scattered and unscattered beam. The unscattered beam corresponds to the bright central spot on the diffraction pattern. In the imaging mode, objective aperture is inserted in the back focal plane of the objective lens. While using the objective aperture, if the central beam is selected and the rest of the signal is blocked, then a bright field image is obtained. If the signal from the diffracted beam is allowed and the direct beam is blocked, then the dark field image is obtained. The selected signal is magnified and projected on a screen or camera. In the

diffraction mode, a selected area aperture is used to determine the area of the specimen from which the signal will be displayed. By changing the strength of the intermediate lens, the diffraction pattern is obtained and displayed on a screen. Diffraction is a very useful tool for crystal structure determination.

To obtain information over a lager d-range, of the crystalline sample, SAED was carried out on the LHDAC synthesized sample, which is described in chapter 4. The conventional method of sample preparation for TEM cannot be followed because the quantity of sample retrieved in the case of LHDAC synthesis is of the order of a microgram. Hence, to get thin crystalline sample which would be electron transparent, the retrieved sample was sheared between the two diamond anvils. As the sample quantity is not enough to be dispersed in alcohol and subsequently to be transferred to the carbon coated copper grid, the sheared sample as such was transferred to the grid. Then the sample was examined by SAED and TEM imaging. For the experiments, a LIBRA 200FE (Carl Zeiss) high resolution transmission electron microscope (HRTEM) operated at 200 kV was used. The microscope has an information limit of 0.13 nm.

2.3.3. Micro-Raman spectroscopy

In micro-Raman spectroscopy, the probe laser is focused to a size of 1-2 micron. Hence, this techniques was used to probe different regions of the HPHT synthesized sample to obtain the lattice modes. For this thesis, Renishaw-inVia micro-Raman spectrometer with laser excitation of 514 nm was used.

2.3.4. Studies using density functional theory

Density functional theory (DFT) is a computational modelling method for calculating the ground state of many body quantum systems. The system can be represented by an n-body wave-function. Hohenberg-Kohn proposed a one to one mapping between the wave-function and a functional i.e. spatially dependent electron density. This mapping is

depicted in Hohenberg-Kohn theorem. Hence, the properties of ground state are determined from the electron density. One more interesting and useful theory is Kohn-Sham theory, by virtue of which a complicated quantum mechanical problem of many interacting electrons can be mapped into a system of non-interacting electrons with a modified potential called Kohn-Sham potential. However, as the analytical expression of this potential is unknown and it is only known that there exists such a potential, DFT uses an approximation called exchange correlation function which is chosen to describe the real interaction. The exchange correlation function is approximated generally using local density approximation (LDA) and general generalized gradient approximation (GGA). In GGA, in addition to local electron density, the local gradient in the electron density is considered. Different exchange correlation functions, for example, those proposed by Perdew, Burke and Ernzerhoff (PBE), Perdew and Wang (PW) or Wu and Cohen (WC) are used. In the case of LDA, the functions have been given by Vosko-Wilk-Nusair (VWN), Cole-Perdew, Perdew and Wang, Ceperly and Alder Perdew and Zinger (CAPZ) are used [123].

With GGA-PBE, the compressibility behaviour of Ni_2B and Mo_2B was predicted with good accuracy [55, 124]. However, in case of TaB_2, LDA-CAPZ and GGA-WC give better result as compared to GGA-PBE [10]. Spin polarized GGA with PBE functional works well for CrB under high pressure [125]. DFT study of VB, TaB and TiB_2 under high pressure have been carried out and the details are presented in chapter 3. In addition, the thermodynamic, elastic and dynamic stabilities of the HPHT synthesized TMCs are discussed in chapter 4 and 5.

Chapter 3

Compressibility behavior of VB, TaB and TiB$_2$

3.1. Introduction

As discussed in section 1.2.3, group 4B and 5B transition metal borides show higher stability due to greater cohesive energies and may show better incompressibility behaviour [63, 126]. Hence, the objective of the study presented in this chapter was to investigate the 5B monoborides VB and TaB and the group 4B boride TiB$_2$.

DFT studies on borides of group 5B elements V, Nb and Ta have predicted that for the stoichiometries TM$_2$B, TM$_3$B$_2$, TMB, TM$_3$B$_4$, TM$_5$B$_6$, TM$_2$B$_3$ and TMB$_2$ the tantalum borides have higher bulk moduli as compared to those of vanadium and niobium borides. But, among them, for the stoichiometries TM$_5$B$_6$, TM$_3$B$_2$, TM$_2$B and TMB, the bulk moduli of niobium borides are lower than those of vanadium borides [127]. The study has also asserted that both incompressibility and thermodynamic stability improve with increasing boron concentration for the borides of V, Nb and Ta. In the case of titanium borides too, computational study has reported the bulk modulus to increase with increasing boron content [127, 128].

Bulk modulus of TiB$_2$ has been experimentally estimated by various techniques *viz.* ultrasonic wave propagation methods, shock-wave experiments and study under static pressure [50, 54, 129-136]. However, there is a large spread in the reported values i.e. from 193 GPa to 399 GPa.

This chapter will discuss the studies of bulk and linear compressibility behaviour of VB, TaB and TiB$_2$ using HPXRD as well as *ab initio* electronic structure calculations and the following points will be addressed: (i) compressibility behaviour of 5B monoborides VB and TaB and, their comparison (ii) the compressibility behaviour of AlB$_2$ type TiB$_2$,

the large spread in its reported bulk modulus and the trend in bulk modulus values of diborides along the *3d* series and 4B group (the literature data is used). For the study, TaB and TiB_2 were procured from sigma Aldrich and VB was synthesized.

3.2. Study of VB and TaB under high pressure

3.2.1. Synthesis of VB by arc melting method

VB was synthesized from elemental vanadium and boron using a tri-arc furnace (described in section 2.2.1). For the synthesis of pure phase, a three step process was followed. The steps are arc melting and two stage annealing treatments. At first, boron powder was pelletized and arc melted in a tri arc furnace. Then, vanadium pieces along with the boron pieces were taken in the atomic weight ratio of 1:1.22. Excess boron was taken to compensate for the boron loss which occurs during the arc melting process. The total weight of starting material taken was 1.775g and the weight loss was 0.219 g i.e. ~12%. The ingot was annealed at 1000°C for 4 days. Then, the annealed ingot was thoroughly powdered using mortar and pestle to improve the homogeneity. The powder was then pelletized. Annealing was performed for the second time at 1000°C for 4 days on the pellet to obtain VB. The phase purity was checked at each step by XRD using laboratory based sources – a 18 kW rotating anode X-ray generator ($\lambda = 0.7107$ Å) and a micro-focus X-ray generator ($\lambda = 0.711$ Å) [137].

The XRD patterns of the melted ingot and the sample after first annealing are shown in figure 3.1. The arc melted ingot contained an impurity phase V_5B_6 (ICDD PDF # 00-023-0716) along with VB. From the relative intensities of VB and V_5B_6 phases, an improvement in phase fraction of VB could be observed after first annealing. However, the impurity phase was still persistent. The XRD pattern of the sample after second annealing is presented in figure 3.1 showing the formation of pure VB phase.
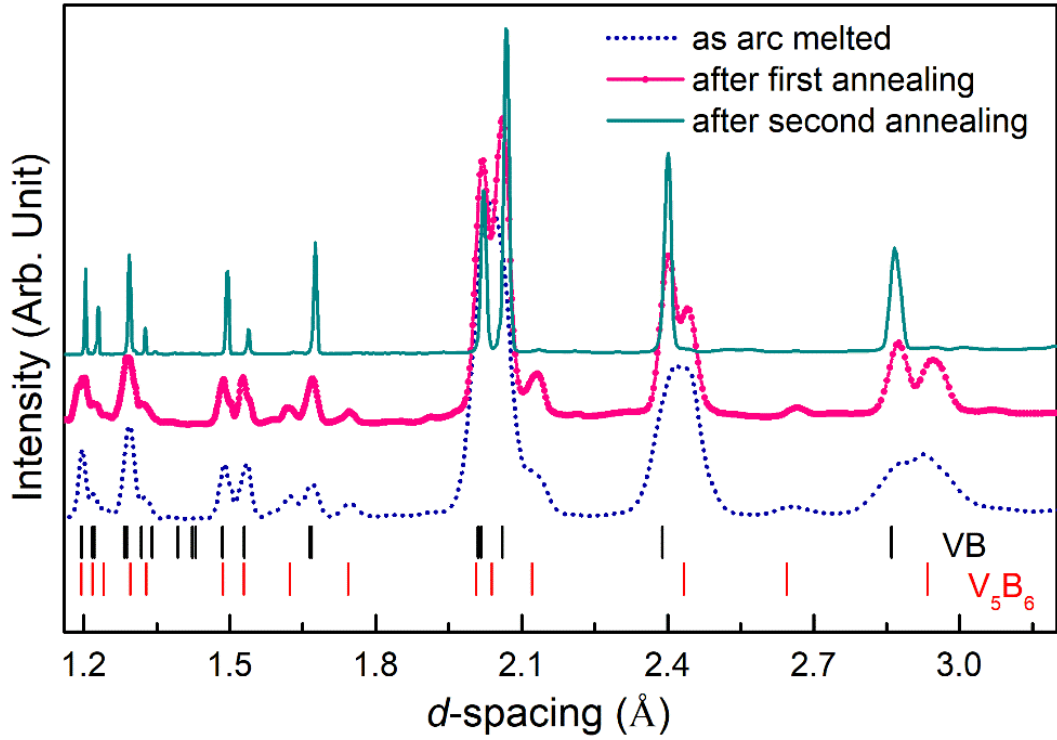
Figure 3.1: XRD pattern of sample: as melted and after two stages of annealing. First annealing was performed on the melted ingot at 1000°C for 4 days. A pure VB phases was obtained when the annealed ingot was powdered, pelletized and annealed for the 2nd time at 1000 °C for 4 days

VB and TaB samples were characterized in a Debye- Scherrer geometry using synchrotron X-ray radiation ($\lambda = 0.619$ Å) at BL-11, Indus-2, RRCAT, Indore, India. Mar-345 type image plate detector was used for recording the diffraction patterns. LaB_6 was used for the distance calibration. Fit2d software was used to integrate 2D diffraction pattern to 1D (2θ vs. intensity) pattern [138]. FullProf Suite was used for crystal structure determination and VESTA for visualization [139, 140]. Both TaB and VB adopt orthorhombic structure with space group *Cmcm* (63) and lattice parameters $a =3.0594(7)$ Å, $b = 8.0457(6)$ Å, $c = 2.9716(3)$ Å and $V = 73.14$ (2) Å^3 for VB, and $a =3.2776(2)$ Å, $b = 8.6683(6)$ Å, $c = 3.1555(2)$ Å and $V = 89.65(1)$ Å^3 for TaB. Their Rietveld refined ambient XRD patterns are presented in figure 3.2. The peaks are indexed in the figure. In the case of TaB, the

sample contained a minor fraction (~ 7%) of TaB$_2$ as impurity phase along with TaB. The crystal structure of TaB$_2$ was determined to be hexagonal with space group *P6/mmm* (191).
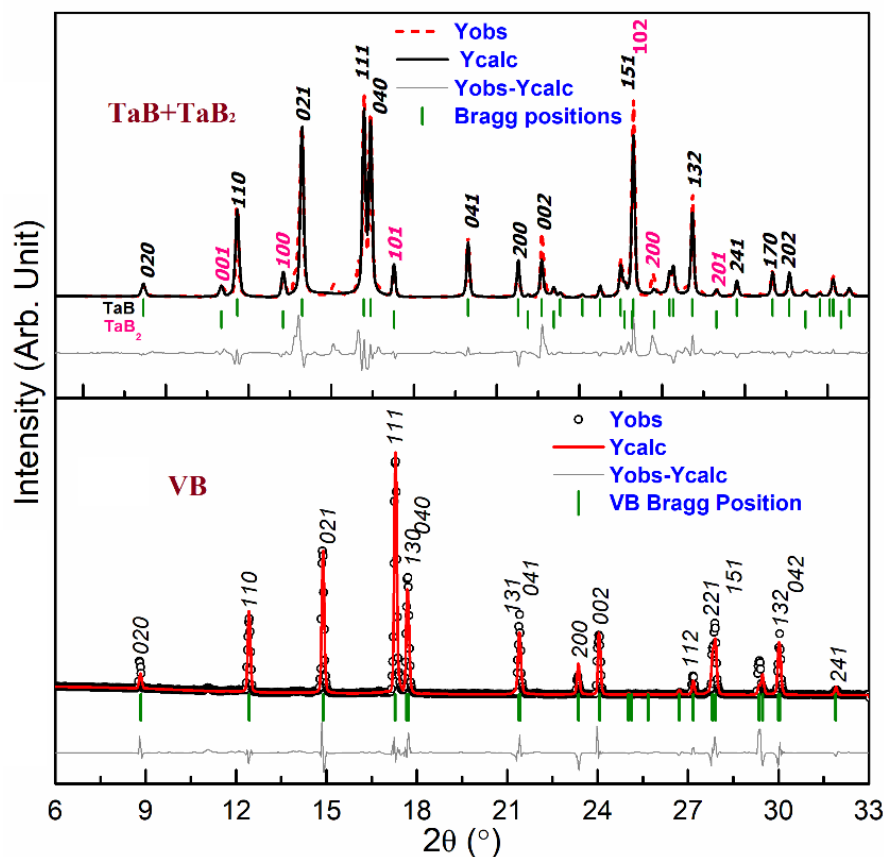
Figure 3.2:   Rietveld refined ambient XRD patterns of VB and TaB samples. The TaB sample contained TaB$_2$ as a minor phase.

The unit cells of VB and TaB are presented in figure 3.3 and the parameters are listed in table 3.1 and table 3.2 respectively. In the unit cells of VB and TaB, the TMs are at *4c* (0, y, 0.25). For VB, the y-coordinate is 0.1475 and for TaB it is 0.1457. The B atoms are also at *4c*. The respective y coordinates are 0.4375 and 0.4508 for VB and TaB. It can be seen that VB and TaB are similar in structure and the projection of atoms in *ab, bc* and *ca* plane are presented in figure 3.4, wherein, the bonds can be seen. The boron atoms form zig-zag boron chain along the *c* axis. The TM-TM bonds are present predominantly along *a* axis and B-B bonds are present along *b* and *c* directions. The TM-B bonds are aligned along all the directions.
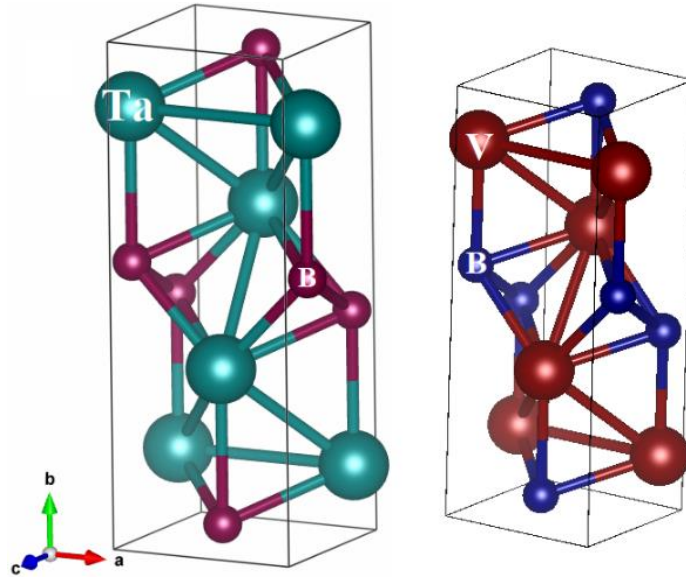
Figure 3.3: Unit cell of TaB and VB. The atoms are labelled in the figures. The bigger spheres are TM and the smaller ones are boron.
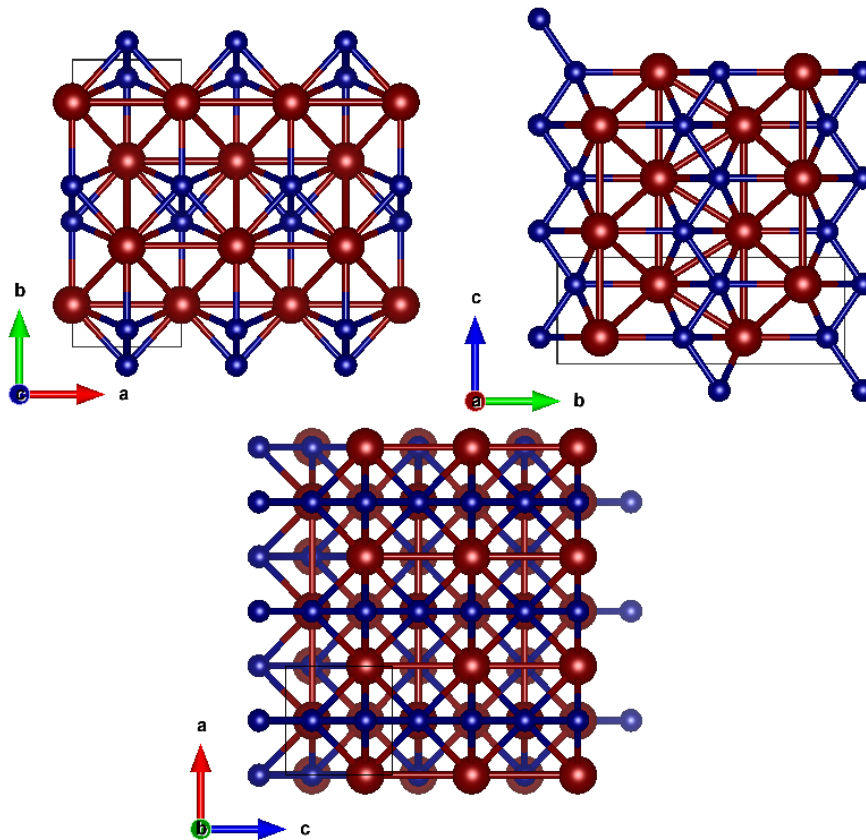
Figure 3.4: The representational *ab, bc* and *ca* planes of VB and TaB. The TM-TM , TM-B and B-B bonds and their alignment can be seen in the figure.

3.2.2. Stability and compressibility behaviour

High pressure X-ray diffraction studies were performed using synchrotron X-ray radiation. The thickness of pre-indented stainless steel gaskets were about 50 µm and the sample chamber diameter was about 200 µm. MEW was used as PTM and EOS of Pt was used as pressure calibrant. The studies were carried out up to 37.5 GPa for VB and 40.5 GPa for TaB. *Ab initio* electron structure calculations were carried out using pseudo potential plane wave (PPPW) method implemented in Vienna Ab initio Simulation Package (VASP) [141]. Ceperley-Alder-Perdew-Zunger (CAPZ) and Perdew-Burke-Ernzerhof (PBE) functional were used for the exchange correlation potentials in local density approximation (LDA) and generalized gradient approximation (GGA), respectively [142-144]. For the Brillouin zone integration, Monkhorst pack scheme of k-point sampling was used. Employment of plane wave cutoff of 520 eV and $19 \times 19 \times 18$ of k-mesh were found to yield acceptable convergence. The XRD patterns of VB at high pressures are shown in figure 3.5 (a) and that of TaB+TaB$_2$ are shown in figure 3.6. It can be seen in the figures that there is no disappearance of any peak or emergence of a new peak, and the peaks shift towards higher 2θ values with pressure. This implies VB, TaB and TaB$_2$ are structurally stable in the pressure range studied. The unit cell parameters at different pressure were determined for VB, TaB, TaB$_2$ and Pt using FullProf Suite. The lattice parameters of Pt have been used for pressure determination.

The volume compression of VB with pressures is shown in 3.5 (b). The bulk modulus of VB has been estimated by fitting the experimental P-V data to second order Birch- Murnaghan equation of state (BM2 EOS). The experimental and computational bulk moduli of VB are 301(5) GPa and 280.8 GPa, respectively.
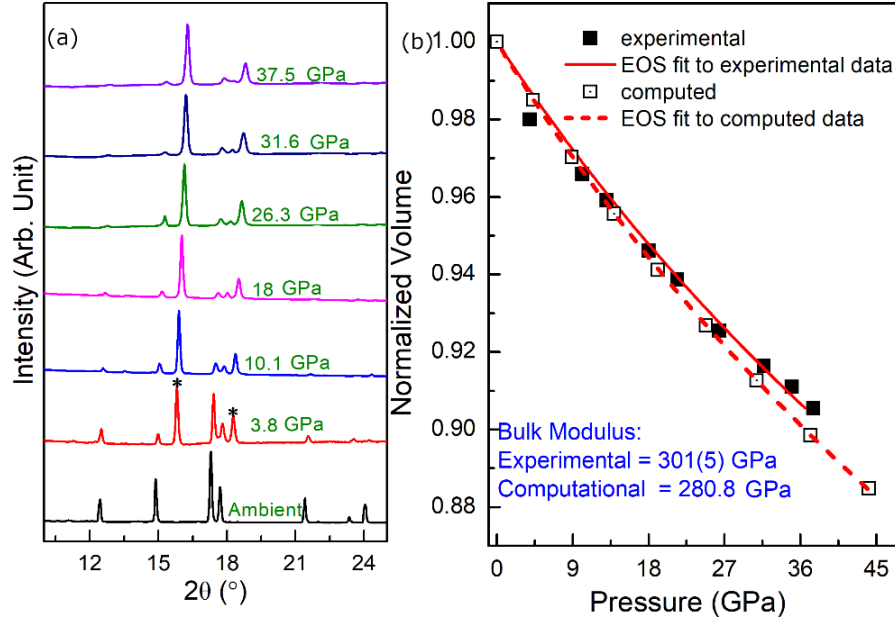
Figure 3.5: (a) HPXRD patterns of VB. The star marked peaks are from Pt (pressure calibrant), (b) volume compressibility of VB. The solid and dashed lines are the BM2 EOS fit to experimental and computational P-V data, respectively.

The pressure versus volume data of TaB obtained experimentally and their comparison with that obtained computationally is shown in figure 3.7 (a). The P-V data of TaB_2 (minor fraction present in the sample) is shown in figure 3.7 (b). The bulk moduli were estimated for both TaB and TaB_2 by fitting the pressure versus volume data to the third order Birch Murnaghan equation of state (BM3 EOS).

The bulk modulus of TaB is estimated to be 366(17) GPa with $B_0' = 4(1.2)$. Hence, compressibility of TaB is also on par with some of the highly incompressible materials like ReB_2, OsB_2 and WB_4.[20, 43, 145] A recent paper reports the bulk modulus of TaB to be 302(4.9) GPa [146]. However, bulk modulus of the minor phase TaB_2 was also determined and found to be 332(16) GPa which is in good agreement with the study by Winkler *et al.*[10] Also from HPXRD plots it can be seen that the shift of TaB_2 peaks with pressure is more compared to that of TaB. Hence, the bulk modulus of TaB is expected to be higher

compared to that of TaB_2 i.e. 332(16) GPa. Moreover, the hydrostatic condition of sample assembly which affects the result is not mentioned in ref 146.
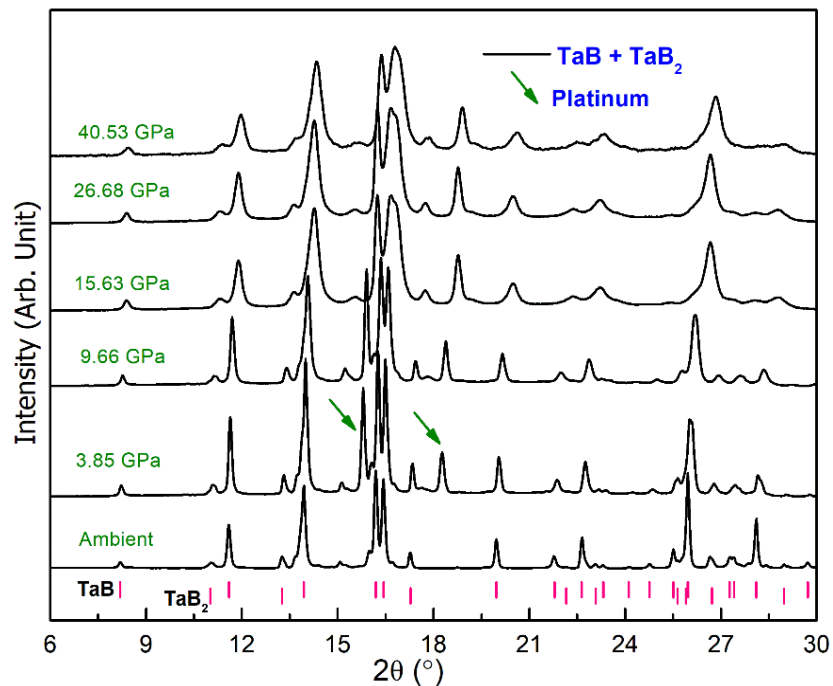
Figure 3.6:   HPXRD patterns of $TaB+TaB_2+Pt$ showing structural stability of TaB and TaB_2. The arrows show the Pt (pressure calibrant) peaks

The theoretical values of bulk modulus for TaB obtained with GGA and LDA are 297.4 and 323.5 GPa, respectively. The experimental and computational bulk modulus values of VB are listed in table 3.1 and those for TaB and TaB_2 are mentioned in table 3.2. It can be seen that TaB is less compressible than VB. A difference between experimental and computational bulk modulus values was noticed for both VB and TaB. Similar differences have also been seen for other borides, for example, TaB_2, CrB and WB_4[10, 56, 125, 147-150]. As mentioned earlier, the experimental bulk modulus value for TaB_2 is 332(16) GPa. However, the theoretical calculation employing pseudo potential plane waves (PPPW) where the exchange correlation potential was described by GGA with Perdew, Burke and Ernzerhoff (PBE) parametrization method approach based on DFT implemented in CASTEP code, gives a value of 297 GPa [147]. But, the study that employs Vanderbilt

ultrasoft pseudopotentials and treats the exchange correlation with LDA developed by Ceperly and Alder and parametrized by Perdew and Zinger (CAPZ) gives a value of 341.5 GPa [148]. Also, with GGA potential by Wu and Cohen (WC), the value comes out to be 336 GPa [10]. In the case of CrB, the experimental bulk modulus is 269(5) GPa. But, the computational study using VASP code with GGA proposed by Perdew and Wang (PW) estimates the value to be 304.8 GPa [56]. However, the study with the spin polarized generalized gradient approximation, PBE functional as implemented in the VASP package estimates a value of 255.3 GPa [125]. For WB_4 the theoretical values with VASP code that uses the projector augmented wave (PAW) method are 360 GPa and 375 GPa with GGA and LDA respectively; whereas the HPXRD study report the value to be 428(4) GPa [149-151]. Hence, the use of other method and/or other exchange correlation potential may give a better matching.
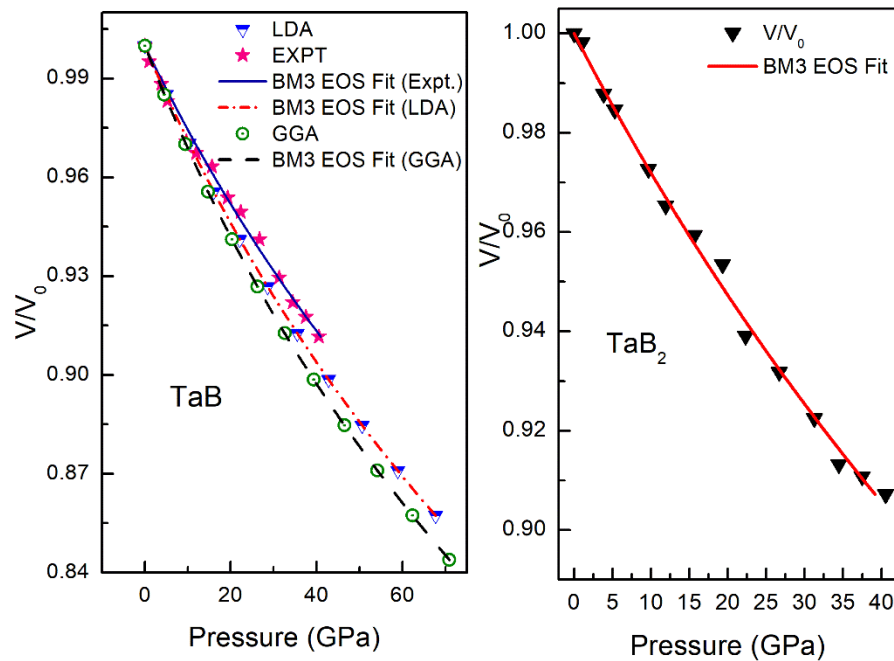
Figure 3.7: (a) Experimental and computed P-V data of TaB. The solid and dashed lines are BM3 EOS fits (b) experimental P-V data of TaB_2. The solid line is the BM3 EOS Fit to the data

In figure 3.8, the bulk modulus of group 5B monoborides estimated by DFT studies by Qi *et al* and Yao *et al* and those estimated in this study are plotted [127, 152].
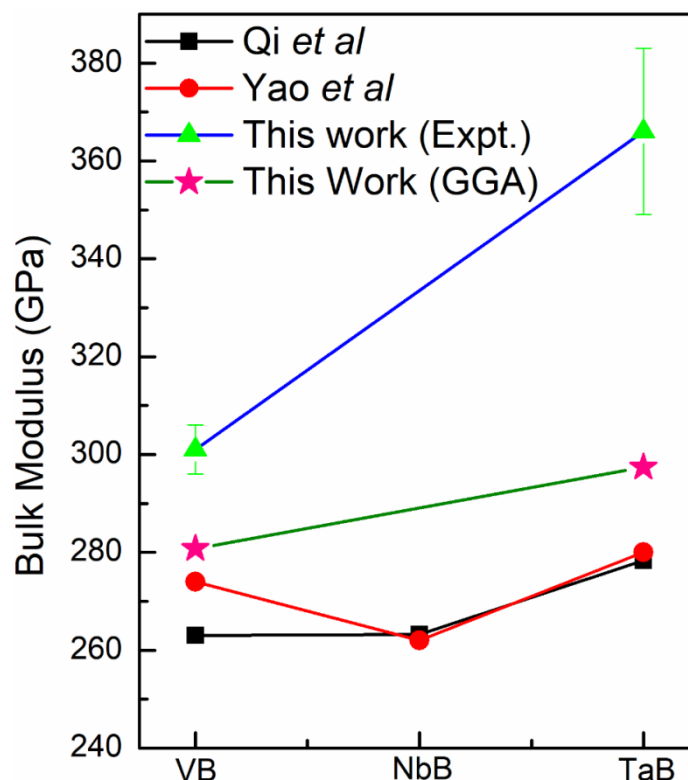
Figure 3.8: Bulk modulus of group 5B monoborides. The trend between VB and NbB is not clear. However, TaB shows a clear increase in bulk modulus from VB and NbB.

It can be seen that the trend between VB and NbB cannot be established. However, in the case of VB and TaB, there is a clear increase in bulk modulus value from the former to latter and the same has been observed experimentally in this study.

The linear compressibility of both VB and TaB have also been studied. The inverse linear compressibilities along *a, b* and *c*- axes were estimated by the method prescribed by Angel [153]. As the BM EOS deals with volume data, the lattice parameters are cubed to get "volume like data". Then BM2 EOS has been fit to pressure versus "volume like data". The obtained bulk modulus is one third of the inverse linear compressibility along the corresponding direction. The experimental and computational linear compressibility is

shown in figure 3.9 for VB. The lattice parameters, bulk modulus and inverse linear compressibility values of VB are listed in table 3.1. It is evident from the inverse compressibility values that the compressibility is highest along a axis. From computation, it is revealed that the compressibility is least along b direction. However, in the case of experimental values, the compressibility along b and c fall within each other's error bar.

Table 3.1: Crystal structure and compressibility data of VB

		Experimental	Computational
Space group: *Cmcm* (63) Lattice parameters (Å)	a	3.0594(7)	3.0412
	b	8.0457(6)	8.0255
	c	2.9716(3)	2.9645
Volume		73.14 (2)	72.36
Bulk modulus (GPa)		301 (5)	280.8(3)
Inverse linear compressibilities (GPa)	along a	842(15)	749.5(4)
	along b	934(16)	903(2)
	along c	943(21)	890.9(8)

Table 3.2: Lattice parameters and bulk moduli of TaB and TaB_2

Phase	Space group	a in Å	b in Å	c in Å	V in Å^3	B_0 (GPa)	$B_0^{'}$
TaB (This work)	*C m c m*	3.2776(2)	8.6683(6)	3.1555(2)	89.65(1)	366 (17)	4.0 (1.2)
Ref [154] (expt.)		3.280(1)	8.670(3)	3.155(2)	89.73(13)	---	---
GGA (This work)		3.2931	8.7080	3.1614	90.66	297.4 (9)	4.02(3)
LDA (This work)		3.2502	8.5981	3.1244	87.32	323.5 (4)	3.98(1)
TaB_2 (This work)	*P6/mmm*	3.095(3)		3.224(4)	26.75(4)	332(16)	3.9(1.1)
Ref [155] (expt.)		3.09803(7)		3.22660(12)	26.82	---	---
Ref [10] (expt.)		3.1018(2)		3.2836(4)	27.360(4)	341 (7)	4

Figure 3.10 shows the lattice compression of TaB under high pressure and their comparison with computational data. The experimental and theoretical inverse linear compressibilities along *a, b* and *c* axes are listed in table 3.3. The compressibility is least along *c* axis. The theoretical study by Chen *et al* had predicted the compressibility to be highest along *b* axis [156]. However, it can be seen both experimentally and theoretically that the unit cell is compressible the most along *a* axis.
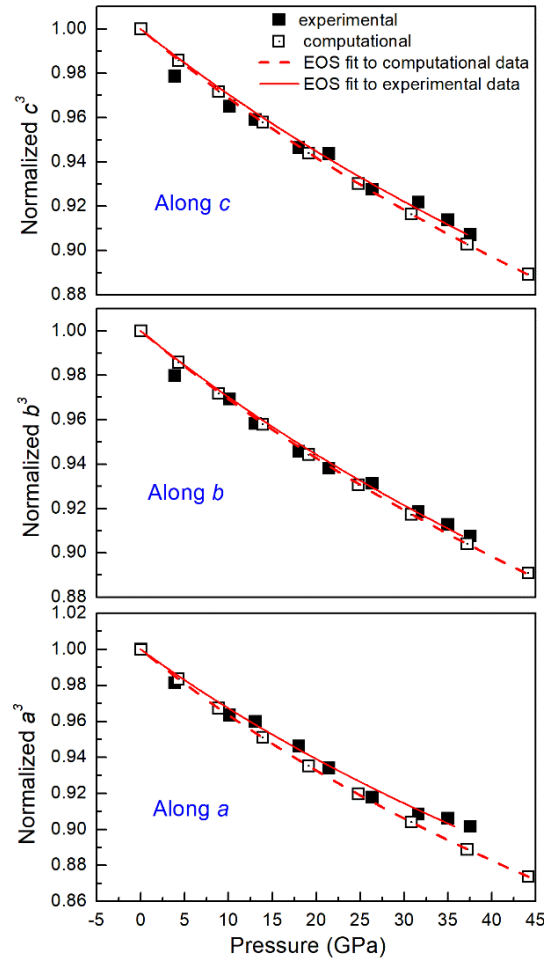
Figure 3.9:   Linear compressibility of VB along a, b and c - direction. The lattice is most compressible along a axis.

3.2.3. Electronic Properties

The electronic properties of VB and TaB have been studied using DFT. Their density of states (DOS) were calculated and are plotted in figure 3.11. The DOS is finite at the Fermi level which infers that both VB and TaB are metallic. A pseudogap at Fermi level can be

noticed as in the case of few transition metal diborides. This suggests high structural stability for both of them [126]. The formation of pseudogap can be attributed to two mechanisms. One is of hybridization effects and another is due to ionicity. There is an overlap of *d* orbital of the TM and B *p* orbital inferring strong hybridization between them and in turn the covalency of TM-B bond [157]. To understand the nature of bonds in VB and TaB, the charge distribution in their unit cell was studied.
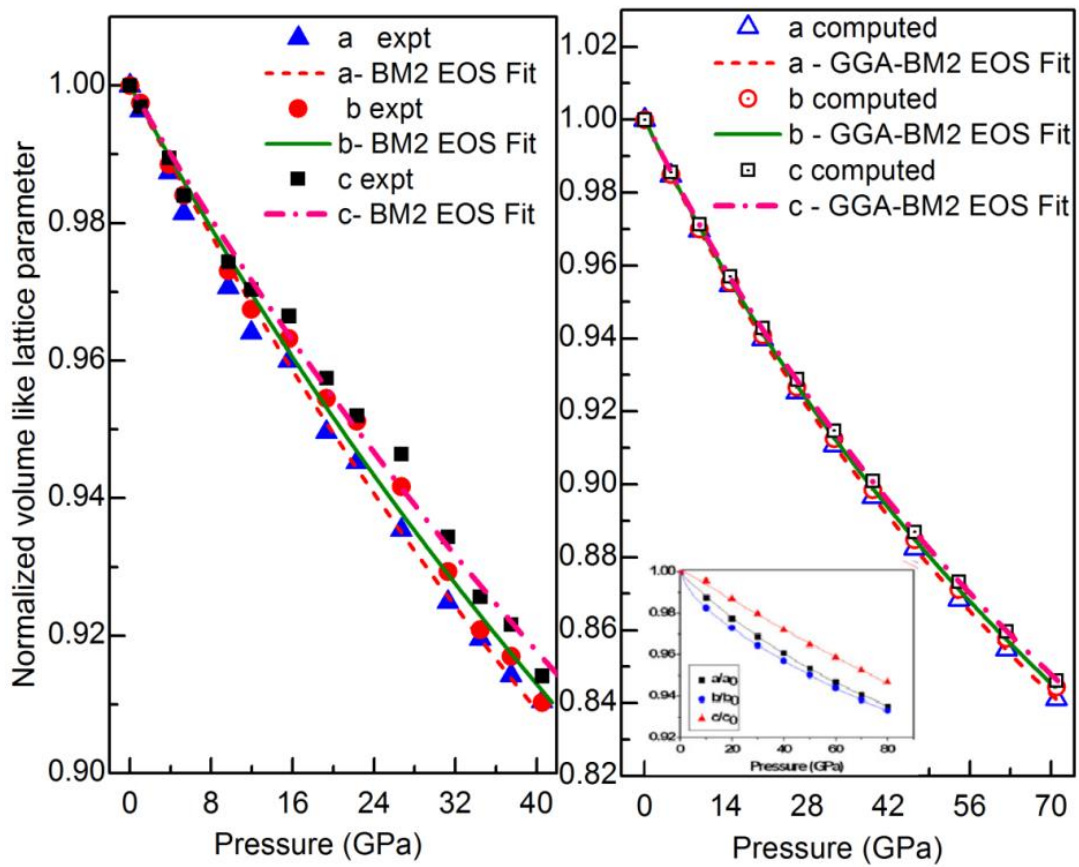
Figure 3.10: Variation of lattice parameters of TaB with pressure and their comparison with computational values. The cell is most compressible along a axis and the least along c axis. The inset shows the lattice compressibility behaviour from ref 156.

Table 3.3:   Inverse linear compressibility of TaB

	Along *a* (GPa)	Along *b* (GPa)	Along *c* (GPa)
Expt.	1042	1098	1177
GGA-PBE	868	893	914
LDA-CAPZ	949	976	984

In figure 3.12, charge density distribution along the *(-100)* plane of VB and *(100)* plane of TaB are shown. In the figure, blue colour indicates the highest charge density and red the lowest. Finite, low and uniform charge distribution between the metals indicates metallic bonding between them. The metallic bonding between TM-TM is the major reason for metallic behaviour of VB and TaB. High charge accumulation between B-B bond implies it to be covalent in nature [158]. However, the charge density along B-B bond is higher in case of TaB which infers stronger covalency compared to that in VB. This may be another reason for higher bulk modulus of TaB. There is a charge transfer from metal to boron. The transfer seems to be more between Ta and B compared to that between V and B. Hence, it can be said that, the *p-d* hybridization of TM and boron electrons and the partial ionicity of TM-B bond are the reasons of pseuodogap formation.

Now, the axial compressibility can be understood in terms of the bond nature and the bond alignments in the unit cell. In figure 3.4, it was seen that, the metallic bonds are present predominantly along *a* direction and also there is an absence of B-B covalent bonds along the same. This justifies the highest compressibility along *a* axis. The compressibility along *b* and *c* directions are almost of equal order and that have been dictated by the bond strengths of B-B and TM-B bonds.

3.2.4. Elastic Properties

The mechanical stability of VB and TaB have been studied and elastic constants have been determined at ambient as well as high pressures. There are 9 independent elastic constants for orthorhombic system. Their elastic constants at ambient are listed in table 3.4.
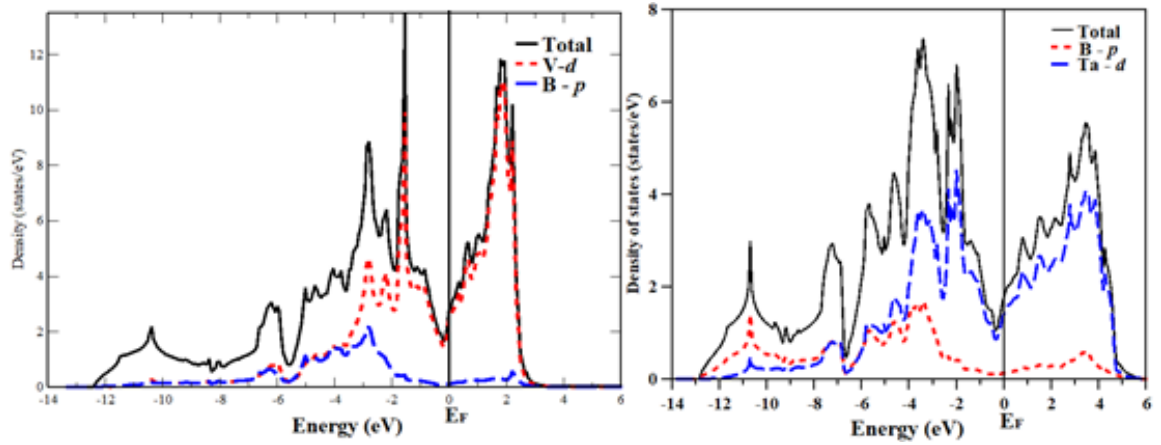
Figure 3.11:   DOS of VB (left) and TaB (right) showing their metallic nature and
the strong p-d hybridisation between the TM and B electrons.

Table 3.4:   Elastic stiffness constants of VB and TaB at ambient and the elastic
moduli

	Elastic Constants								
	C_{11}	C_{12}	C_{13}	C_{22}	C_{23}	C_{33}	C_{44}	C_{55}	C_{66}
VB	509.1	132.4	158.4	648.9	78.2	622.4	209.7	211.2	281.9
TaB	521.5	163.5	194.2	569.4	147.1	561.0	236.4	205.0	266.4
	Bulk modulus		Shear modulus	Young's modulus		B/G ratio		Poisson's ratio	
VB	279.88		234.67	550.22		1.19		0.17	
TaB	295		218	525		1.35		0.204	

The variation of elastic constants with pressure is shown in figure 3.13. The elastic
constants were found to satisfy Born criteria for orthorhombic structure showing elastic
stability of the structure both at ambient and high pressures [159]. The bulk modulus (B), shear
modulus (G) and Young's modulus (E), Pugh ratio (B/G) and Poisson's ratio were
estimated for both of them by Voigt approximation method and are listed in table 3.4 [160].
According to Pugh's criteria, if the B/G ratio and Poisson's ratio are greater than 1.75 and
0.26, respectively, then the material is ductile and malleable [161, 162]. Hence, VB and TaB
are not ductile or malleable in nature.
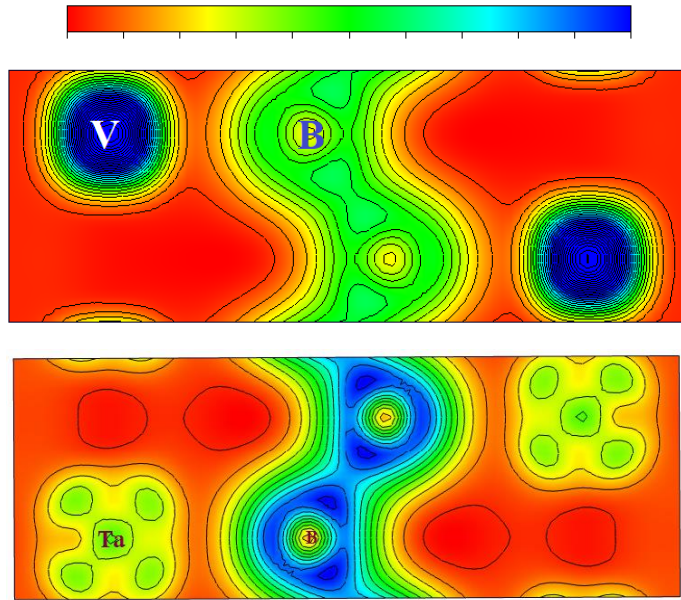
Figure 3.12:   Charge distribution along *(-100)* plane of VB (top) and *(100)* plane of TaB (bottom)
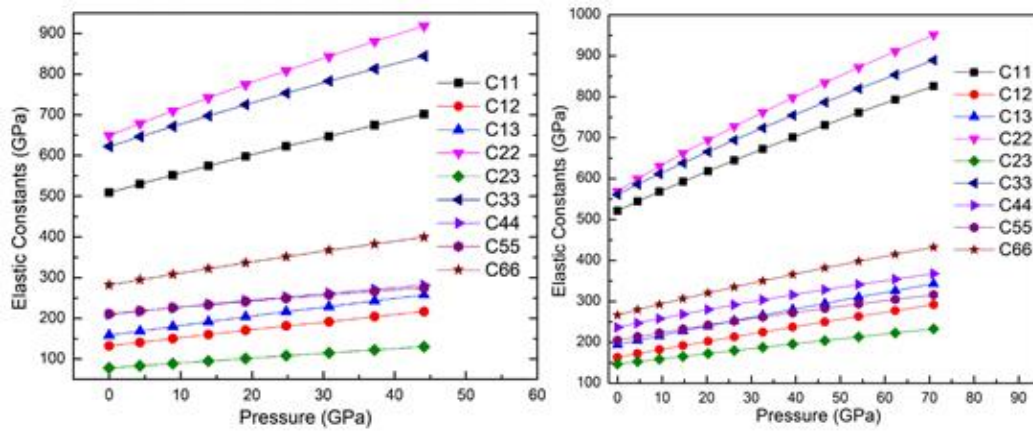
Figure 3.13:   Variation of elastic constants of VB (left) and TaB (right) with pressure

3.3. Behaviour of TiB$_2$ under high pressure and the change in rate of bond compression

The following sections describe the behaviour of diboride of TiB$_2$ under high pressure. The study was carried with the objective to address the high spread in bulk modulus value reported in literature (193 GPa to 399 GPa). At this stage it is apt to discuss

the structure and properties of TiB_2 and nature of incompressibility behaviour one can anticipate for it.

TiB_2 crystallizes in AlB_2 type structure i.e. a hexagonal lattice with space group no. 191 (P6/mmm). Both titanium and boron occupy special positions viz $1a$ (0, 0, 0) and $2d$ (0.33, 0.67, 0.5), respectively. The lattice is a layered one consisting of graphite like boron layer intercalated between layers of Ti metal. However, studies based on electronic structure calculation have reported that TiB_2 cannot be considered as a traditional layered compound due to the presence of strong interlayer interactions. Further, these interactions get enhanced under pressure suggesting a 3D character [126, 163, 164]. Also, the consistency of this proposed interlayer interaction has been verified experimentally for VB_2 and ZrB_2, which share the AlB_2 family with TiB_2 [51]. Hence, a high value of bulk modulus is expected for TiB_2 in accordance with its high hardness (33 GPa) and the notion is strengthened by invoking a strong interlayer interaction. The study also revealed a rate of change of bond length with pressure around 12 GPa. The reason for this change has been understood with the aid of *ab initio* electronic structure calculation.

3.3.1. High pressure XRD study

Powdered sample of TiB_2 from Sigma-Aldrich was used to carry out high pressure studies. Prior to the high pressure studies, the phase purity of the pristine sample was confirmed by XRD using in-house micro focus x-ray diffraction setup with Mo target ($\lambda = 0.711$ Å) [137]. HPXRD experiments were carried out using the RAXRG ULTRAX ($\lambda = 0.7107$ Å) and mar-345 image plate detector. Pressure was estimated from the shift of the position of R1 line of ruby fluorescence spectra. MEW was used as PTM. Figure 3.14 shows the Rietveld fit of the ambient XRD pattern of TiB_2 using GSAS+EXPGUI [165, 166].
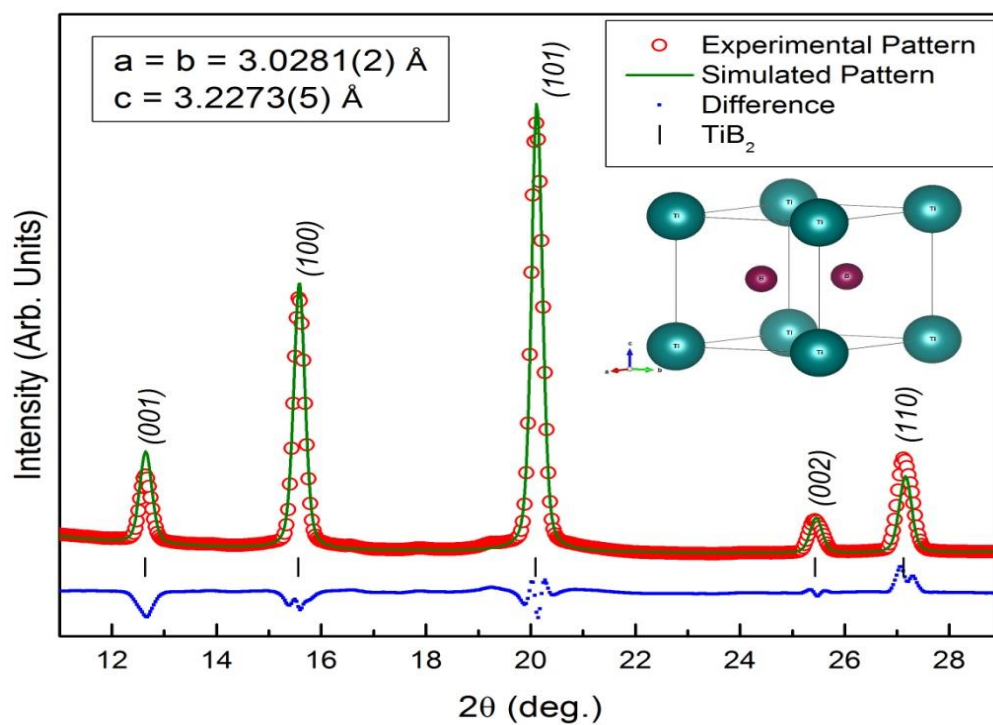
Figure 3.14:   Rietveld fit of ambient XRD pattern of TiB$_2$. The inset shows the unit
cell of TiB$_2$ (space group 191), Ti is at *1a* and B is at *2d*.
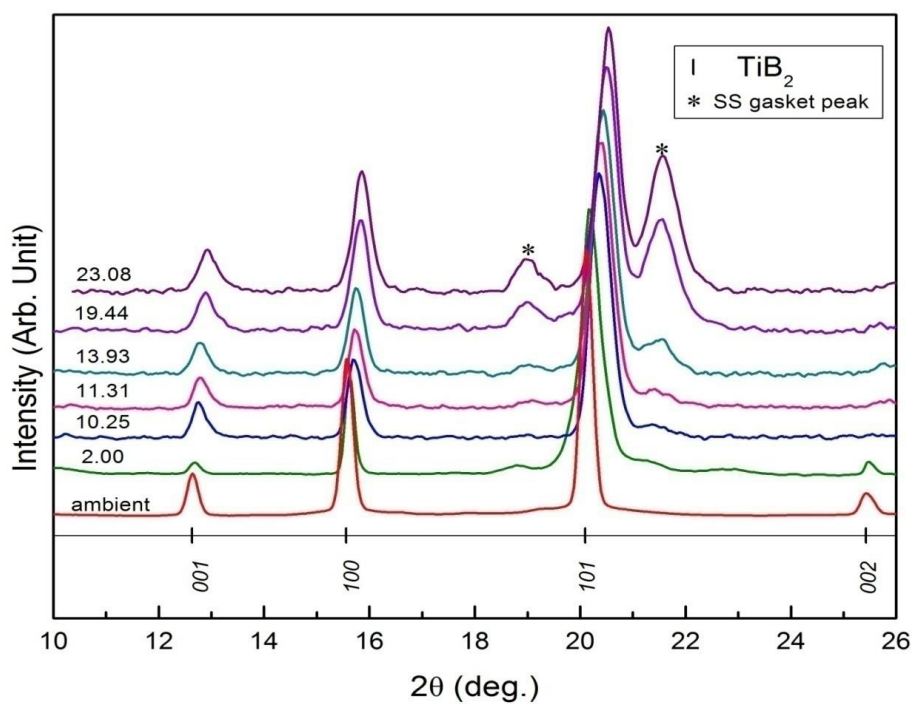
Figure 3.15: HPXRD patterns of TiB$_2$ confirming structural stability up to 23 GPa. The
peaks marked with asterisks are due to SS gasket

The lattice parameters were found out to be $a = b = 3.0281(2)$ Å and $c = 3.2273(5)$ Å with ambient unit cell volume $V_0 = 25.629(4)$ Å^3. The lattice parameters obtained are in good agreement with those in ICDD pdf # 00-035-0741 [167]. Figure 3.15 shows the HPXRD patterns of TiB$_2$. As expected, the hexagonal lattice was stable in the pressure range studied and only a systematic shift of Bragg peaks towards higher 2θ angles was seen. The peaks marked with asterisks which show up after 13 GPa were confirmed to be due to the SS gasket. The lattice parameters and the corresponding unit cell volume were estimated in same manner at each pressure. The bulk modulus was estimated by fitting the experimental pressure vs. volume data with BM3EOS. The fitting carried out with B_0 and B_0' as variables, resulted in physically unreasonable values of B_0' (7.89 ± 4.15). Hence, B_0' was fixed with literature reported values as 1.89 [136], 3.86 [54] and 4 [50]. Considering the large spread in bulk modulus values reported earlier, for a good estimation of order of bulk modulus value, the EOS fitting was also done with Murnaghan type EOS (equation 1) and Rose-Vinet EOS (equation 2).

$$P(V) = \frac{B_0}{B_0'}\left[\left(\frac{V}{V_0}\right)^{-B_0'} - 1\right] \qquad \text{---- (1)}$$

$$P = 3B_0\left(\frac{1-\eta}{\eta^2}\right)e^{\frac{3}{2}(B_0'-1)(1-\eta)} \text{------ (2),}$$

$$\text{where } \eta = \left(\frac{V}{V_0}\right)^{1/3}$$

The bulk modulus values obtained by fitting to the above equation of states are tabulated in table 3.5. Figure. 3.16 shows the EOS fitting of the pressure-volume data. The inset shows the B_0 values obtained at different selected B_0'. B_0' of 1.89 is from shock wave measurement whereas the values 3.86 and 4 are from static pressure experiments [50, 54, 136]. Also, B_0' of 4 is routinely reported for TMBs. Hence, bulk modulus of TiB$_2$ is estimated to be 333(6) GPa.
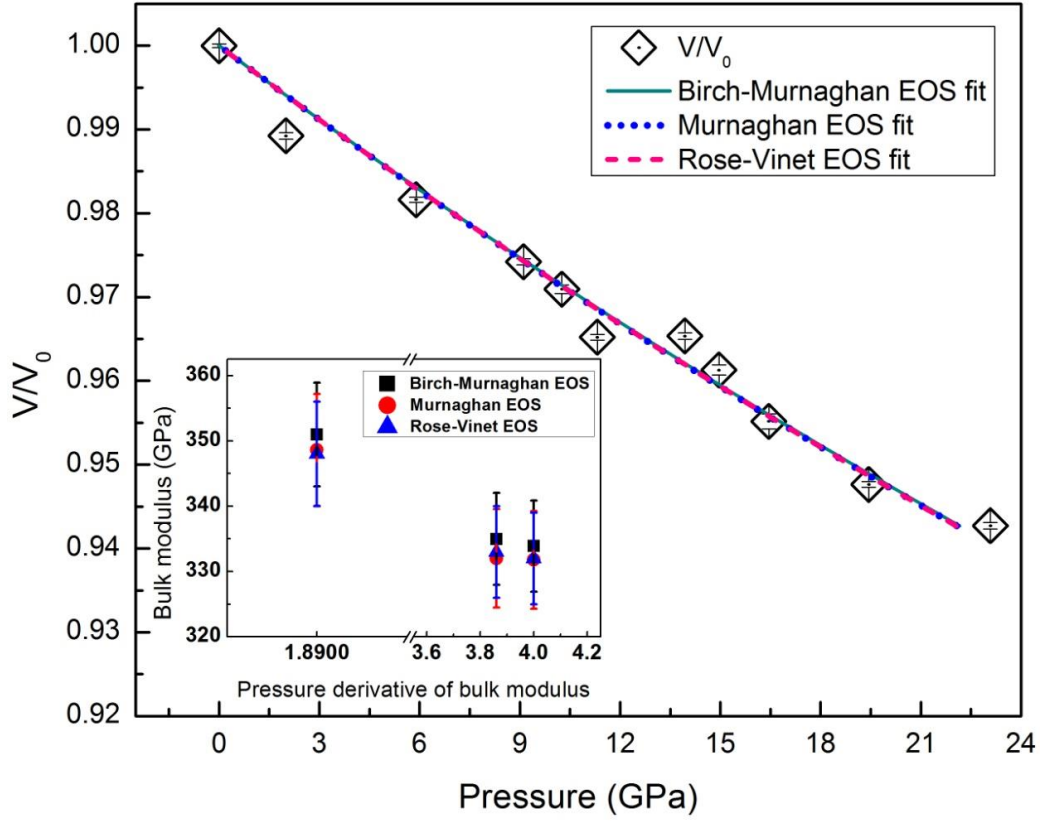
Figure 3.16:   EOS fit to the experimental pressure vs. volume data. The inset shows the bulk modulus values obtained at different fixed B_0'

Table 3.5:   Values of bulk modulus obtained by fitting the experimental data to different EOS

B_0'	B_0 (GPa)		
(fixed)	3rd order Birch-Murnaghan	Murnaghan	Rose-Vinet
1.89	350(7)	348(8)	348(8)
3.86	334(7)	332(7)	333(7)
4	333(6)	331(7)	332(7)

The lattice compressibility values for 'a' and 'c'- axis have been estimated using the method described by Angel [168]. In figure 3.17, the lattice compressibility of TiB_2 is shown.

The lattice compressibility values obtained for *'a'* and *'c'* axis are $\beta_a = 0.93(2)$ TPa^{-1} and $\beta_c = 1.14(2)$ TPa^{-1}, respectively. The compressibility along *c*- axis is more as compared to that along *a*- axis showing anisotropic compressibility behaviour. Similar anisotropic compression is also seen in isostructural VB$_2$, MgB$_2$, HfB$_2$, CrB$_2$, MnB$_2$ and AlB$_2$ [18, 169-173].
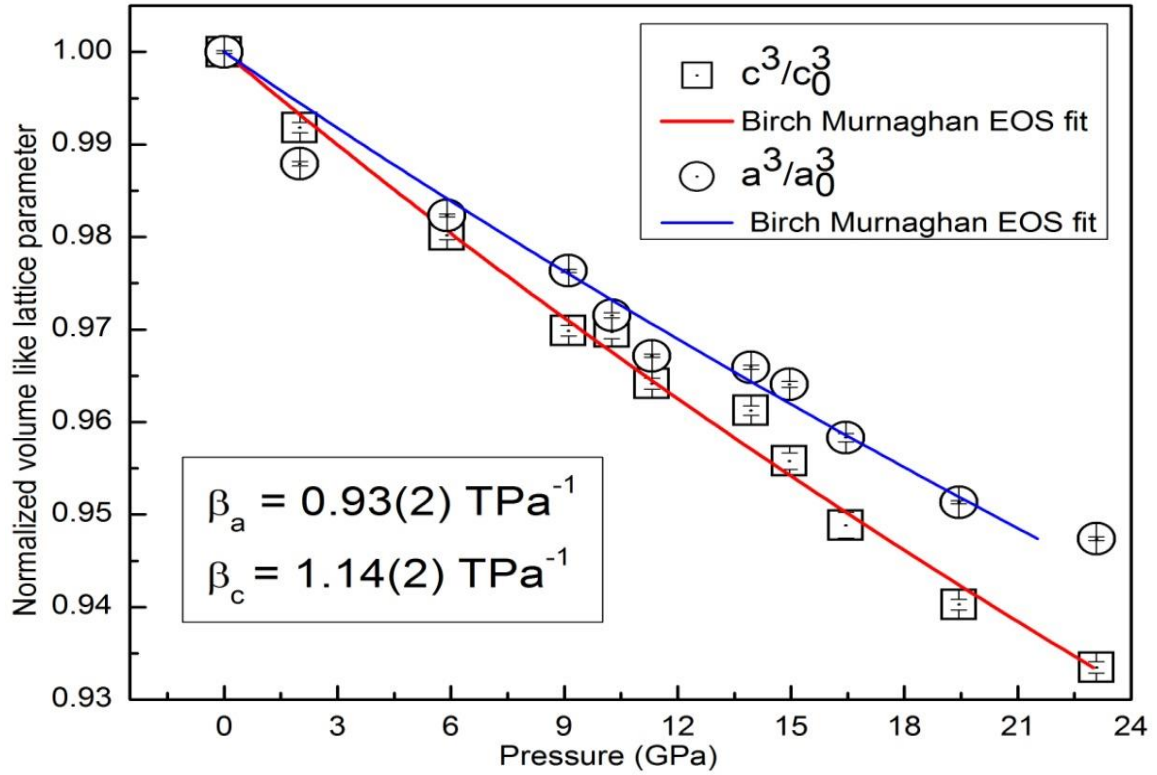
Figure 3.17:   EOS fit to pressure vs. normalized volume like lattice parameter data

The experimental bulk modulus values for TiB$_2$ published earlier are tabulated in table 3.6 along with the nature of sample and the measurement method. It is evident from table 3.6 that with the exception of the study by Dodd *et al.* and Gilman *et al.,* ultrasound measurements give a value of about 250 GPa or quite less than that whereas the shock wave experiments and our study report higher values [131-133, 175].

Table 3.6:   Compilation of bulk modulus value for TiB$_2$ from various studies

Author	Nature of sample	Experimental method		Bulk modulus (GPa)
Grady [175]	Polycrystalline		-	193.1 [a]
Manghnani [b]	Polycrystalline		Ultrasonic wave velocity	238.9 [a]
Wright [b, 131]	Textured polycrystalline sample [c]	**Other Methods**	Pole figure measurement	194.3 [d] 237 [e]
Tatro and Green	Hot pressed polycrystalline sample		Ultrasonic wave	251 [f]
Wiley [g, 132]	Hot pressed polycrystalline bar		Sonic resonance method	208
Spoor [b 133]	Single crystal		Resonant ultra sound spectroscopy	240.4
Dodd [134]	Piece of ceramic sample		Pulse echo overlap method	276
Gilman [b130]	Single crystal		Pulse echo method	399
Gust [136]	Hot pressed		Shock wave	346 [h]
LASL Shock Hugoniot Data [176]	---	**High Pressure methods**	----	323 [h]
Waskoska [50]	Single crystal		High pressure EDXRD	260
Present study	Polycrystalline		High pressure ADXRD	333

a   as described in reference [131]

b   calculated from measured stiffness constants

c   same sample as used by Manghnani *et al* after correction for texture

d	single crystal elastic constants were estimated on the basis of Voigt polycrystal - average formulation
e	single crystal elastic constants were estimated on the basis of Reuss polycrystal - average formulation
f	as described in reference [136]
g	calculated from measured Young's and shear modulus
h	as described in reference [135]

The large difference in B_0 between ultrasonic measurement and high pressure measurement are often reported in literature. For example, in the case of ZrB_2 (AlB_2 type), ultrasonic measurement and HPXRD measurement estimate B_0 to be 240 and 317 GPa respectively [169, 177]. Also, in WB (tetragonal), ultrasonic measurement estimates B_0 to be 266 GPa whereas HPXRD estimates a value of 452 GPa [57, 178]. However, high pressure EDXRD measurement on TiB_2 yields a low value of bulk modulus as compared to the values reported by other high pressure techniques [50]. The possible reason for this may be the inherent limitation on spatial resolution in EDXRD.

Shock wave measurements by Gust *et al* and the LASL Shock Hugoniot data have reported bulk modulus value to be 346 and 323 GPa respectively and the elastic constant measurement on TiB_2 by pulse echo method estimates B_0 to be 399 GPa; which are in good agreement with the B_0 value obtained by this work [136, 179]. Also, an electronic structure calculation using self-consistent LMTO-ASA has reported the bulk modulus value to be 370 GPa [180]. The electronic structure calculation for *3d* transition metal borides (TMB_2) shows that in DOS plot of TiB_2, the fermi level (E_F) lies in a pseudo gap and falls near the minima which infers ,high stability and high cohesive like properties [126, 128, 181].
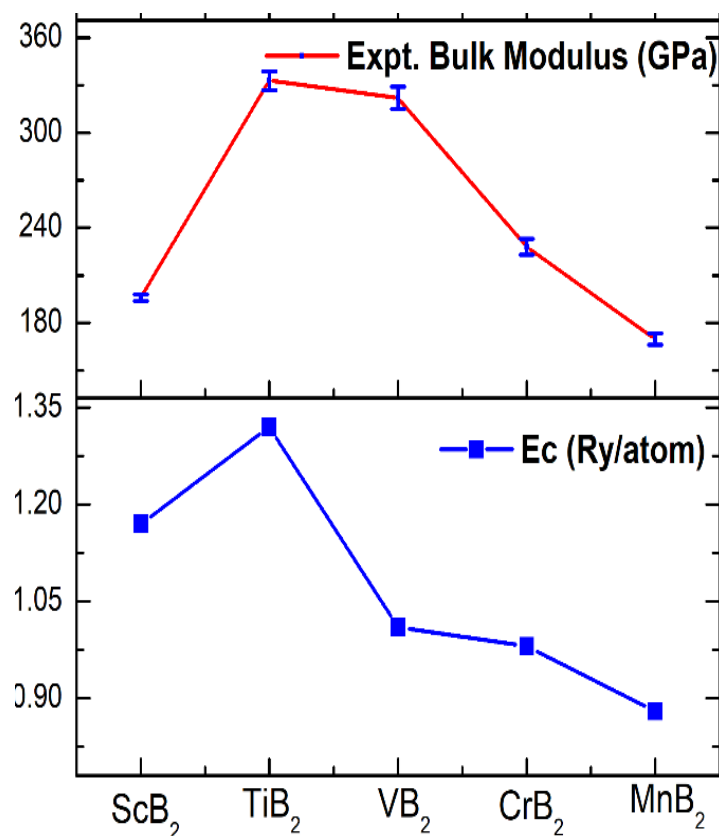
Figure 3.18: Trend of bulk modulus of *3d* transition metal diborides. The bulk
modulus follows the trend of cohesive energy

In the case of *3d* TMB$_2$s, the cohesive energy (E$_C$) is maximum for TiB$_2$ due to highest band filling effect and suggest maximum stability for the compound [126]. The experimental B_0 reported for ScB$_2$, TiB$_2$, VB$_2$, CrB$_2$, and MnB$_2$ are 196, 333 (present study), 322, 228 and 169 GPa, respectively [18, 50, 169, 172]. In figure 3.18, E$_C$ and the experimental bulk modulus of the diborides of *3d* elements are plotted and the same for group 4B diborides are potted in figure 3.19. They both follow similar trend and the bulk modulus estimated in this study fits well into the trend implying the reliability of the value.

The bond length variation for Ti-B and B-B bond with pressure is shown in figure 3.20. The overall reduction in bond length has been found to be 2.007% and 1.785% for Ti-B and B-B respectively up to 23 GPa. In the plot, a change in rate of contraction of bond length was noticed around 12 GPa. The rate of change in Ti-B bond length across the two

regions are -0.00233(1) and -0.0020(2). In the case of B-B bond length, the change is –0.00163(9) to –0.0013(1). From this, it is clear that the rate of change of bond length has decreased after 12 GPa for both Ti—B and B-B bonds. To explore the reason behind this, ab initio electronic structure calculation has been carried out.
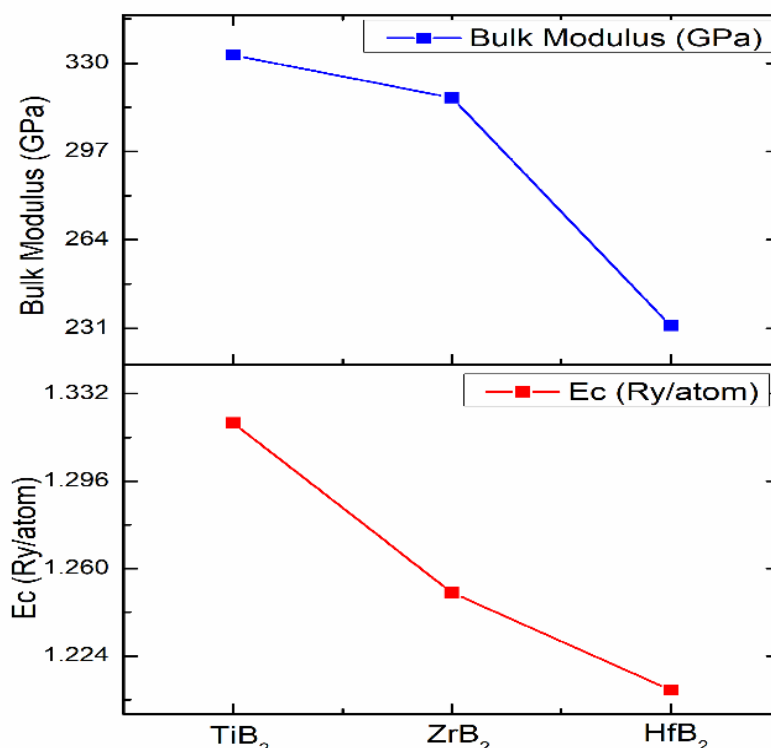
Figure 3.19:   Trends bulk modulus along the group 4B TMB_2s. Their bulk modulus follow the trend of cohesive energy.

3.3.2. Ab initio electronic structure calculation

First principle electronic structure calculations were carried out based on the pseudo potential plane-wave (PP-PW) method implemented in CASTEP code and the other is the full potential linearized augmented plane wave method (FP-LAPW) implemented in WIEN2k [182-186]. Geometrical optimization and charge density have been performed for one unit cell using the PP-PW method and electronic structure calculations have been carried out using the FP-LAPW method implemented in WIEN2k computer package. In this

method the unit cell volume is divided into muffin tin (MT) spheres and interstitial region. In the muffin tin spheres, atomic orbitals and spherical harmonics are used to expand the wave function, whereas in the interstitial region the wave function is expanded by using the plane waves. The cut-off angular momentum quantum number value (inside the muffin tin sphere) is set to $l_{max} = 10$ and interstitial wave function is expanded with a cutoff $K_{max}=8/R_{mt}$, where R_{mt} is the smallest muffin tin radius. The charge density and potentials expanded up to $G_{max} =12$. 23×23×18 k-mesh with 560 k-points in irreducible Brillouine zone (IBZ) has been used for k-space integration for the electronic structure calculation. Systematic first principles calculations have been carried out to see the pressure effect (around 12 GPa) in the pressure range (0 to 22 GPa) with step size of 2 GPa.

To see the trend in the rate of change of bond length, linear fitting to the theoretical bond length data for both Ti-B and B-B bonds was done which is shown in figure 3.21. For B-B bonds, the slope (compressibility) is -0.00184(2) for the range 0 to 12 GPa and that for the range from 12 to 22 GPa is -0.0061(3). In case of Ti-B bonds, the compressibility below 12 GPa is -0.00306(3) and that above 12 GPa is -0.00258 (2). This clearly implies both B-B and Ti-B bonds are hardening at 12 GPa which was also seen in the experiment.
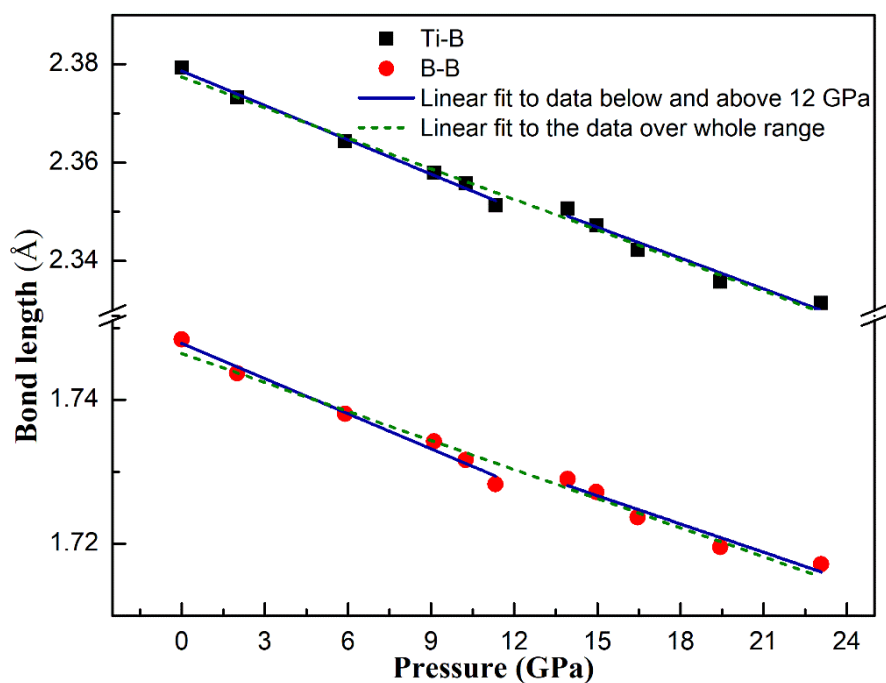
Figure 3.20: Variation in Ti-B and B-B bond lengths with pressure. The solid and dashed lines are the linear fit to the experimental data
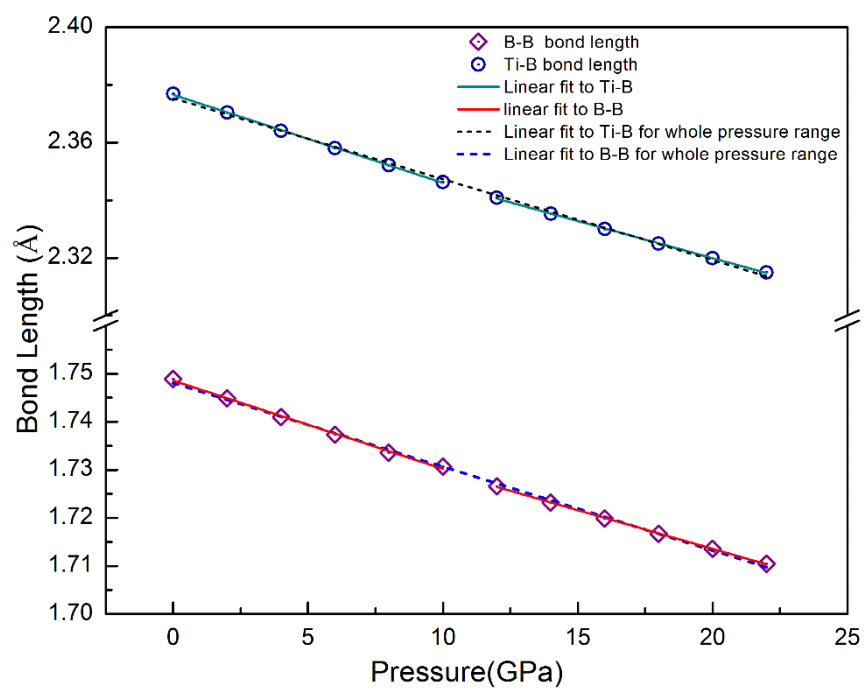
Figure 3.21: Variation of computed bond lengths of TiB_2 with pressure. The change in slope at 12 GPa suggests bond hardening for both B-B and Ti-B bonds.

The variation in rate of bond compression observed in the present calculation and also in the experiment were understood by probing further. The band structure and density of states were studied carefully. However, there was no significant change in either band structure or density of states around 12 GPa. This confirmed the fact that TiB_2 does not exhibit any structural or electronic phase transition in the pressure range studied. After this, the charge density of TiB_2 were examined carefully in the pressure range of 0 to 22 GPa in step size of 2 GPa. The charge density distribution of TiB_2 along *(100)* plane of TiB_2 at 6, 10, 12 and 20 GPa are shown in figure 3.22. In the figure, the bonding between boron atoms and the charge distribution between them is presented. At 6 GPa, the charge distribution along the bond is encircled with a red circle and it can be seen that the charge accumulation is high near the boron atoms and is comparatively less between them.
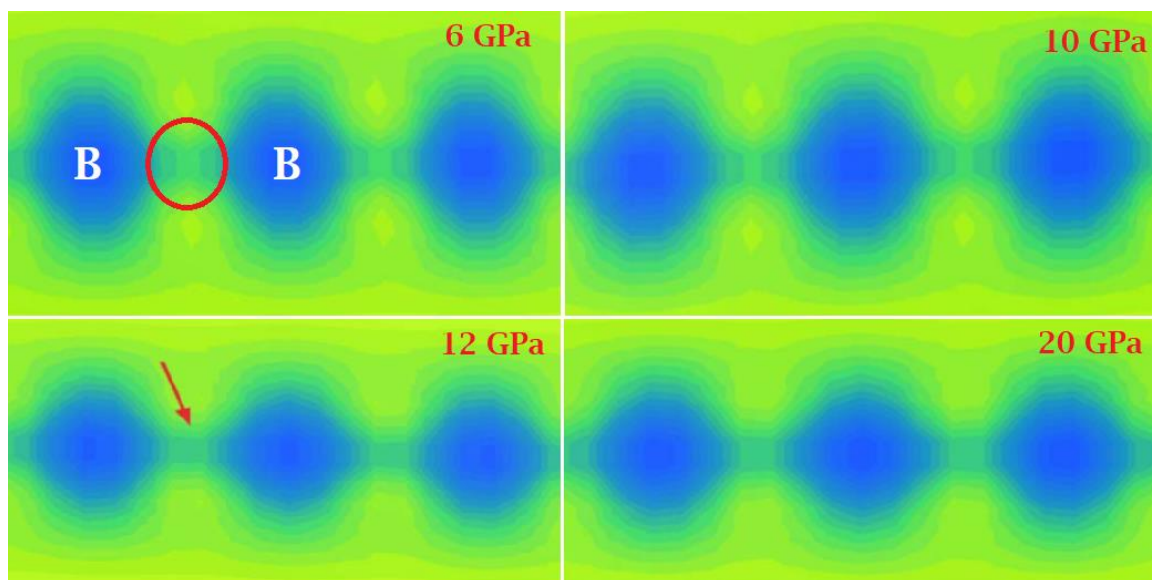
Figure 3.22:   Calculated charge density plots of TiB_2 along (100) direction. In the figure B-B covalent bond can be seen. Redistribution of charge density between the B-B atoms have led to the change in rate of bond compression.

With pressure, the charge density along the bond increases and interestingly a significant change is observed at 12 GPa where the distribution becomes high and uniform and is

indicated by a red arrow. With application of further pressure, the charge density becomes even higher. Hence, the change in B-B bond compression rate at 12 GPa can be attributed to this redistribution of charge. In TiB_2, the nature Ti-B bond is covalent with partial ionicity and the degree of covalency of Ti-B bond increases with pressure [187, 188]. Hence, it can be concluded that Ti-B bond hardening is due to increase in covalent nature of the bond character.

3.4. Summary

The compressibility of VB, TaB and TaB_2 has been studied. The estimated bulk modulus are 301(5) GPa, 366(17) GPa and 333(6) GPa, respectively. Also, the bulk modulus of TaB_2 which was present as minor fraction in TaB sample, was estimated to be 332(16) GPa. All the studied borides are highly incompressible and structurally stable in the pressure range studied. Presence of pseudogap is a common feature in all of them implying high stability for them. VB, TaB and TiB_2 are metallic in nature which was inferred from the finite DOS at fermi level.

The comparison between the group 5B monoborides VB and TaB revealed that, TaB, TaB_2 are less compressible as compared to VB and VB_2, respectively. The common notion of bulk modulus to increase with increasing boron content does not hold for TaB and TaB_2 and also has been seen in the case of other borides like chromium borides, tungsten borides etc. In both the cases, the TM-TM bonds are metallic, B-B bonds are covalent and TM-B bonds was seen to have both covalent and ionic nature. However, the B-B bond is stronger for TaB and also, the charge transfer from tantalum to boron is higher as compared to that between V and B. These two factors contribute to the higher incompressibility of TaB. The study of linear compressibility showed that the compression is anisotropic and is in accordance with the bond nature and the bond alignment in their unit cells.

In the case of TiB$_2$ there was a decrease in rate of bond compression (bond hardening) for both B-B and Ti-B bond around 12 GPa. The significant charge redistribution along B-B bond at around 12 GPa and the increase in covalency of Ti-B bond with pressure are understood to be the possible reason for the changes observed. The compressibility behaviour of TiB$_2$ was also anisotropic with c axis being more compressible as compared to a axis. The bulk modulus of TiB$_2$ is highest among the diborides of $3d$ elements and 4B transition elements. The bulk modulus of diborides were seen to follow the trend of cohesive energy.

Chapter 4

High pressure synthesis of novel manganese monocarbide: A potential hard material

4.1. Introduction

The formation mechanism and synthesis of TMCs have been reviewed in the section 1.3.2. Also, the role of high pressure in synthesis of TMCs has been discussed. It is observed that relative strength of TM-TM and TM-C bonds dictates the stability of a particular phase. The TM-C bonds, where the bonding states are completely filled and anti-bonding states are completely vacant, are the strongest [82]. Along the series of TMs, due to increased occupation of anti-bonding states, TM-C bond becomes weaker for the TM present in the latter part of the series and insertion of more carbon to the TM lattice becomes difficult. For this reason, an absence of stable carbon rich TMC phases can be noticed for those TMs [189]. However, in general, hardness can be improved by insertion of more carbon to a TM lattice wherein the TM has high valency. Manganese (Mn) has the highest possible valence number for $3d$ transition metals. In the binary phase diagram of Mn and C, the phases reported are $Mn_{23}C_6$, Mn_5C_2, Mn_7C_3 and Mn_3C [190]. The thermodynamic properties of Mn-C compounds have been assessed by Djurovic et al using CALPHAD (calculation of phases diagram) method and the results for MnC_x (x ranging from 0.26 to 1) shows that for MnC the enthalpy of formation is positive [190, 191]. Hence, formation of manganese carbide with higher carbon content (x $\geq$ 1) is unfavourable. Nevertheless, as discussed in section 1.3.2, it can be expected to be synthesized by high pressure method. The following subsections describe the HPHT synthesis of new novel manganese monocarbide using laser heated diamond anvil cell.

4.2. HPHT synthesis of novel manganese carbide

The HPHT synthesis of manganese carbide starting from elements was carried out using LHDAC facility [192]. Towards this, Mn (Cubic, $I\bar{4}3m$) and carbon powder were taken in the atomic ratio of 1:5 and mixed thoroughly by grinding with addition of alcohol. A pelletized sample of about 150 µm diameter along with ruby chip (pressure calibrant) was loaded in the sample chamber. Argon was loaded using in-house cryogenic loading system [193]. Argon functions both as pressure transmitting medium and also as insulation layer between sample and diamond anvils preventing graphitization of diamond at high temperature. The heating was done in rastering manner with laser power between 30-50% for 45 minutes at a pressure of 4.7 GPa and temperature was measured to be 2000 K. The experiment was repeated two more times to check for reproducibility wherein HPHT syntheses were carried out at 9.2 and 5.2 GPa respectively. After laser heating, the samples were retrieved to ambient condition and were characterized by XRD, TEM and micro-Raman spectroscopy.

4.2.1. X-ray diffraction

XRD was carried out in a Debye-Scherrer geometry using ULTRAX ($\lambda = 0.7107$ Å) and a mar-345 image plate detector. Due to mechanical constraint of the DAC, the data obtained was limited only up to $2\theta = 30°$. Hence, XRD on the retrieved sample was carried out only with the piston and meaningful data up to $2\theta = 40°$ could be obtained [98]. Figure 4.1 shows the ambient XRD patterns of the sample before and after laser heating at 4.7 GPa and 9.2 GPa. Along with the unreacted Mn Bragg peaks, the appearance of new reflections at 2θ positions 15.99°, 18.46°, 26.26°, 30.86° and 32.25° can be clearly seen which indicates the formation of a manganese carbide phase (Mn-C). In figure 4.2, the 2D diffractogram of Mn-C formed after laser heating at 4.7 GPa, is shown. The Mn and Mn-C

peaks are marked in the image. The thick bright lines are from SS gaskets. In figure. 4.1 it can be seen that the observed new reflections are reproducible in high pressure synthesis range of 4.7 GPa to 9.2 GPa.
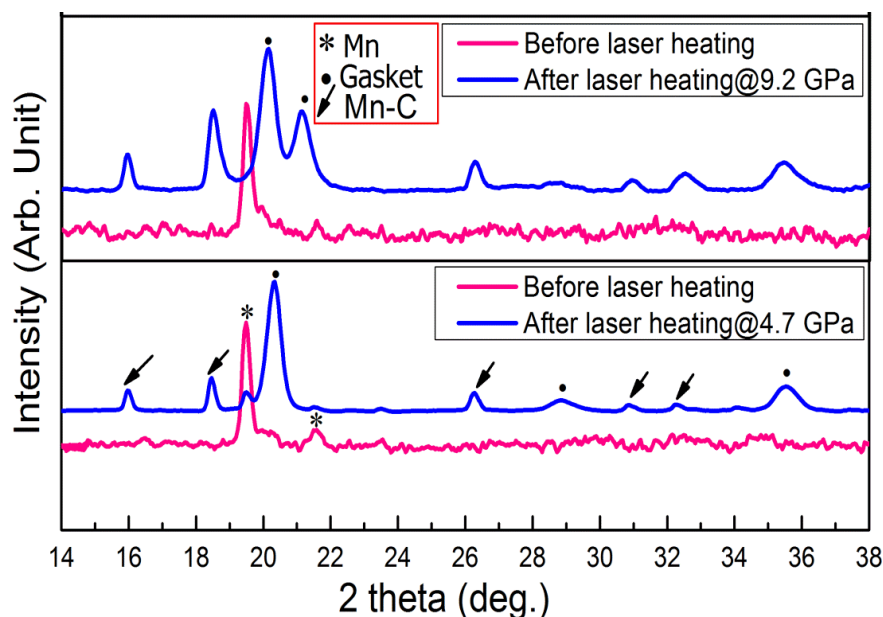
Figure 4.1: Ambient X-ray diffraction patterns of the sample before and after laser heating confirming the formation of manganese carbide phase and reproducibility of the result. The peaks for Mn-C are marked by arrow. The star marked peaks are from Mn and the dot marked peaks are from gasket
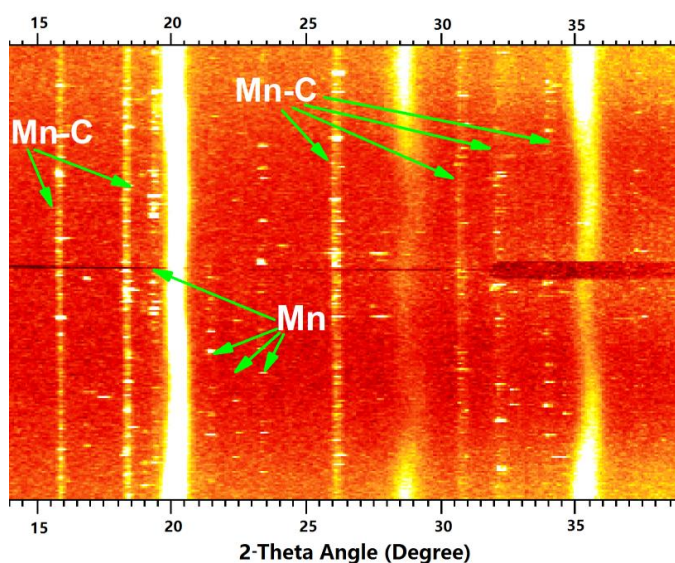
Figure 4.2: 2D diffractogram of Mn-C after laser heating at 4.7 GPa. The thick bright lines are from SS gasket.

As a first step towards phase determination, the XRD pattern of the retrieved sample was compared with the XRD patterns of the phases present in the binary phase diagram of Mn and C system viz. $Mn_{23}C_6$, Mn_3C, Mn_7C_3 and Mn_5C_2 [190, 194-197]. The comparison confirmed that new manganese carbide has formed.

4.2.2. Transmission Electron Microscopy study

Transmission electron microscopy (TEM) was carried out for further characterization of the sample, mainly with the aim of probing further d-spacing. As the sample volume obtained from the high pressure synthesis is of the order of microgram, the conventional sample preparation method for TEM was not possible. Hence, the retrieved sample was sheared between the diamond anvils to make it thin and thereby electron beam transparent. Then, the sample was transferred to the carbon coated copper grid. LIBRA 200 FE HRTEM was used for selected area electron diffraction (SAED) and imaging. The information limit of the microscope is 0.13 nm. Figure. 4.3 shows the bright field TEM image of the sample.
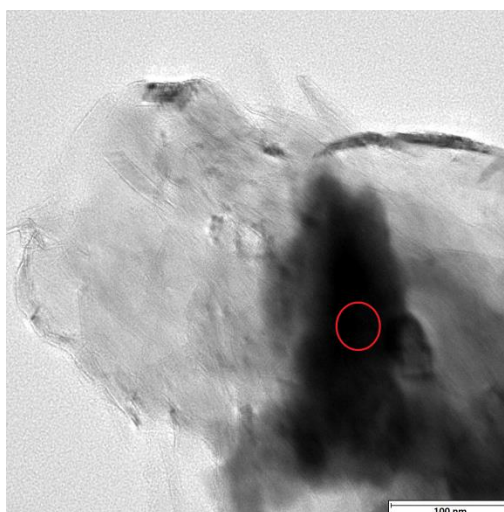
Figure 4.3: Bright field TEM image of the retrieved sample. The area where SAED was performed is marked with red circle. The lighter part is the image of graphene formed along with manganese carbide during laser heating.

The particles look agglomerated and some graphene like structure were seen in the image. Figure. 4.4 shows the SAED pattern of the sample. Some continuous rings and some bright dots forming rings can be seen in the diffraction pattern. The dotted rings are due to the small number of crystallites present in the sample.
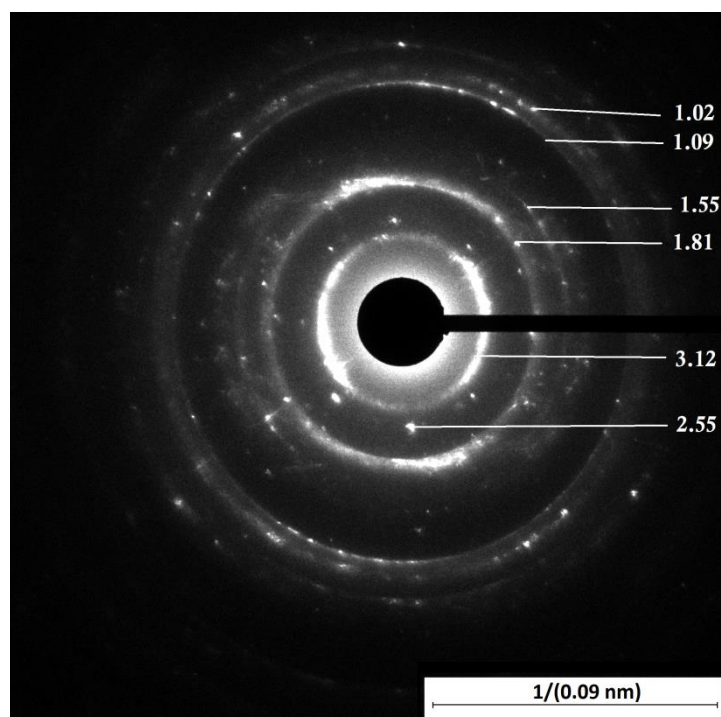
Figure 4.4: SAED pattern of the retrieved sample. The d-spacings in Å are marked corresponding to the rings.

The d-spacings were calculated corresponding to the rings and the same have been marked in the pattern. Table 4.1 lists the d-spacing obtained from SAED experiment along with those from ambient XRD of the retrieved sample. The d-spacings for Mn and C have been taken from ICDD PDF No. 00-032-0637 and 00-006-0675, respectively. It can be seen that the sample contains manganese and carbon along the manganese carbide. Also, few of the d-spacings obtained from XRD for the carbide are missing in the SAED pattern so is the case with Mn and C. This is because of the unconventional sample preparation method adopted. However, electron diffraction clearly corroborates the observation made in XRD.

Table 4.1:   List of d-spacings obtained from SAED experiment along with those from XRD experiment. The miller indices for Mn and C are mentioned in bracket. *ICDD PDF No. 00-032-0637 and #PDF No. 00-006-06755

From SAED	Mn*	C#	Mn-C from XRD	Remark
1.02	1.03 (831)	1.07 (311)		From Mn
1.09	1.09 (811)		1.10	From Mn-C mainly
	1.21 (721)	1.26 (220)	1.27	
			1.33	
1.51	1.52 (530)		1.56	From Mn-C mainly
	1.74 (510)			
1.81	1.81 (422)			From Mn only
1.96	1.89 (332)			From Mn only
	2.10(411)			
		2.06(111)		
			2.21	
2.55	2.57 (222)		2.55	From Mn-C mainly
3.12	3.15 (220)			From Mn only
	3.64 (211)			

4.2.3.   Micro-Raman Study

Micro-Raman study was carried out using Renishaw inVia Raman Spectroscope, UK with 514 nm laser excitation. The Raman spectra are shown in figure 4.5. The modes for graphene (also indicated in TEM imaging) could only be observed. In the spectra, the G (1583 cm^{-1}) and 2D band (2714 cm^{-1}) of graphene can be seen. The D band (1352 cm^{-1}) is caused by disordered structure of graphene. The intensity ratio of G and 2D bands suggest it to be a multilayer graphene.[198] However, no Raman active modes could be observed for the synthesized manganese carbide indicating that may be the novel phase is metallic in nature.
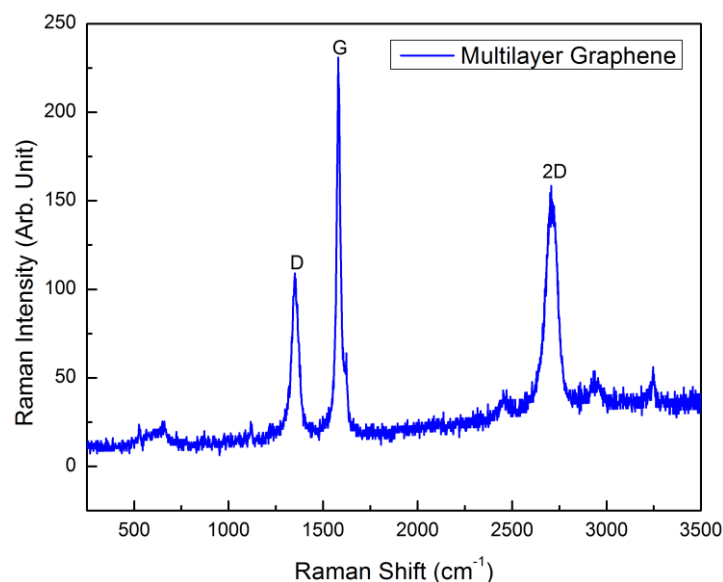
Figure 4.5: Raman spectra of the laser heated sample. The spectra show modes only for graphene and no modes for the manganese carbide could be observed.

4.3. Phase identification of the new manganese carbide

For crystal structure determination the XRD data was taken into consideration for POWD analysis. To get the plausible candidate structures for the LHDAC synthesized carbide, a survey on the structures adopted by TMCs were carried out. It was noticed that the TMCs adopt the stoichiometries M_3C_4, M_4C_3, M_3C_2, M_2C, M_5C_2 and MC, and in general, they adopt cubic or hexagonal close packed structures. Hence, the unit cell parameters were generated for cubic and hexagonal systems. XRD patterns were simulated with different crystal structures and the obtained lattice parameters. The best match to the experimental XRD pattern was obtained with four cubic crystal structures *viz.* Ag_2O, Nb_4C_3, NaCl (B1) and ZnS (B3) type crystal structures, and one hexagonal structure i.e. Al_3Ni_2 type. Thermodynamic stability of all the above candidate structures was studied using *ab initio* electronic structure calculations. The calculations were carried out employing density functional theory (DFT). PAW-PBE potential method as implemented in VASP code was used. $20 \times 20 \times 20$ k-points were considered for computation. Calculations using density functional perturbation theory (DFPT) have been carried out to calculate the phonon

dispersion using VASP plane wave code and PHONOPY module [199, 200]. The computationally obtained unit cell parameters and their comparison with the experimentally obtained parameter are discussed as follows. The experimentally obtained unit cell with Al_3Ni_2 structure type has $a = 4.4209(4)$ Å and $c = 3.4211(6)$ Å. In the unit cell, there are two types of Mn sites and those are *1a* (0, 0, 0), *2d* (0.333, 0.666, 0.621) and C is at 2d(0.333, 0.666, 0.119). However, the simulated XRD pattern of the computed unit cell with relaxed lattice parameters and atom positions does not reproduce the experimentally observed peak at 26.16° and also, the predicted Bragg peaks (002) and (1$\bar{2}$1) were not observed in the experimental pattern. Hence, the possibility of the synthesized Mn-C adopting the structure type of Al_3Ni_2 can be ruled out. The lattice parameter for the cubic lattice types obtained was 4.42(1) Å. In Table 4.2, the computed equilibrium lattice parameters for all the four cubic candidate structures are listed down. It can be seen that for the Ag_2O and Nb_4C_3 prototypes, computed lattice parameters are not in good agreement with the experimentally obtained lattice parameter value. Hence, those structure types can also be eliminated from further analysis. For B3 structure of manganese monocarbide (MnC), the experimental and computed lattice parameters are in good agreement whereas for the NaCl type they are not. Hence, it appears that B3 type MnC has formed.

Table 4.2:   Computed equilibrium lattice parameters for the cubic candidate structures for the synthesized Mn-C.

Candidate structure	Computed Lattice parameter (a in Å)
Mn$_2$C: Prototype: Ag$_2$O Space Group - $Pn\overline{3}m$ (224)	4.083
Mn$_4$C$_3$:Prototype: Nb$_4$C$_3$ Space Group - $Pm\overline{3}$ m (221)	3.932
MnC: Prototype: NaCl (B1) Space group - $Fm\overline{3}m$ (225)	4.005
MnC: Prototype - ZnS (B3) Space group - $F\overline{4}3m$ (216)	4.290

A study on *3d* transition metal monocarbides to understand the relation between average charge density per molecule (n_e) and the cohesive properties, shows that the cohesive energy is maximum for TiC ($n_e = 4$) and it decreases afterwards, reaches a minima for MnC ($n_e = 5.5$) and again increases for higher n_e. A complementary trend is seen for the density of states (DOS) wherein Fermi level lies in deep minima of DOS for TiC and moves up towards higher density (less stability) and DOS becomes maximum for MnC. Also, from extrapolation of experimental data and theoretical calculation it is seen that with increasing n_e the enthalpy of formation becomes unfavourable after VC [201, 202]. In the light of the above discussion, ScC, TiC and VC are designated as stable compounds and are reported to be synthesized by high temperature and mechanochemical methods [75-78]. Accordingly, CrC, MnC, FeC, CoC and NiC are designated as metastable compounds. However, among these metastable compounds, synthesis of CrC has been reported to be done by ion implantation and that of FeC by pulsed laser deposition. [203, 204]. It is interesting to note that both the stable and metastable *3d* TMCs are reported to adopt NaCl (B1) structure type. [203-207] Hence, in spite of the difference in lattice parameter, it becomes pertinent to investigate the dynamic stability of MnC in both B1 and B3 structure types. Figure 4.6 and 4.7 show the

phonon dispersion plots of MnC in NaCl and ZnS structure types at ambient. The appearance of negative modes in the dispersion plots for both B1 and B3 structures at ambient indicates that the structures are dynamically unstable. Nevertheless, as the synthesis has been done at HP-HT condition and has been quenched, to study the stability at high pressure and high temperature the phonon dispersion relation has been studied up to 10 GPa (unit cell compression *i.e.* high pressure) and -20 GPa (unit cell expansion *i.e.* high temperature). NaCl type MnC was found out to be dynamically unstable in the whole temperature and pressure range studied. However, ZnS type MnC becomes stable at -20 GPa (high temperature) and stays stable at further high temperatures. Figure 4.8 shows the phonon dispersion plots for MnC with ZnS type crystal structure at -20 GPa. The lattice parameter corresponding to the -20 GPa is $a = 4.436$ Å which is in good agreement with the experimental lattice parameter *i.e.* 4.4294 Å. Hence, it can be concluded that a high temperature phase of MnC has formed which crystallizes in ZnS crystal structure. To cite a parallel, it can be mentioned here that though the first paper on HPHT synthesis of PtC reported an NaCl type structure, later, the study by Qian Li *et al* has showed that ZnS type structure is the thermodynamically stable state for PtC.[99, 208]

Figure 4.9 shows the experimental and simulated XRD pattern for the HP-HT synthesized MnC plus Mn. The blank regions of 2θ in the XRD plot were excluded during Le Bail fitting due to presence of gasket peaks at those positions. In the unit cell of MnC, the Mn atom occupies the *4a (0, 0, 0)* position and C occupies the *4c* $\left(\frac{1}{4}, \frac{1}{4}, \frac{1}{4}\right)$ position and Mn is tetrahedrally bonded to C atoms. Figure 4.10 shows the extended unit cell of MnC representing the tetrahedral arrangement.
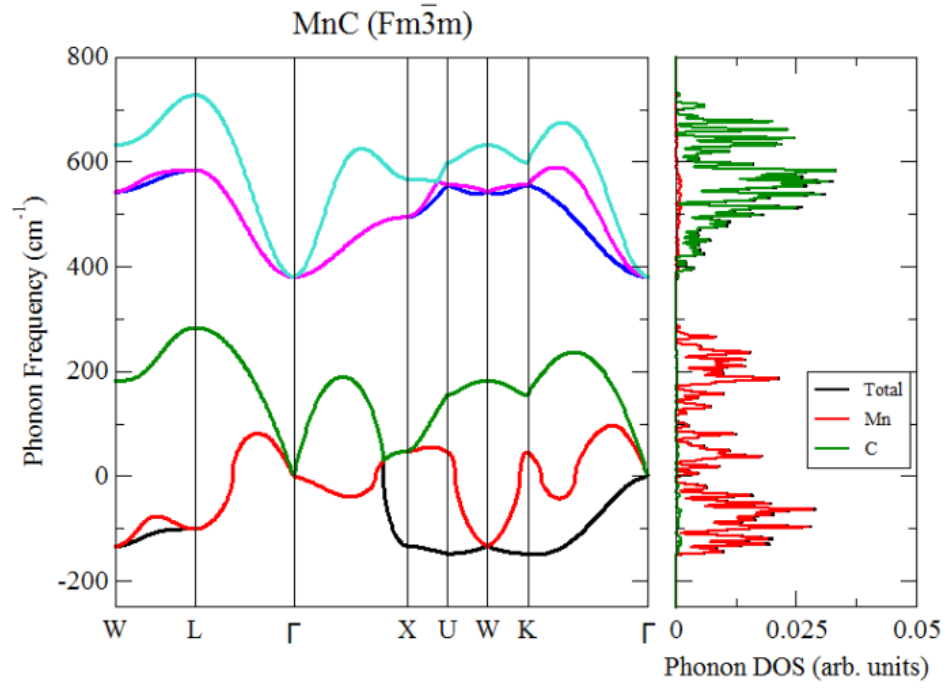
Figure 4.6: Phonon dispersion plot for MnC at ambient in B1 structure type. Appearance of negative modes infers dynamical instability of the structure.
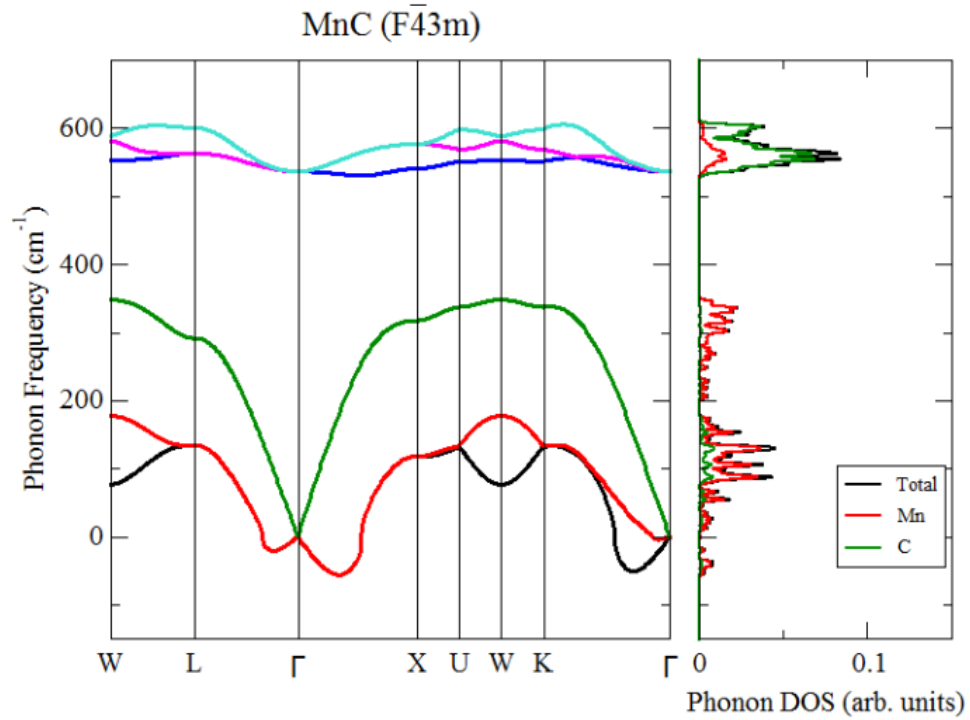
Figure 4.7: Phonon dispersion plot for MnC at ambient in B3 structure type. Appearance of negative modes infers dynamical instability of the structure
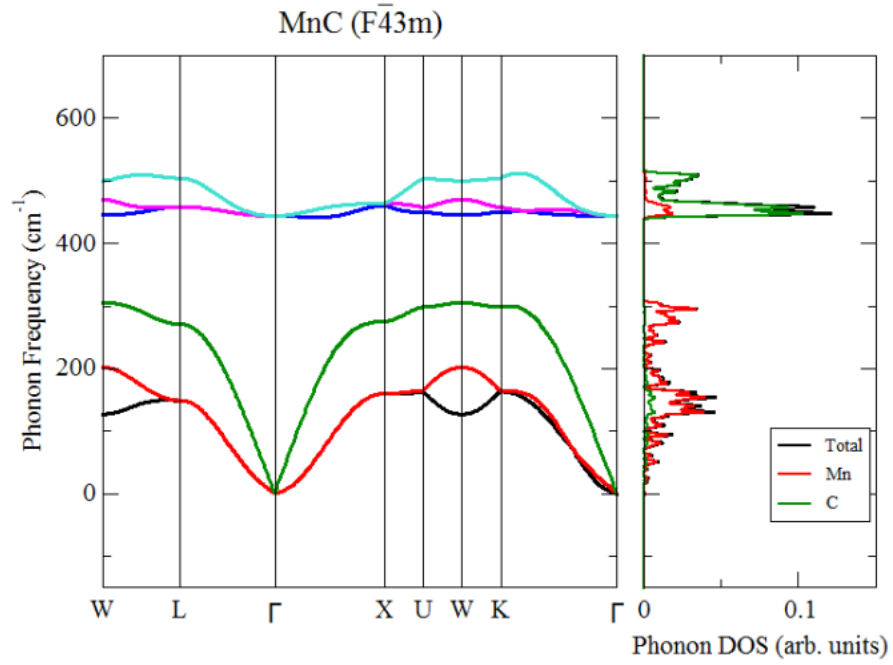
Figure 4.8: Phonon dispersion plot for MnC at -20 GPa in B3 structure type indicating dynamical stability of the structure at high temperature.
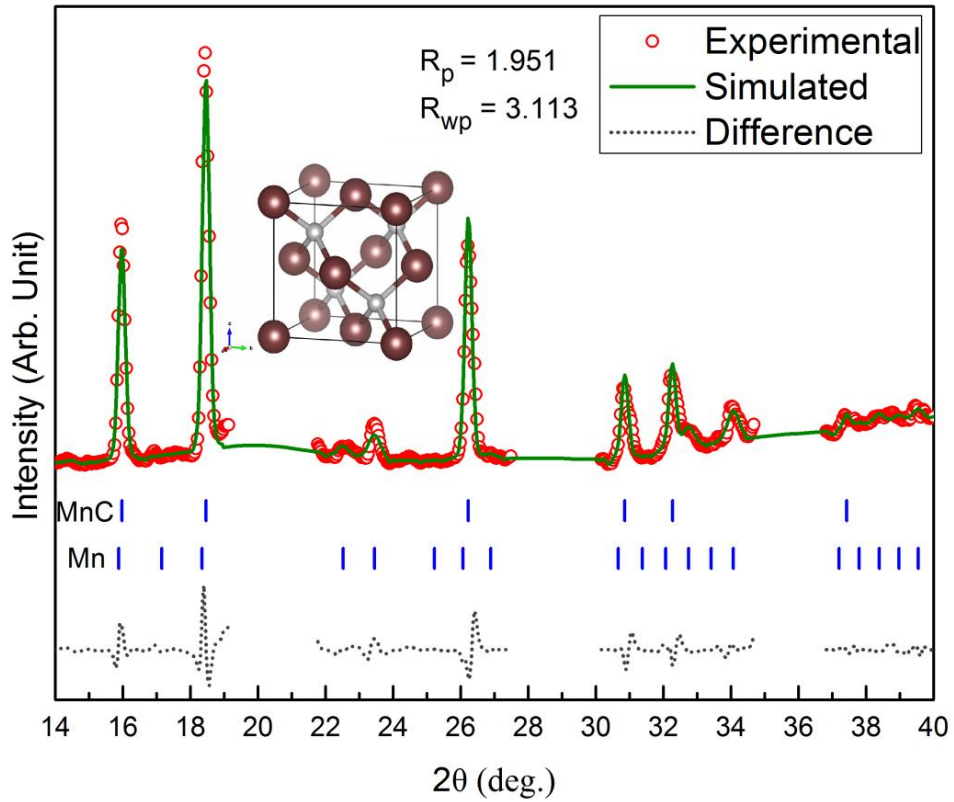
Figure 4.9: Le Bail fitting of the experimental XRD pattern with B3 type MnC and Mn structures. The inset shows the unit cell of MnC where Mn (the bigger sphere) is at 4a and C (smaller sphere) at 4c. The blank regions of 2θ in the XRD plot were excluded during fitting
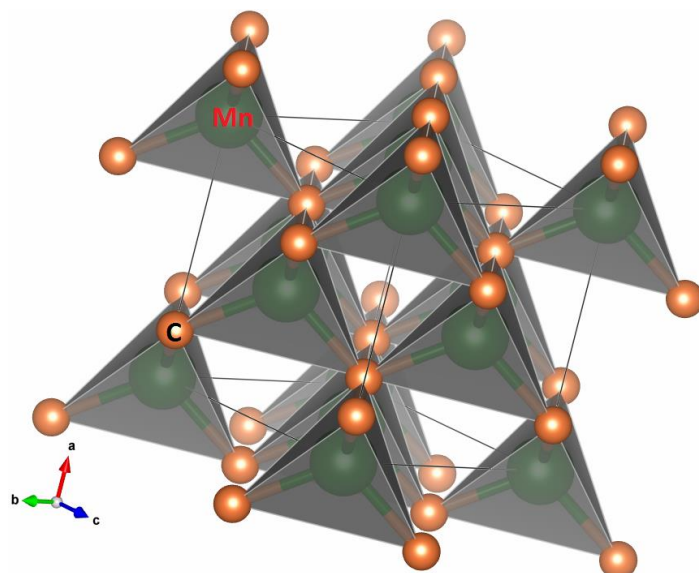
Figure 4.10:   Extended unit cell showing tetrahedral arrangement in MnC in ZnS structure.

4.4.   Estimation of bulk modulus of MnC

The bulk modulus of the synthesized MnC has been estimated by *in-situ* HPXRD experiments. Diffraction patterns were collected for 2 hours at each pressure during the experiment. Figure 4.11 (a) shows the HPXRD patterns of MnC. The MnC peaks are indexed in figure 4.11 (a). The peaks from Argon, Mn and gasket are also marked. For the lattice parameter determination at high pressure the *(111)* and 200 peaks were taken into consideration. The average of the volumes obtained from the two peaks has been plotted against pressure in figure 4.11 (b). By fitting the P-V data to second order Birch-Murnaghan equation of state (BM2 EOS) the bulk modulus (B_0) was found out to be 170(5) GPa.
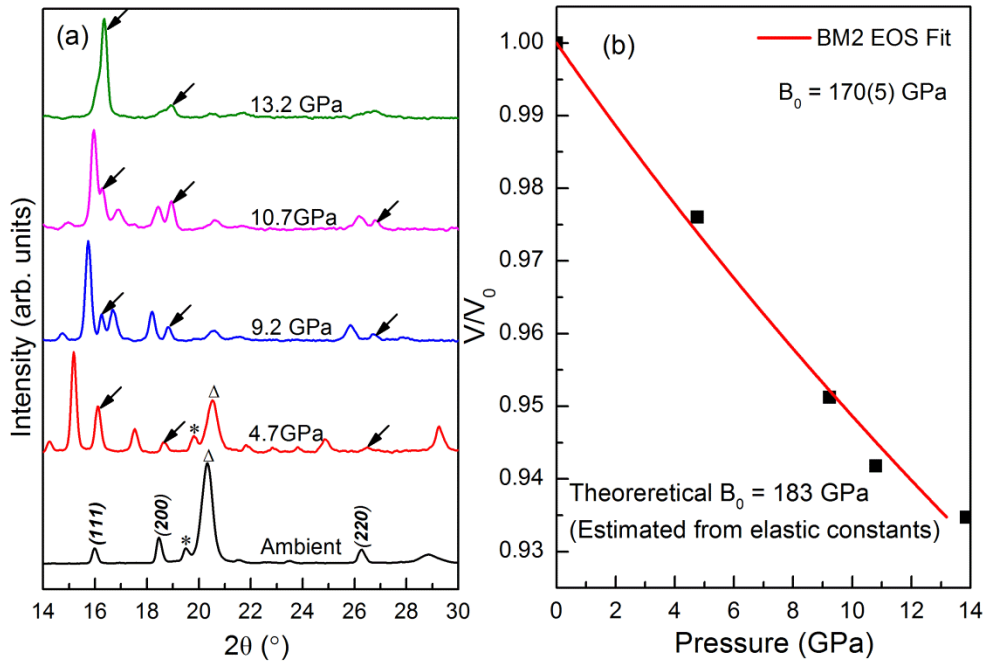
Figure 4.11: (a) HPXRD patterns of MnC. The MnC peaks are indexed in the ambient pattern and are marked with arrows at high pressures. The star marked peaks are from Mn, triangle marked peaks are from gasket and unmarked peaks are from Argon (b) EOS fit to P-V data

Elastic stiffness constants were estimated for the high temperature MnC phase by electronic structure calculation. For cubic structure three independent elastic constants *viz.* C_{11}, C_{12}, C_{44} are needed. For MnC, $C_{11} = 286.44$, $C_{12} = 235.27$ and $C_{44} = 127.17$. These estimated constants satisfy the Born Criterion showing elastic stability of the phase.[159] The bulk modulus was estimated to be 183 GPa by Voigt-Reuss-Hill average formula which is in good agreement with the experimental bulk modulus value.

4.5. Electronic structure of MnC

The electronic properties of MnC were investigated by *ab initio* electronic structure calculations. Figure 4.12 shows the band structure and electronic density of state plots for the high temperature MnC phase. The finite density of state at the Fermi level tells that MnC is metallic and the *d*-band of Mn is mainly contributing towards it. The metallic nature possibly could be the reason for not getting Raman active modes from micro-Raman experiment. Figure 4.13 shows the electronic charge density plot for MnC in the plane $1\bar{1}0$.

The colour from blue to red indicates low to high charge density. From the plot it can be seen that the charge density between Mn and C is high and contour maps show localization of charge between Mn and C; hence they are covalently bonded. The covalent nature of Mn-C bond can also be seen from the DOS vs. energy plot. The overlapping Mn d band and C p band in the interval ~-5 eV to -4 eV and -3eV to -2 eV indicate strong interaction between the *3d* and *2p* electrons of Mn and C. However, a partial iconicity of Mn-C bond can also be seen in figure 4.13. The high density charge cloud (orange colour) around carbon infers a charge transfer from Mn to C. The charge density between Mn and Mn is comparatively low and the distribution is uniform throughout, signifying metallic nature of Mn-Mn bond. Similar bonding nature is seen in TiC, VC, NbC, TaC and WC. [157, 209]

4.6. Empirical estimation of hardness

Hardness has been estimated from the crystal structure of MnC by using the empirical formula given by Antonín Šimůnek.[210] The formula estimates hardness reliably for various class of material (e.g. SiC, VC, WC) with a good correspondence to experimentally determined hardness value.[211] Hardness for a compound with two types of atoms is given as

$$H = \frac{C}{\Omega} b_{12} s_{12} e^{-\sigma f_2}$$

where, C and σ are empirically determined constants with values 1450 and 2.8, respectively. b_{12} is the number of bonds between atom 1 and atom 2 present in the unit cell. s_{12} is the strength of the bond between atom 1 and atom 2 which is defined as $s_{12} = \frac{\sqrt{e_1 e_2}}{n_1 n_2 d_{12}}$; where, $e_i = \frac{z_i}{R_i}$; z_i and R_i are the valence electron number and atomic radius of the atom i respectively and $f_2 = \left(\frac{e_1 - e_2}{e_1 + e_2}\right)^2$. n_1 and n_2 are coordination number of atom 1 and 2,

respectively. Mn shows various valency states out of which 4 and 7 are common. Hence, the corresponding hardness values were estimated.
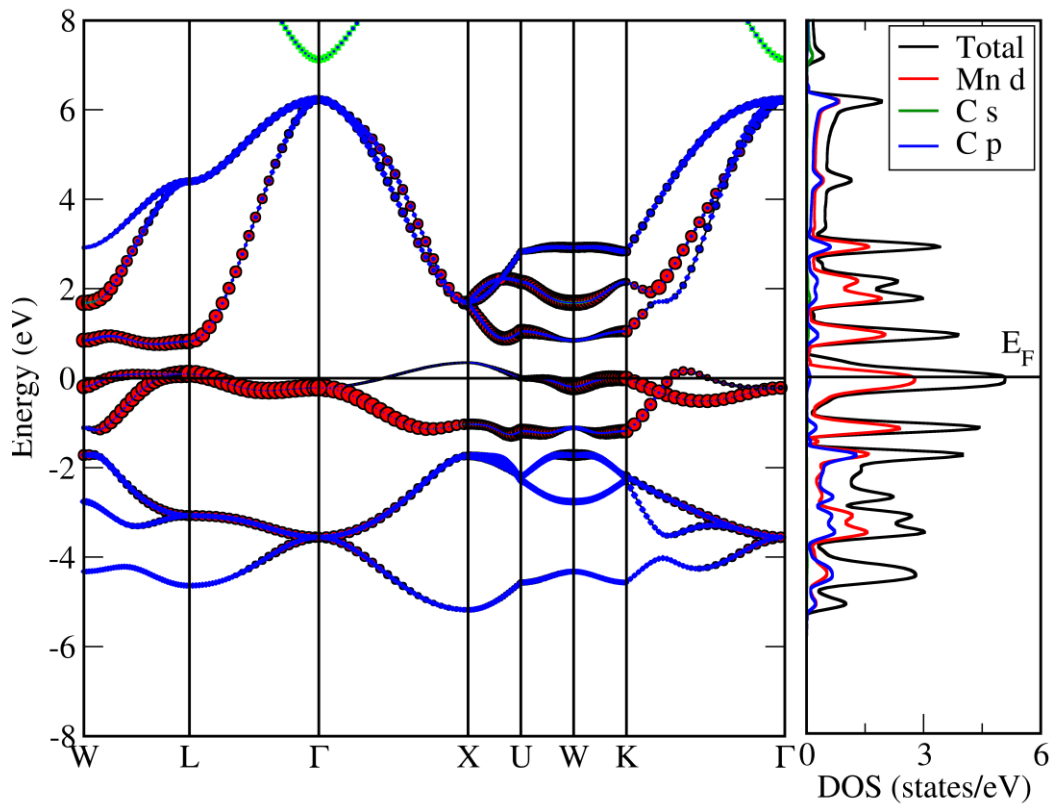
Figure 4.12:   Band structure and electronic density of state plot for MnC
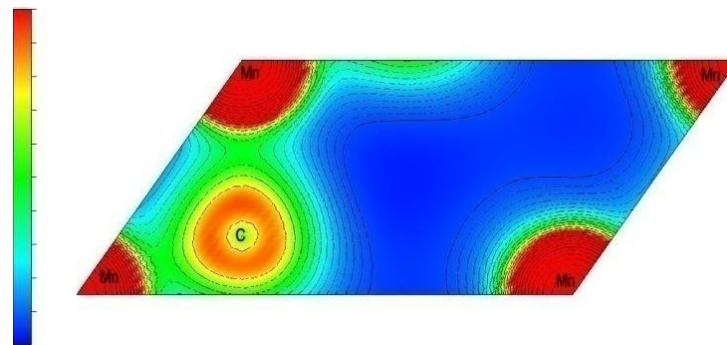
Figure 4.13: Electronic charge density plot for the 1̄1 0 plane of MnC

For MnC with ZnS structure, $b_{12} = 16$, R(Mn) = 1.26 Å, R (C) = 0.92 Å and $n_1 = n_2 = 4$ (can be seen in Figure 4.10), $d_{12} = 1.918$ Å. Thereby, H = 40.9 GPa with Z = 7 and H = 30.2 GPa with Z= 4.

To understand the high value estimated, it was compared with the hardness of TiC and VC wherein both of them adopt NaCl structure. For TiC, the Ti-C bond length is 2.162 Å (generated with PCW by crystal structure data from reference[212]) and the corresponding hardness is 16.4 GPa. Similarly for VC the bond length is 2.08 Å and the hardness is 25.4 GPa [207]. If the hardness of MnC is estimated in B1 type structure where the Mn-C bond length is 2.214 Å and the hardness value turns out to be 23.67 GPa with $Z = 7$. So, it can be inferred that the high value of hardness is endorsed by the high valence electron density of Mn, the short bond length (1.918 Å) and the tetrahedral arrangement in ZnS type MnC. From the above discussion, it can be asserted that MnC is a potential hard material which can be synthesized at a reasonably low pressure of 5 GPa. So, it can be synthesized in bulk by use of multi-anvil or belt type apparatus and can have huge industrial application like cubic boron nitride, tungsten carbide and silicon carbide.

4.7.   Summary and conclusion

MnC has been synthesized for the first time at HPHT condition by using LHDAC. MnC adopts ZnS type crystal structure *i.e.,* a cubic lattice with space group $F\overline{4}3m$ (216) and lattice parameter a = 4.4294(2) Å. The bulk modulus (B_0) and the pressure derivative of bulk modulus (B_0') have been found to be 170(5) GPa and 3.4 (1), respectively. The electronic properties as well as thermodynamic, dynamic and elastic stabilities have been investigated which shows that the obtained MnC phase is a high temperature phase. The theoretical results are in good agreement with the experimental results. The hardness has been estimated to be 40.9 GPa with valency $Z = 7$ and 30.1 GPa with $Z = 4$. This makes MnC a potential hard material which can be synthesized in bulk at a considerably low pressure of 5 GPa. The high hardness estimated is due to the tetrahedral bonding between Mn and C, the high valency of Mn and the short Mn-C bond length.

Chapter 5
High pressure synthesis of novel chromium carbide

5.1. Introduction

In the previous chapter, HPHT synthesis of a novel compound i.e. manganese monocarbide (MnC) was discussed and the empirical estimation of its hardness indicates a prospect that MnC is a material of high hardness. Chromium is the neighbouring element of manganese and has the highest possible valence number for *3d* transition metals. Also, this silvery white element is well known for its contribution towards hardness, toughness and corrosion/erosion resistance of stainless steel. In the chromium-carbon system, the common known phases are $Cr_{23}C_6$, Cr_7C_3 and Cr_3C_2 [213]. These chromium carbides are refractory ceramic compounds. Two metastable states namely Cr_2C and CrC are also reported in the Cr-C system [213, 214]. Cr_2C crystallizes in hexagonal structure and is known to increase fracture toughness of a material as well as has potential catalytic properties [215]. CrC is reported to crystallize in NaCl type structure. The unit cell parameters for CrC is reported to be in a range of 3.62 to 4.10 Å [216-218]. CrC in WC type (h-CrC) and in NaCl type structure (c-CrC) are studied computationally and it is revealed that h-CrC and c-CrC have considerably high hardness values (32.1 and 31.7 GPa respectively) as compared to that of Cr_7C_3, Cr_3C_2 and $Cr_{23}C_6$. As discussed earlier, a carbon rich phase may even show improved hardness. Hence, this study was aimed at synthesizing a novel superhard chromium carbide using HPHT synthesis method.

5.2. HPHT synthesis of chromium carbide and characterization

The HPHT synthesis was carried out using the CO_2 based LHDAC facility (described in section 2.2.2) from elemental chromium and graphitic carbon. Chromium to

carbon ratio was taken to be 1:5. They were mixed thoroughly by grinding and the mixture was pelletized using tungsten carbide anvils. A stainless steel gasket was pressed between the diamond anvils to a thickness of 80 µm and a hole of about 250 µm diameter was drilled in the pre-indented region. The pellet was loaded into the hole along with small ruby chips which worked as a pressure calibrant. Argon was loaded cryogenically using in-house Argon loading system [219]. The LHDAC experiments were carried out many times at pressure of about 5 GPa to confirm the reproducibility of the observed results. The sample retrieved to ambient condition was characterized by XRD and micro-Raman study.

5.2.1. X-ray diffraction study

X-ray diffraction experiment was carried out using ULTRAX with $\lambda = 0.7107$ Å in Debye Scherrer geometry. The 2 dimensional (2D) X-ray diffractogram of a typical retrieved sample after laser heating at 5 GPa is shown in figure 5.1.
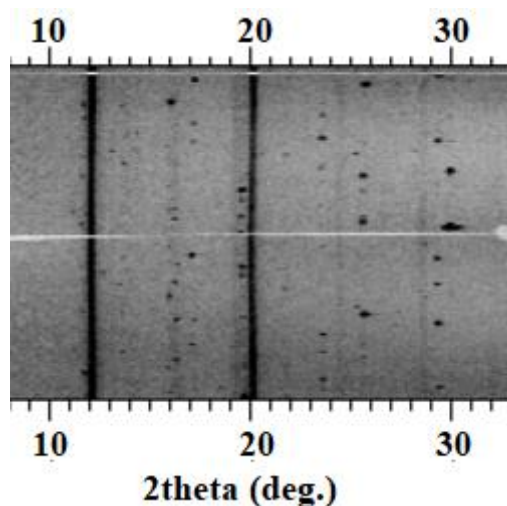
Figure 5.1:   2D diffractogram of the retrieved sample at ambient after laser heating at 5 GPa.

In the laser heating experiments, as the number of crystallites obtained is small, the XRD patterns look spotty. In the figure, the continuous lines belong to the unreacted starting elements i.e. chromium and graphite and, the dotted lines belong to the synthesized

chromium carbide. The ambient XRD patterns of the samples before and after heating are presented in figure 5.2. The appearance of new reflections at 2θ = 17.17°, 19.60°, 23.59°, 25.60° and 29.28° indicate the formation of a chromium carbide phase. The new reflections are marked by asterisks.
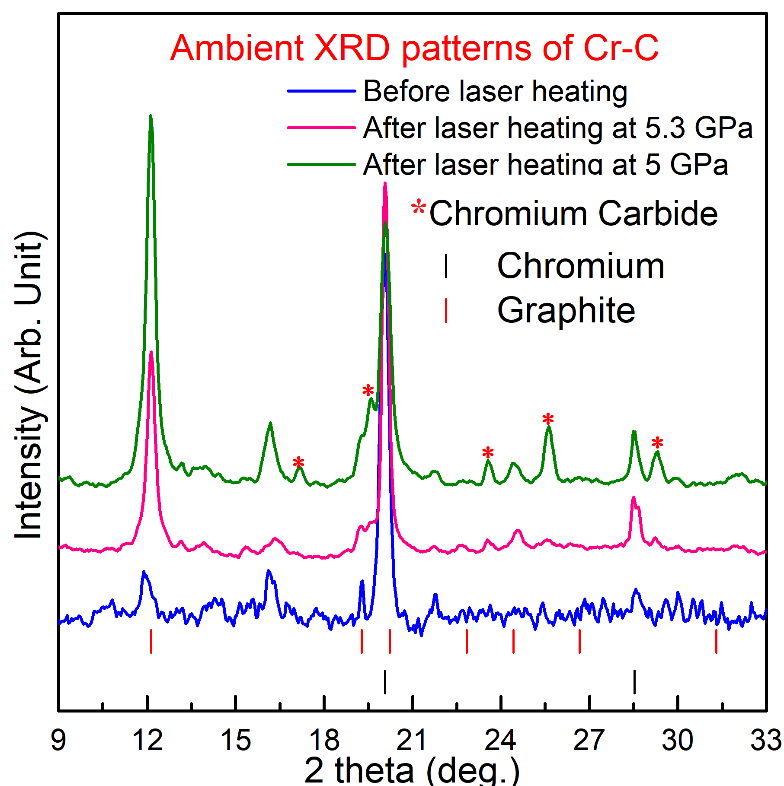
Figure 5.2: Ambient XRD patterns of Cr-C before and after laser heating at high pressure. The appearance of new peaks (marked with asterisk) confirms the formation of a chromium carbide.

5.2.2.   Raman Spectroscopy of the laser heated sample

Micro-Raman experiment was performed on the retrieved sample using Renishaw inVia Raman Spectroscope, UK with laser excitation of 514 nm. Two Raman modes were obtained at 1348 cm^{-1}(D band) and 1579.5 cm^{-1}(G Band) and were recognized to belong to nanographites [220]. Like in the case of manganese carbide, no modes for the chromium carbide could be observed. This indicates metallic nature of the carbide formed.

5.3. Phase identification of the synthesized carbide

First of all, the ambient XRD pattern of the retrieved sample was compared with the XRD patterns for reported phases of $Cr_{23}C_6$, Cr_7C_3 and Cr_3C_2 as well as the metastable phases Cr_2C and B1 type CrC. The pattern was also compared with that of the computationally studied WC type CrC. The comparison is depicted in figure 5.3. $Cr_{23}C_6$ does not index the reflections at 19.60°, 23.59° and 29.28°. The highest intensity peak of Cr_3C_2 is not experimentally observed and also, none of the experimentally observed peaks match with that of Cr_3C_2. From this it was recognized that the formed carbide is not any of the reported/predicted phases and a novel chromium carbide (Cr-C) has been obtained.
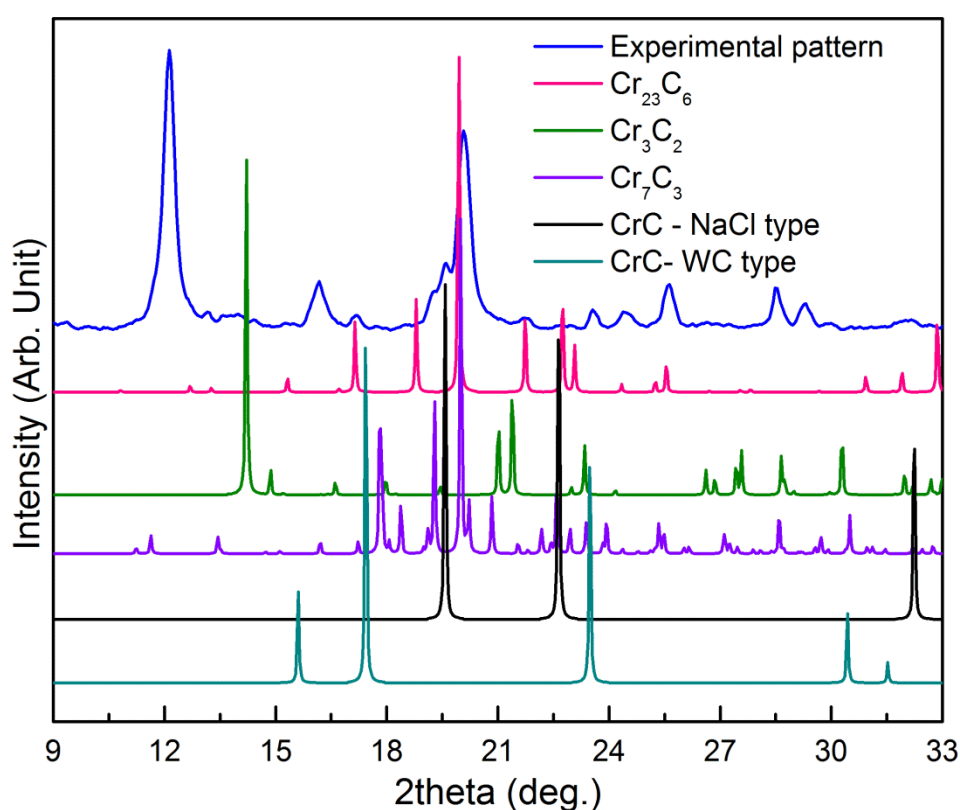
Figure 5.3: Comparison of the ambient XRD pattern of the synthesized chromium
carbide with that of phases reported earlier.

For the determination of the new phase, like in the case of manganese carbide, the XRD data was analyzed using POWD software [221]. Possible unit cell parameters were

generated for the observed reflections. No parameter belonging to cubic structure was predicted. Hence, possible hexagonal lattice parameters were generated. Two probable hexagonal unit cells were obtained with good figure of merit of 57.4 and 32.5 respectively. They are listed in table 5.1.

Table 5.1: Probable hexagonal unit cell parameters for the HPHT synthesized carbide

a in $\AA$	c in $\AA$	c/a	V in $\AA^3$
2.7475	8.6834	3.16	56.76
2.7496	17.4021	6.32	113.93

To determine the structure of the Cr-C formed, a survey on the structures adopted by transition metal carbides was carried out. Among the TM_3C type carbides, Fe_3C adopts hexagonal structure with space group $P6_322$ (182) with two formula unit in a cell (Z = 2). The c/a ratio of Fe_3C unit cell is 0.913 which is very different from that of the predicted Cr-C unit cell and the simulated XRD pattern with Fe_3C structure does not give a good match as well [222]. However, the predicted lattice parameters and c/a for the Cr-C has a good correspondence with Re_3N structure type (space group P-6m2, Z= 1) [223, 224]. Interestingly, XRD pattern for chromium carbide with prototype Re_3N i.e. Cr_3C showed a good matching with the experimental pattern.

TM_2C type carbides crystallize in hexagonal structure. Some of them, for example Nb_2C, Ru_2C and Ta_2C have the space group P-3m1 (164) and have one formula unit per unit cell [225-227]. Re_2C and Os_2C adopt Fe_2N type structure i.e. space group $P6_3/mmc$ (194) and have two formula units per unit cell [98, 228]. Study of Cr-C in these structure type showed that the synthesized carbide has not adopted any of them and hence, is not Cr_2C. The other stoichiometries of carbides *viz.* TM_4C_3, TM_3C_2, TM_6C_5 and TM_7C_3 type carbides were also

considered. However, the correspondence between experimental and simulated patterns was poor.

Some of the monocarbides like TiC, VC, FeC and MnC are reported to adopt cubic structures (NaCl or ZnS types) [204, 207, 212, 229]. Among the hexagonal monocarbides, RuC and OsC have been reported to crystallize in WC type structure [230]. Several $5d$ monocarbides are studied in WC structure using DFT [231]. The unit cells of these monocarbides have a volume of about 25 $Å^3$. However, for the HPHT synthesized carbide of present case, no unit cell with a volume of this order is predicted. Hence, the synthesized chromium carbide adopting WC structure is ruled out.

Another hexagonal monocarbide i.e. MoC was considered as the candidate structure. There are three polymorphs of hexagonal MoC besides the cubic one. γ MoC is WC type in structure [232]. γ' – MoC has space group $P6_3/mmc$ (194) and, unit cell parameters $a = 2.932$ Å, $c = 10.97$ Å and V = 81.67 $Å^3$ with Z= 4 [233]. The other polymorph is η-MoC which has 6 formula units in the unit cell and has a volume of 114.63 $Å^3$ [234]. A non-stoichiometry modification of η-MoC i.e $Mo_{1.2}C_{0.8}$ is also reported. In the unit cell, both Mo and C atoms share the *2a* and *4f* sites with site occupancy factors 0.2 and 0.8, respectively and the unit cell volume is higher [235]. It was noticed that η-MoC has similar unit cell parameters and c/a ratio as that of the predicted unit cell. When the experimental pattern was matched with the simulated XRD pattern with η-MoC structure (space group 194), it was observed that the predicted peak at 2θ = 17.17° is of very less intensity. Also, there is an additional high intense peak *(101)* at 2θ = 17.33° which is not present in the experimental pattern. Hence, the synthesized Cr-C adopting the space group 194 is ruled out. Modified MoC type structures with other symmetries were probed further as candidate structures.

The XRD pattern with hexagonal unit cell having space group P-6c2, $a = 2.7496$ Å, $c = 17.4021$ Å, wherein, the chromium atoms are at *2d* (0, 0, 0.25) and *4g* (0, 0, 0.7) and, C atoms are at *2a* (0, 0, 0) and *4i* (2/3, 1/3, 0.334), gave a good matching with the experimental pattern. Hence, Re_3N and modified MoC were considered as candidate structures for the synthesized chromium carbide. Thermodynamic, mechanical and dynamical stability of Cr-C in these two structures i.e. for Cr_3C and CrC, were studied using density functional theory.

5.3.1. Electronic structure calculations

Ab initio electronic structure calculations were carried out employing DFT. PAW−PBE potential method as implemented in VASP code was used. The calculations were carried out with energy cut-off 520 eV, and 4000 K-points in the whole Brillouin zone, that means 14x14x6 Gamma centered k-mesh for Cr_3C and 12x12x5 Gamma centred k-mesh for CrC structure, respectively. The k-points for charge density and DOS calculations were generated using a Gamma centered k-mesh 15x15x5 grid for both the structures using VASP. Both the structures were relaxed fully till the interatomic forces were less than 10^{-4} eV/atom. Starting from the experimentally found structure, the lattice parameters/volume was relaxed first, and then the atom positions were relaxed. This process was repeated three times in that order. After this the lattice parameters/volume and atom positions were relaxed in a simultaneous run so that the stress in the systems reduced to 0 kBar. After this the electronic structure, DOS were calculated.

5.3.1.1. Thermodynamic and mechanical stability of Cr_3C

The input for DFT calculation is tabulated in table 5.2. The structure was found to be thermodynamically stable and the computed equilibrium unit cell parameters are also listed in table 5.2. The elastic constants for Cr_3C were also calculated. There are 5

independent elastic constants for hexagonal structure. The elastic constants were calculated after giving 13 finite distortions for each of the 5 independent elastic constants (C_{11}, C_{33}, C_{44}, C_{12}, C_{13}), while $C_{66} = (C_{11}-C_{12})/2$. For Cr_3C, $C_{11} = 371.84$, $C_{12} = 265.42$, $C_{13} = 179.97$, $C_{33} = 566.23$, $C_{44} = 97.84$. For mechanical stability, the necessary and sufficient conditions are[159]

$$C_{11} > |C_{12}|$$

$$2C_{13}^2 < C_{33}(C_{11} + C_{12})$$

$$C_{44} > 0 \text{ and } C_{66} > 0$$

The above mentioned criteria are satisfied by the elastic constants of Cr_3C and hence, Cr_3C is mechanically stable. The bulk modulus (B) was estimated to be 284.51 GPa by Voigt approximation method.

Table 5.2: Experimental and computed equilibrium unit cell parameters for Cr_3C

For Cr_3C	
Experimental unit cell parameters as input	Computed equilibrium unit cell parameter
Space group No. 187 a = 2.7475 Å, c = 8.6834 Å	a = 2.6121 Å, c = 6.9272Å
Cr @ *1a* (0,0,0) Cr@ *2h*(1/3, 2/3, 0.802) C@ *1b*(0,0,1/2)	Cr1@(0,0,0) Cr2 @(1/3, 2/3, 0.309) Cr2 @(1/3, 2/3, 0.690) C@ (0,0,1/2)

5.3.1.2. **Thermodynamic and mechanical stability of CrC**

The experimentally obtained lattice parameters for CrC were $a = 2.7496$ Å, $c = 17.4021$ Å and the unit cell is presented in figure 5.4. It can be observed that if the unit cell

is cleaved along the *c*-axis at midway, the two parts look symmetrical. Hence, for the study of thermodynamic stability, the smaller unit with unchanged *a* = 2.7496 Å and halved along *c* axis i.e *c* = 8.7010 Å were considered as input for the computation. The structure of CrC which was taken as input for DFT study is listed in table 5.3. It can be noticed here that this unit cell is same as that of Cr_3C dimension wise.
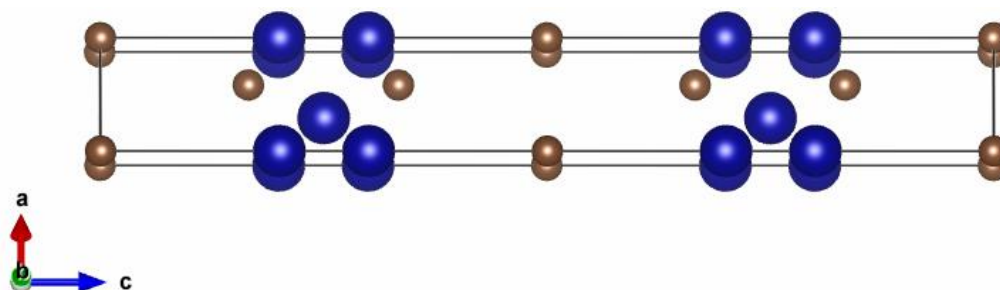
Figure 5.4: Proposed unit cell in modified MoC structure for the synthesized Cr-C

CrC was also found to be thermodynamically stable with equilibrium lattice parameters *a* = 2.9345 Å and *c* = 7.9205 Å.

Table 5.3: Experimental and computed equilibrium structural parameters for CrC

For CrC	
Structure of CrC taken as input	Computed equilibrium unit cell parameter
Space group No. 187 *a* = 2.7496 Å, *c* = 8.7010 Å	a = 2.93459 Å, c = 7.9205Å
Cr@ *1d*(1/3, 2/3, 0.5), Cr@ *2g*(0,0, 0.77), C@ *1a*(0,0,0), C@ *2i* (2/3, 1/3, 0.33)	Cr1@ (1/3,2/3, 0.5), Cr2 @ (0,0,0.228), Cr3@ (0,0,0.771), C1@(0,0,0) C2@ (2/3, 1/3, 0.652), C3 @ (2/3, 1/3, 0.347)

Elastic constants were estimated for CrC. They are $C_{11} = 373.11$, $C_{12} = 156.58$, $C_{13} = 182.78$, $C_{33} = 637.77$, $C_{44} = 112.22$ and $C_{66} = 108.31$. These elastic constants suggest that CrC is mechanically stable. The bulk modulus was calculated to be 269.83 GPa.

It can be noticed here that there is a difference in experimental and computational lattice parameters. The difference in lattice parameter has been reported for other high pressure synthesised systems *viz.* osmium carbide, ruthenium carbide, rhenium carbide etc. The major reason for this could be off stoichiometry which is a well-known phenomenon in refractory compounds. In the case of rhenium carbide effect of off stoichiometry on lattice parameter has been studied [236-238].

5.3.1.3.   Dynamical stability of Cr$_3$C and CrC.

For the calculation of phonon dispersions, density functional perturbation theory (DFPT) was used. For this, a 3x3x2 supercell was constructed which contained (3Cr+1C)x18 = 54 Cr + 18 C atoms in the case of Cr$_3$C and (3Cr+3C)x18 = 54 Cr + 54 C atoms in CrC structure. 9x9x5 Gamma centered k-grid was used for the supercell calculations. The atoms were displaced in both positive and negative directions for the force calculations. The output from VASP was analyzed with phonopy code. 15x15x5 q-points was used for plotting the phonon dispersion in the Brillouin zone for all the calculations.

The dynamical stability of the proposed structures for Cr$_3$C and CrC was studied. Figure 5.5 shows the phonon dispersion plot of Cr$_3$C. Presence of negative frequency indicates that the structure is not dynamically stable. Nevertheless, the structure for CrC was dynamically stable and the phonon dispersion plot is presented in figure 5.6.
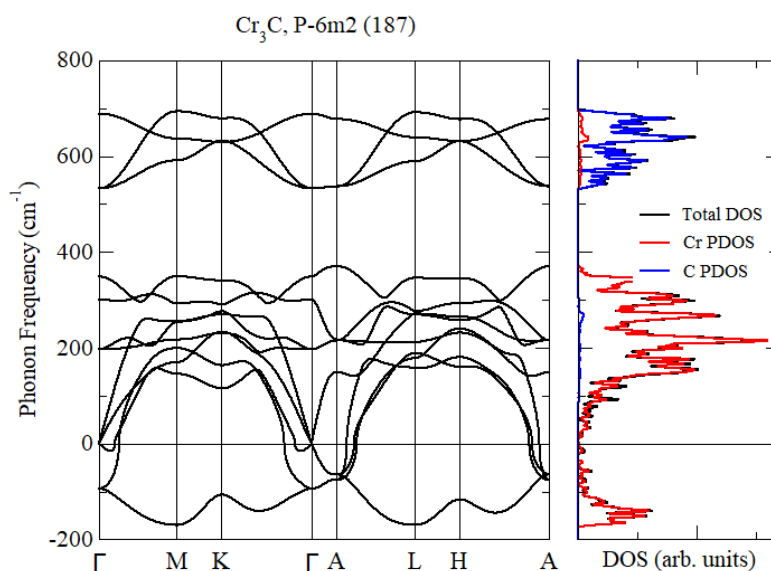
Figure 5.5:   Phonon dispersion plot for Cr$_3$C. Negative frequencies indicate dynamical instability
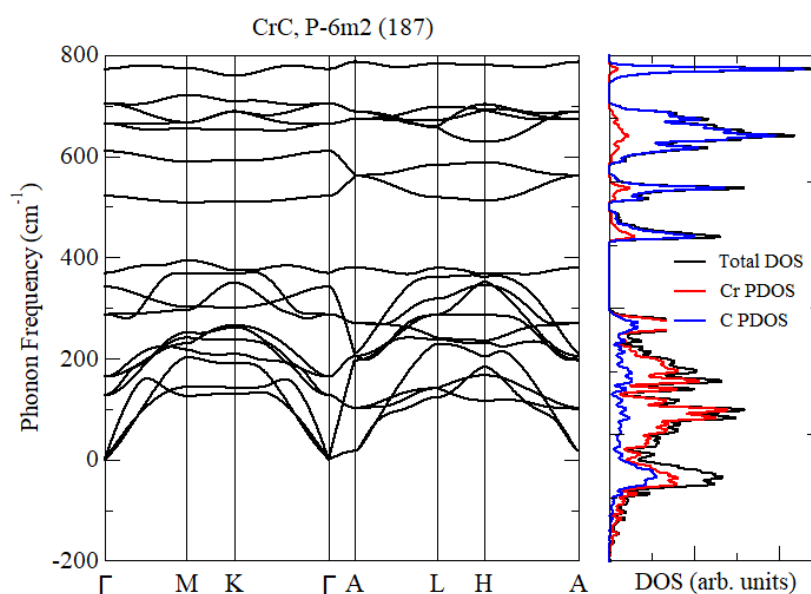
Figure 5.6:   Phonon dispersion plot of CrC. Absence of negative frequencies show dynamical instability

Hence, it can be concluded that chromium monocarbide (CrC) in a modified MoC structure has formed. The le-Bail fit of the experimental pattern with CrC, Cr and graphite structures is shown in figure 5.7. Further studies of the HPHT synthesized CrC was carried by density functional theory.
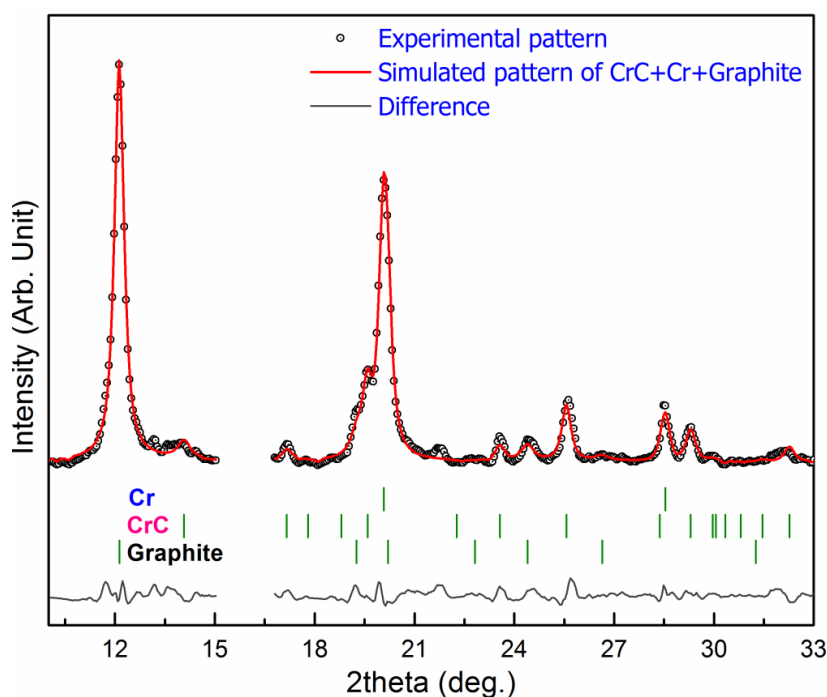
Figure 5.7:   Le Bail fit of experimental pattern with CrC, Cr and graphite. The blank
               region was excluded during fitting due to presence of unidentified peak

5.3.2.   Electronic Properties of CrC:

The electronic band structure and the density of states of CrC are shown in figure 5.8. In the band structure, the mixing of frequencies of Cr and C electrons (presented in red and green, respectively) infers *p-d* hybridization between them. The DOS at Fermi level is high indicating metallic nature of CrC. The electronic charge density distribution along the *(1-10)* plane of CrC is presented in figure 5.9. The light blue colour indicates highest charge density and the yellow colour indicates the lowest. Localization of charge between Cr and C, as well as transfer of charge from Cr to C, indicate that the bonding between Cr and C is a combination of covalent and ionic nature. Cr-Cr bond is metallic.
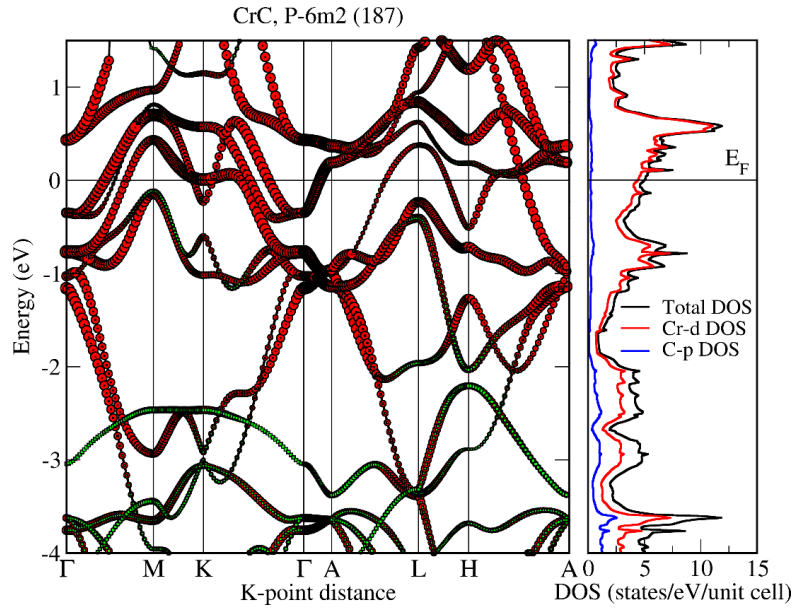
Figure 5.8: Electronic band structure of and density of state plot of CrC.
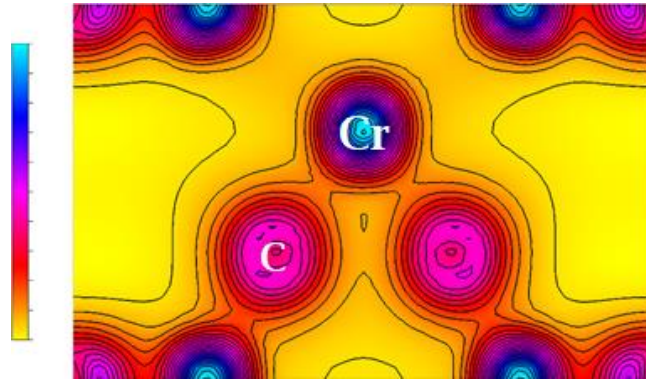
Figure 5.9: Charge density distribution of CrC in the (1-10) plane. Blue colour corresponds to highest charge density and yellow to the lowest.

5.3.3. Estimation of hardness:

The hardness of CrC was estimated by using the empirical formula suggested by Simunek. The formula uses the, bond strength, effictive charge of atoms involved and the no. of bonds present in the unitcell.

In the unit cell of CrC, there are two types of Cr. They are designated as Cr1 and Cr2. Similarly, there are two types of carbon atoms C1 and C2. The unit cell contains one Cr1, one C1, two Cr2 and two C2 atoms. Hence, the no. of formula units is 3. There are 5 different kinds of bonds involved and the formula for hardness reads.

$$H = \frac{C}{V} \times 5 \times [b_{12}s_{12}b_{34}s_{34}b_{56}s_{56}b_{78}s_{78}b_{910}s_{910}]^{1/5} \times e^{-\sigma f10}$$

where, b_{ij} is no. of bonds between the atoms i and j present in the unit cell, s_{ij} is the bond strength defined as $S_{ij} = \frac{e_i e_j}{n_i n_j d_{ij}}$; $e_i = \frac{Z_i}{R_i}$; n_i = coordination no. atom i; n_j = coordination no. atom j, d_{ij} = length of bond between i and j, z_i is the valence number and R_i is the atomic radius of atom i. $R(Cr) = 1.28$ Å and $R(C) = 0.92$ Å.

Contrary to MnC, CrC does not have isotropic bond length and strength. There are five types of bonds in the CrC unit cell.

i.   Bond between atom1 (Cr1) and atom2 (C2): As it can be seen in the figure 5.10 (a), Cr1 forms bonds with 6 C2 and the bond length d_{12} is 2.169 Å. Hence, b_{12} = 6, n_1 = 6. C2 has three Cr1, three Cr2 and 6 C2 neighbours (figure 5.5 a and c), that means n_2 = 12.
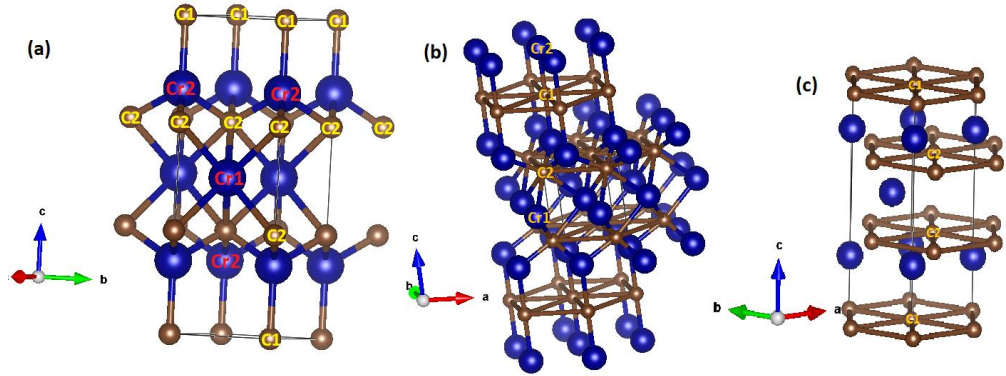
Figure 5.10:   Unit cell of CrC showing different types of bonding between the atoms.

ii.   Bond between atom3 (Cr2) and atom4 (C1): Both the Cr2 atoms form bond with one C1 atom each. In this case, b_{34} = 2, d_{34} = 2.001 Å, Cr2 has three C2 and one C1 as neighbours. Hence, n_3 = 4 and n_4 = 8 (figure 5.10 b)

iii.   Bond between atom5 (Cr2) and atom6 (C2): Cr2 is also bonded to three C2 atoms (figure 5.10 a). Hence, b_{56} = 6, n_5 = 4 and n_6 = 12. Here, d_{56} = 1.810 Å.

iv.   Bond between atom7 (C1) and atom8 (C1): In figure 5.10 c, it can be seen that the C1 atom has six similar C1 atoms as neighbours which are at a distance d_{78} = 2.749 Å. Here, b_{78} = 6, n_7 = n_8 = 6

v.   Bond between atom9 (C2) and atom10 (C2): Each of the two C2 atoms in the unit cell has six C2 atoms as neighbours in two parallel planes (figure 5.10 c) with bond length $d_{9,10}$ = 2.749 Å. So, $b_{9,10}$ = 12, n_9 = n10 = 6

In bond formation, the commonly adopted valence states of chromium are Z= 3 and 6. The hardness was estimated with both of them.

For Z (Cr) = 3 and Z (C) = 4 and with R(Cr) = 1.28 Å and R (C) = 0.92 Å.

e_{Cr} = 2.3437 and e_c = 4.3478

Hence, e_1 = e_3 = e_5 = 2.3437 and e_2 = e_4 = e_6 = e_7 = e_8 = e_9 = e_{10} = 4.3478

So, s_{12} = 0.0204, s_{34} = 0.0498, s_{56} = 0.0367, s_{78} =0.0439 and s_{910} = 0.0439

Now, f_{10} = 0.0704

So, hardness = 21.5 GPa

Now, the hardness of CrC with 6 as the valence state of Cr is calculated as follows.

With Z (Cr) = 6 and Z (C) = 4

e_1 = e_3 = e_5 = 4.6875 and e_2 = e_4 = e_6 = e_7 = e_8 = e_9 = e_{10} = 4.3478

hence, s_{12} = 0.0289, s_{34} = 0.0705, s_{56} = 0.0519, s_{78} =0.0439 and s_{910} = 0.0439

In this case, f_{10} = 0.0012 and hardness H = 32.2 GPa.

It can be seen that the estimated hardness of CrC, is lesser than that of ZnS type MnC and earlier reported NaCl type CrC. This may be because of the hexagonal structure

of CrC where where the carbon atoms form layers as seen in the case of graphite. Also, the coordination number which is inversely proportional to bond strength, is high and the C-C bond length is also considerably high.

5.4. Summary and conclusion

Chromium monocarbide has been synthesized at about 5 GPa using laser heated diamond anvil cell. With X-ray diffraction and stability studies using *ab initio* electronic structure calculation, the structure was determined to be hexagonal with space group P-6m2 (187) and lattice parameter $a = 2.7496(2)$ Å and $c = 8.7010(4)$ Å. The bulk modulus of CrC was estimated from 269.8 GPa compounds. Band structure and DOS study revealed that CrC is metallic and with *p-d* hybridization between chromium and carbon electrons. The study of charge density along (1-10) plane showed that the Cr-C bond has both ionic and covalent nature and, Cr-Cr bond is metallic. Empirical estimation of hardness showed that with valence number 6, the hardness of CrC is 32.2 GPa and that with valence number 3 is 21.5 GPa. CrC has a hardness lower than that of MnC which may be because of the graphite like carbon layer present in the structure.

Chapter 6

Summary and Future directions

6.1. Summary

The study presented in this thesis was aimed at investigating borides of group 4B and 5B transition metals as they have higher stability compared to other TMBs. The study also aimed at synthesizing carbon rich novel transition metal carbides which may show potential superhardness. With these objectives VB, TaB and TiB_2 were studied under high pressure and synthesis of novel manganese and chromium carbides were attempted using laser heated diamond anvil cell. VB was synthesized in single phase by arc melting followed by annealing the sample twice at 1000 °C for 4 days with intermittent grinding. TaB and TiB_2 were procured for the studies.

VB and TaB were studied using high pressure X-ray diffraction experiments and the DOS and charge density studies were carried out using density functional theory. The result of the studies is presented as follows. The orthorhombic lattices of the 5B monoborides VB and TaB were seen to be stable in the pressure range studied i.e. up to 37.5 GPa and 40.5 GPa, respectively. The respective estimated bulk modulus values are 301(5) and 366(17) GPa for VB and TaB. Study of bulk compressibility of TaB_2 which was present as a secondary phase estimated its bulk modulus to be 332(16) GPa. That means, TaB was more incompressible as compared to TaB_2 and there is no direct correlation between boron content and higher incompressibility. This has been the case in chromium, osmium and tungsten borides as well. The monoborides and diborides of tantalum (*5d* TM) were seen to be less compressible than those of vanadium (*3d* TM) respectively.

VB and TaB are metallic which was inferred from the finite DOS at their Fermi level. In both the cases, TM-TM bond is metallic, which is the reason of bulk metallicity. The B-B bond is covalent and the boron atoms form zig-zag boron chain along *c*-axis. TM-B bonds

have both covalent and ionic nature. The B-B covalent bond is stronger and the charge transfer from metal to boron is more in the case of TaB as compared to VB. These factors contribute to the higher incompressibility of TaB.

The studies on linear compressibility behaviour of VB and TaB showed that the compressibility is anisotropic in nature. In both the cases, the lattice was more compressible along the *a* – direction because of the predominant presence of metallic TM-TM bonds and the absence of covalent B-B bonds along the *a*-axis. The compressibility along *b* and *c* directions are of almost equal order with VB more compressible along the *b* direction and the opposite for TaB. The pseudogap at the Fermi level in DOS plot was understood to be due to ionicity of TM-B bond and *p-d* hybridization between TM *d* electrons and C *p* electrons.

The hexagonal lattice of TiB_2 was also seen to be stable in the pressure range studied and was highly incompressible with bulk modulus of 333(6) GPa. The compressibility was anisotropic in nature with *c*-axis more compressible as compared to *a*-axis. This is because of the presence of metallic bonds along *c* and covalent B-B bond along the *a* axis. Among the *3d* diborides, TiB_2 has the highest cohesive energy. It was seen that TiB_2 has the highest bulk modulus too. The study of correspondence between bulk modulus and cohesive energy revealed that experimentally estimated bulk modulus values of *3d* transition metal diborides follow the trend observed in cohesive energy. The diborides was also seen to follow the trend of cohesive energy along the group 4B.

A change in the rate of bond compression was seen for B-B and Ti-B bonds at about 12 GPa. The increase in charge density along the B-B bond at around 12 GPa and the increased covalency of Ti-B bond were understood to be the reason behind the change.

With the objective of synthesis of novel TMCs, a new manganese carbide i.e MnC was synthesized at high pressure and high temperature and was seen to reproducible in the

pressure range 4.7 to 9.2 GPa. The structure of MnC was found out to be ZnS type with lattice parameter 4.4294(2) Å and is metallic. The dynamical stability analysis reveals the synthesized phase to be high temperature phase. The bulk modulus was estimated to be 170(5) GPa. The hardness was estimated from its crystal structure by using an empirical relation. The estimated hardness values are 40.9 GPa with valency $Z = 7$ and 30.1 GPa with $Z = 4$. This makes MnC a potential hard material. The high hardness of MnC owes to high valency of Mn, tetrahedral bonding between Mn and C and the short Mn-C bond length. Another novel TMC i.e. chromium monocarbide has been synthesized at about 5 GPa. Unlike MnC, the synthesized CrC adopts a hexagonal lattice with space group 187 and lattice parameters $a = 2.7496(2)$ Å and $c = 8.7010(4)$ Å. The bulk modulus was estimated to be 269.8 GPa from its elastic constants using Voigt approximation method. Hence, CrC has considerably fair incompressibility. CrC is metallic with appreciable DOS at Fermi level which is because of the metallic nature of Cr-Cr bond. The Cr-C bond has both ionic and covalent nature. Similar to MnC, there is a *p-d* hybridization between Cr and C electrons. The hardness of CrC was empirically estimated to be 32.2 GPa for 6 as valence of Cr and 21.5 GPa for the valence 3. Hence, CrC has fair hardness. However, as compared to MnC it is less. This lower hardness is understood to be because of the graphite like carbon layers in the structure.

6.2. Future Directions

The compressibility behaviour of VB, TaB and TiB$_2$ has been studied under high pressure. These borides can be sintered for the improvement in mechanical properties and can be studied. TMBs are difficult to sinter due to low self-diffusion coefficient and strong covalent bindings. Nevertheless, sintering of TMBs can be done with suitable sintering aid using methods like spark plasma sintering, hot isostatic pressing and microwave sintering etc. [239-243].

Besides the rule of introducing covalent bonds by incorporation of light elements into TM lattice, another rule is to identify the weak slip plane and to strengthen the plane by the method of solid solutioning. With the application of this method, a series of ternary alloy $W_{1-x}Ta_xB$ have been studied and the alloy with x=0.5 has been found to be superhard with Vicker's hardness 42.8 GPa [244]. Ternary borides (Mo_2FeB_2 and Mo_2NiB_2) based cermets prepared by reaction boronizing sintering have improved mechanical properties [245]. Similarly other *3d* transition metals can be made to form ternary compounds with VB, TaB and TiB_2. Aluminium and aluminium-silicon based metal matrix composites (MMC) reinforced with TiB_2 have been seen to show improved wear resistance, hardness and machinability. They are used in aerospace and defense [246, 247]. Reinforcement of other borides with properties comparable to TiB_2 may yield good result. Boride composites like ZrB_2-TaB_2 has shown better strength as compared to individual boride. Hence, composite of VB and TaB can be prepared by spark plasma sintering and studied. With use of sintering aid like Fe, Ni and Al, mechanical properties of TiB_2 is seen to improve. Hence, this aspect can be investigated with VB and TaB.

The application of TMBs as energy storage device is an active area of research [37, 38]. Application of VB, TaB and TiB_2 as electrodes in battery can be investigated.

Both MnC and CrC have been synthesized at moderate pressure of 5 GPa and MnC is a potential hard material. As the novel phase has been obtained at few GPa both MnC and CrC can be synthesized in bulk by using belt type apparatus for proper characterization and investigation of other properties.

The HPHT synthesized chromium carbide has been identified to be chromium monocarbide with hexagonal lattice and the bulk modulus has been estimated from its elastic constants. The experimental and computational high pressure study of CrC can be carried out to probe high pressure structural stability of the novel phase obtained.

References

1.   Spear, K. E.; Dismukes, J. P., *Synthetic diamond: emerging CVD science and technology*. John Wiley & Sons: 1994; Vol. 25.

2.   Liang, Y.; Qin, P.; Jiang, H.; Zhang, L.; Zhang, J.; Tang, C., Designing superhard metals: The case of low borides. *AIP Advances* **2018,** *8* (4), 045305.

3.   Solozhenko, V. L.; Andrault, D.; Fiquet, G.; Mezouar, M.; Rubie, D. C., Synthesis of superhard cubic BC2N. *Applied Physics Letters* **2001,** *78* (10), 1385-1387.

4.   Liang, Y.; Zhong, Z.; Zhang, W., A thermodynamic criterion for designing superhard transition-metal borides with ultimate boron content. *Computational Materials Science* **2013,** *68*, 222-228.

5.   Matkovich, V. I.; Samsonov, G.-.; Hagenmuller, P., *Boron and refractory borides*. Springer: 1977.

6.   Kumar, P. A.; Satya, A. T.; Reddy, P. V. S.; Sekar, M.; Kanchana, V.; Vaitheeswaran, G.; Mani, A.; Kalavathi, S.; Shekar, N. V. C., Structural and low temperature transport properties of Fe2B and FeB systems at high pressure. *Journal of Physics and Chemistry of Solids* **2017,** *109*, 18-25.

7.   Sekar, M.; N. V, C. S.; Samudrala, A.; Shwetha, G.; Vaitheeswaran, G.; Venkatakrishnan, K., Structural stability of ultra-incompressible Mo2B: A combined experimental and theoretical study. *Journal of Alloys and Compounds* **2015,** *654*.

8.   Akopov, G.; Pangilinan, L. E.; Mohammadi, R.; Kaner, R. B., Perspective: Superhard metal borides: A look forward. *APL Materials* **2018,** *6* (7), 070901.

9.   Yeung, M. T.; Mohammadi, R.; Kaner, R. B., Ultraincompressible, Superhard Materials. *Annual Review of Materials Research* **2016,** *46* (1), 465-485.

10.   Winkler, B.; Juarez-Arellano, E. A.; Friedrich, A.; Bayarjargal, L.; Schröder, F.; Biehler, J.; Milman, V.; Clark, S. M.; Yan, J., In situ synchrotron X-ray diffraction study of the formation of TaB2 from the elements in a laser heated diamond anvil cell. *Solid State Sciences* **2010,** *12* (12), 2059-2064.

11.   Sologub, O.; Salamakha, L.; Rogl, P.; Stöger, B.; Bauer, E.; Bernardi, J.; Giester, G.; Waas, M.; Svagera, R., Pt–B System Revisited: Pt2B, a New Structure Type of Binary Borides. Ternary WAl12-Type Derivative Borides. *Inorganic Chemistry* **2015,** *54* (22), 10958-10965.

12.   *Cr₂B₃ Crystal Structure: Datasheet from "PAULING FILE Multinaries Edition – 2012" in SpringerMaterials (https://materials.springer.com/isp/crystallographic/docs/sd_0260412)*, Springer-Verlag Berlin Heidelberg & Material Phases Data System (MPDS), Switzerland & National Institute for Materials Science (NIMS), Japan.

13.   Wang, Y.; Chen, W.; Chen, X.; Liu, H. Y.; Ding, Z. H.; Ma, Y. M.; Wang, X. D.; Cao, Q. P.; Jiang, J. Z., Crystal structures, stability, electronic and elastic properties of 4d and

5d transition metal monoborides: First-principles calculations. *Journal of Alloys and Compounds* **2012,** *538*, 115-124.

14.   Gou, H.; Steinle-Neumann, G.; Bykova, E.; Nakajima, Y.; Miyajima, N.; Li, Y.; Ovsyannikov, S.; Dubrovinsky, L.; Dubrovinskaia, N., Stability of MnB2 with AlB2-type structure revealed by first-principles calculations and experiments. *Applied Physics Letters* **2013,** *102*.

15.   Aydin, S.; Simsek, M., First-principles calculations of ${\text{MnB}}_{2}$, ${\text{TcB}}_{2}$, and ${\text{ReB}}_{2}$ within the ${\text{ReB}}_{2}$-type structure. *Physical Review B* **2009,** *80* (13), 134107.

16.   Chung, H.-Y.; Weinberger, M. B.; Yang, J.-M.; Tolbert, S. H.; Kaner, R. B., Correlation between hardness and elastic moduli of the ultraincompressible transition metal diborides RuB2, OsB$_2$, and ReB$_2$. *Applied Physics Letters* **2008,** *92* (26), 261904.

17.   Gou, H.; Tsirlin, A. A.; Bykova, E.; Abakumov, A. M.; Van Tendeloo, G.; Richter, A.; Ovsyannikov, S. V.; Kurnosov, A. V.; Trots, D. M.; Konôpková, Z.; Liermann, H.-P.; Dubrovinsky, L.; Dubrovinskaia, N., Peierls distortion, magnetism, and high hardness of manganese tetraboride. *Physical Review B* **2014,** *89* (6), 064108.

18.   Wang, S.; Yu, X.; Zhang, J.; Zhang, Y.; Wang, L.; Leinenweber, K.; Xu, H.; Popov, D.; Park, C.; Yang, W.; He, D.; Zhao, Y., Crystal structures, elastic properties, and hardness of high-pressure synthesized CrB2 and CrB4. *Journal of Superhard Materials* **2014,** *36* (4), 279-287.

19.   Gou, H.; Dubrovinskaia, N.; Bykova, E.; Tsirlin, A. A.; Kasinathan, D.; Schnelle, W.; Richter, A.; Merlini, M.; Hanfland, M.; Abakumov, A. M.; Batuk, D.; Van Tendeloo, G.; Nakajima, Y.; Kolmogorov, A. N.; Dubrovinsky, L., Discovery of a Superhard Iron Tetraboride Superconductor. *Physical Review Letters* **2013,** *111* (15), 157002.

20.   Mohammadi, R.; Lech, A. T.; Xie, M.; Weaver, B. E.; Yeung, M. T.; Tolbert, S. H.; Kaner, R. B., Tungsten tetraboride, an inexpensive superhard material. *Proceedings of the National Academy of Sciences* **2011,** *108* (27), 10958.

21.   Fisk, Z., Superconducting borides. *AIP Conference Proceedings* **1991,** *231* (1), 155-164.

22.   Wang, Z.; Kochat, V.; Pandey, P.; Kashyap, S.; Chattopadhyay, S.; Samanta, A.; Sarkar, S.; Manimunda, P.; Zhang, X.; Asif, S.; Singh, A. K.; Chattopadhyay, K.; Tiwary, C. S.; Ajayan, P. M., Metal Immiscibility Route to Synthesis of Ultrathin Carbides, Borides, and Nitrides. *Advanced Materials* **2017,** *29* (29), 1700364.

23.   Heping, L.; Ming, X.; Chu, P. K.; Wang, J.; Sun, B. In *Microstructure and mechanical characterization of HVOF sprayed boride-based cermet coatings*, 2008 IEEE 35th International Conference on Plasma Science, 15-19 June 2008; 2008; pp 1-1.

24.   Wu, S. J.; Li, H.; Wu, S. Y.; Guo, Q.; Guo, B., Preparation of titanium carbide–titanium boride coatings on Ti6Al4V by PIRAC. *Surface Engineering* **2014,** *30* (9), 693-696.

25.   Timur, S.; Kartal, G.; Eryilmaz, O. L.; Erdemir, A., Ultra-fast boriding of metal surfaces for improved properties. Google Patents: 2015.

26.   Scales, S. R., Wear resistant boronized surfaces and boronizing methods. Google Patents: 1975.

27.   Medvedovski, E.; Jiang, J.; Robertson, M., Boride-based coatings for protection of cast iron against wear. *Advances in Applied Ceramics* **2016,** *115* (8), 483-494.

28.   Sen, U.; Abakay, E.; Sen, S., Characterization of Tungsten boride coating realized on AISI D2 steel.

29.   Doñu Ruiz, M. A.; López Perrusquia, N.; Sánchez Huerta, D.; Torres San Miguel, C. R.; Urriolagoitia Calderón, G. M.; Cerillo Moreno, E. A.; Cortes Suarez, J. V., Growth kinetics of boride coatings formed at the surface AISI M2 during dehydrated paste pack boriding. *Thin Solid Films* **2015**, 147-154.

30.   Sivakumar, B.; Singh, R.; Pathak, L. C., Corrosion behavior of titanium boride composite coating fabricated on commercially pure titanium in Ringer's solution for bioimplant applications. *Materials Science and Engineering: C* **2015,** *48*, 243-255.

31.   Johnston, J. M.; Catledge, S. A., Metal-boride phase formation on tungsten carbide (WC-Co) during microwave plasma chemical vapor deposition. *Applied Surface Science* **2016,** *364*, 315-321.

32.   Deboer, S. J.; Al-Shareef, H. N., Fabrication of semiconductor devices with transition metal boride films as diffusion barriers. Google Patents: 2005.

33.   Xu, S.-G.; Zhao, Y.-J.; Yang, X.-B.; Xu, H., Stable sandwich structures of two-dimensional iron borides FeBx alloy: a first-principles calculation. *RSC Advances* **2017,** *7* (48), 30320-30326.

34.   Subramanian, C.; Murthy, T. S. R. C.; Suri, A. K., Synthesis and consolidation of titanium diboride. *International Journal of Refractory Metals and Hard Materials* **2007,** *25* (4), 345-350.

35.   Kumashiro, Y., *Electric Refractory Materials*. Taylor & Francis: 2000.

36.   Amendola, S., High energy density boride batteries. Google Patents: 1999.

37.   Yu, X.; Licht, S., A novel high capacity, environmentally benign energy storage system: Super-iron boride battery. *Journal of Power Sources* **2008,** *179* (1), 407-411.

38.   Licht, S.; Wu, H.; Yu, X.; Wang, Y., Renewable highest capacity VB2/air energy storage. *Chemical Communications* **2008,** (28), 3257-3259.

39.   Licht, S.; Cui, B.; Stuart, J.; Wang, B.; Lau, J., Molten air – a new, highest energy class of rechargeable batteries. *Energy & Environmental Science* **2013,** *6* (12), 3646-3657.

40.   Wang, Y.; Guang, X. Y.; Cao, Y. L.; Ai, X. P.; Yang, H. X., Mechanochemical synthesis and electrochemical characterization of VBx as high capacity anode materials for air batteries. *Journal of Alloys and Compounds* **2010,** *501* (1), L12-L14.

41.   Kolmogorov, A. N.; Shah, S.; Margine, E. R.; Bialon, A. F.; Hammerschmidt, T.; Drautz, R., New Superconducting and Semiconducting Fe-B Compounds Predicted with an Ab Initio Evolutionary Search. *Physical Review Letters* **2010,** *105* (21), 217003.

42.   Levine, J. B.; Tolbert, S. H.; Kaner, R. B., Advancements in the Search for Superhard Ultra-Incompressible Metal Borides. *Advanced Functional Materials* **2009,** *19* (22), 3519-3533.

43.   Hebbache, M.; Stuparević, L.; Živković, D., A new superhard material: Osmium diboride OsB2. *Solid State Communications* **2006,** *139* (5), 227-231.

44.   Chung, H.-Y.; Weinberger, M. B.; Levine, J. B.; Kavner, A.; Yang, J.-M.; Tolbert, S. H.; Kaner, R. B., Synthesis of Ultra-Incompressible Superhard Rhenium Diboride at Ambient Pressure. *Science* **2007,** *316* (5823), 436.

45.   Latini, A.; Rau, J. V.; Teghil, R.; Generosi, A.; Albertini, V. R., Superhard Properties of Rhodium and Iridium Boride Films. *ACS Applied Materials & Interfaces* **2010,** *2* (2), 581-587.

46.   Niu, H.; Wang, J.; Chen, X.-Q.; Li, D.; Li, Y.; Lazar, P.; Podloucky, R.; N. Kolmogorov, A., Structure, bonding, and hardness of CrB$_4$: a superhard material? **2012**.

47.   Gu, Q.; Krauss, G.; Steurer, W., Transition Metal Borides: Superhard versus Ultra-incompressible. *Advanced Materials* **2008,** *20* (19), 3620-3626.

48.   Knappschneider, A.; Litterscheid, C.; Dzivenko, D.; Kurzman, J. A.; Seshadri, R.; Wagner, N.; Beck, J.; Riedel, R.; Albert, B., Possible Superhardness of CrB4. *Inorganic Chemistry* **2013,** *52* (2), 540-542.

49.   Zhong, M.-M.; Huang, C.; Tian, C.-L., The structural stabilities, mechanical properties and hardness of chromium tetraboride: Compared with low-B borides. *International Journal of Modern Physics B* **2016,** *30* (30), 1650201.

50.   Waśkowska, A.; Gerward, L.; Staun Olsen, J.; Ramesh Babu, K.; Vaitheeswaran, G.; Kanchana, V.; Svane, A.; Filipov, V. B.; Levchenko, G.; Lyaschenko, A., Thermoelastic properties of ScB2, TiB2, YB4 and HoB4: Experimental and theoretical studies. *Acta Materialia* **2011,** *59* (12), 4886-4894.

51.   Pereira, A. S.; Perottoni, C. A.; Jornada, J. A. H. d.; L ger, J. M.; Haines, J., Compressibility of AlB2-type transition metal diborides. *Journal of Physics: Condensed Matter* **2002,** *14* (44), 10615-10618.

52.   Halevy, I.; Beck, A.; Yaar, I.; Kahane, S.; Levy, O.; Auster, E.; Ettedgui, H.; Caspi, E. N.; Rivin, O.; Berant, Z., XRD, TDPAC and LAPW study of Hf 10 B 2 under high pressure. *Hyperfine Interactions* **2007,** *177* (1-3), 57-64.

53.   Liu, P.; Peng, F.; Yin, S.; Liu, F.; Wang, Q.; Zhu, X.; Wang, P.; Liu, J.; He, D., Exploring the behavior of molybdenum diboride (MoB2): A high pressure x-ray diffraction study. *Journal of Applied Physics* **2014,** *115* (16), 163502.

54.   Amulele, G. M.; Manghnani, M. H., Compression studies of TiB2 using synchrotron x-ray diffraction and ultrasonic techniques. *Journal of Applied Physics* **2004,** *97* (2), 023506.

55.   N. V, C. S.; Sekar, M.; Sahu, P. C., Equation of state and compressibility of nickel semiboride. *Physica B: Condensed Matter* **2014,** *443*, 95–98.

56.   Han, L.; Wang, S.; Zhu, J.; Han, S.; Li, W.; Chen, B.; Wang, X.; Yu, X.; Liu, B.; Zhang, R.; Long, Y.; Cheng, J.; Zhang, J.; Zhao, Y.; Jin, C., Hardness, elastic, and electronic properties of chromium monoboride. *Applied Physics Letters* **2015,** *106* (22), 221902.

57.   Fan, C.; Liu, C.; Peng, F.; Tan, N.; Tang, M.; Zhang, Q.; Wang, Q.; Li, F.; Wang, J.; Chen, Y.; Liang, H.; Guan, S.; Yang, K.; Liu, J., Phase stability and incompressibility of tungsten boride (WB) researched by in-situ high pressure x-ray diffraction. *Physica B: Condensed Matter* **2017,** *521*, 6-12.

58.   Wu, L.; Wan, B.; Zhao, Y.; Zhang, Y.; Liu, H.; Wang, Y.; Zhang, J.; Gou, H., Unraveling Stable Vanadium Tetraboride and Triboride by First-Principles Computations. *The Journal of Physical Chemistry C* **2015,** *119* (37), 21649-21657.

59.   Zhang, M.; Yan, H.; Wei, Q.; Wang, H., Pressure-induced phase transition and mechanical properties of molybdenum diboride: First principles calculations. *Journal of Applied Physics* **2012,** *112* (1), 013522.

60.   Zhang, M.; Wang, H.; Wang, H.; Zhang, X.; Iitaka, T.; Ma, Y., First-Principles Prediction on the High-Pressure Structures of Transition Metal Diborides (TMB2, TM = Sc, Ti, Y, Zr). *Inorganic Chemistry* **2010,** *49* (15), 6859-6864.

61.   Kotmool, K.; Kaewmaraya, T.; Chakraborty, S.; Anversa, J.; Bovornratanaraks, T.; Luo, W.; Gou, H.; Piquini, P. C.; Kang, T. W.; Mao, H.-k.; Ahuja, R., Revealing an unusual transparent phase of superhard iron tetraboride under high pressure. *Proceedings of the National Academy of Sciences* **2014,** *111* (48), 17050.

62.   Vajeeston, P.; Ravindran, P.; Ravi, C.; Asokamani, R., Electronic structure, bonding, and ground-state properties of AlB2-type transition-metal diborides. *Physical Review B* **2001,** *63* (4), 045115.

63.   Miao, N.; Sa, B.; Zhou, J.; Sun, Z., Theoretical investigation on the transition-metal borides with Ta3B4-type structure: A class of hard and refractory materials. *Computational Materials Science* **2011,** *50* (4), 1559-1566.

64.   Kotzott, D.; Ade, M.; Hillebrecht, H., Synthesis and crystal structures of α- and β-modifications of Cr2IrB2 containing 4-membered B4 chain fragments, the τ-boride Cr7.9Ir14.1B6 and orthorhombic Cr2B. *Solid State Sciences* **2008,** *10* (3), 291-302.

65.   Yeh, C. L.; Chen, W. H., Preparation of niobium borides NbB and NbB2 by self-propagating combustion synthesis. *Journal of Alloys and Compounds* **2006,** *420* (1), 111-116.

66.   Yeh, C. L.; Wang, H. J., Combustion synthesis of vanadium borides. *Journal of Alloys and Compounds* **2011,** *509* (7), 3257-3261.

67.   Morris, M. A.; Morris, D. G., Ball-milling of elemental powders—compound formation and/or amorphization. *Journal of materials science* **1991,** *26* (17), 4687-4696.

68.   Iizumi, K.; Kudaka, K.; Maezawa, D.; Sasaki, T., Mechanochemical synthesis of chromium borides. *Journal Of The Ceramic Society Of Japan* **1999,** *107* (1245), 491-493.

69.   Decker, B. F.; Kasper, J. S., The crystal structure of TiB. *Acta Crystallographica* **1954,** *7* (1), 77-80.

70.   Al-Zain, O. A.; Soliyman, A. M. R., Synthesis and Characterization of Fe, Ru and Os Metal Borides. *J Nanomed Nanotechnol* **2017,** *8* (469), 2.

71.   Jothi, P. R.; Yubuta, K.; Fokwa, B. P. T., A Simple, General Synthetic Route toward Nanoscale Transition Metal Borides. *Advanced Materials* **2018,** *30* (14), 1704181.

72.   Hassanzadeh-Tabrizi, S. A.; Davoodi, D.; Beykzadeh, A. A.; Salahshour, S., Fast mechanochemical combustion synthesis of nanostructured vanadium boride by a magnesiothermic reaction. *Ceramics International* **2016,** *42* (1, Part B), 1812-1816.

73.   Balcı, Ö.; Ağaoğulları, D.; Öveçoğlu, M. L.; Duman, İ., Synthesis of niobium borides by powder metallurgy methods using Nb2O5, B2O3 and Mg blends. *Transactions of Nonferrous Metals Society of China* **2016,** *26* (3), 747-758.

74.   Chen, B.; Yang, L.; Heng, H.; Chen, J.; Zhang, L.; Xu, L.; Qian, Y.; Yang, J., Additive-assisted synthesis of boride, carbide, and nitride micro/nanocrystals. *Journal of Solid State Chemistry* **2012,** *194*, 219-224.

75.   Juarez-Arellano, E. A.; Winkler, B.; Vogel, S. C.; Senyshyn, A.; Kammler, D. R.; Avalos-Borja, M., In situ observation of the reaction of scandium and carbon by neutron diffraction. *Journal of Alloys and Compounds* **2011,** *509* (1), 1-5.

76.   Niyomwas, S., Synthesis and Characterization of TiC and TiC-Al$_2$O$_3$Composite from Wood Dust by Self-Propagating High Temperature Synthesis. *Energy Procedia* **2011,** *9*, 522-531.

77.   Feng, X.; Bai, Y.-J.; Lü, B.; Wang, C.-G.; Liu, Y.-X.; Geng, G.-L.; Li, L., Easy synthesis of TiC nanocrystallite. *Journal of Crystal Growth* **2004,** *264* (1), 316-319.

78.   Hassanzadeh-Tabrizi, S. A.; Davoodi, D.; Beykzadeh, A. A.; Chami, A., Fast synthesis of VC and V$_2$C nanopowders by the mechanochemical combustion method. *International Journal of Refractory Metals and Hard Materials* **2015,** *51*, 1-5.

79.   Hallén, A.; Linnarsson, M., Ion implantation technology for silicon carbide. *Surface and Coatings Technology* **2016,** *306*, 190-193.

80.   Gogotsi, Y., Transition metal carbides go 2D. *Nature Materials* **2015,** *14*, 1079.

81.   Wang, Q.; German, K. E.; Oganov, A. R.; Dong, H.; Feya, O. D.; Zubavichus, Y. V.; Murzin, V. Y., Explaining stability of transition metal carbides - and why TcC does not exist. *RSC Advances* **2016,** *6* (20), 16197-16202.

82.   Hammer, B.; Norskov, J. K., Why gold is the noblest of all the metals. *Nature* **1995,** *376*, 238.

83.   Brazhkin, V. V., High-pressure synthesized materials: treasures and hints. *High Pressure Research* **2007,** *27* (3), 333-351.

84.   Zou, P.; Xu, G.; Wang, S.; Chen, P.; Huang, F., Effect of high pressure sintering and annealing on microstructure and thermoelectric properties of nanocrystalline Bi2Te2. 7Se0. 3 doped with Gd. *Progress in Natural Science: Materials International* **2014,** *24* (3), 210-217.

85.   Yang, M.; Su, T.; Zhou, D.; Zhu, H.; Li, S.; Hu, M.; Hu, Q.; Ma, H.; Jia, X., High-pressure synthesis and thermoelectric performance of tellurium doped with bismuth. *Journal of Materials Science* **2017,** *52* (17), 10526-10532.

86.   Gilioli, E.; Ehm, L., High pressure and multiferroics materials: a happy marriage. *IUCrJ* **2014,** *1* (6), 590-603.

87.   Matizamhuka, W., High-Pressure High-Temperature (HPHT) Synthesis of Functional Materials. In *Sintering of Functional Materials*, IntechOpen: 2017.

88.   Li, X.; Hermann, A.; Peng, F.; Lv, J.; Wang, Y.; Wang, H.; Ma, Y., Stable Lithium Argon compounds under high pressure. *Scientific Reports* **2015,** *5*, 16675.

89.   Dong, X.; Oganov, A. R.; Goncharov, A. F.; Stavrou, E.; Lobanov, S.; Saleh, G.; Qian, G.-R.; Zhu, Q.; Gatti, C.; Deringer, V. L.; Dronskowski, R.; Zhou, X.-F.; Prakapenka, V. B.; Konôpková, Z.; Popov, I. A.; Boldyrev, A. I.; Wang, H.-T., A stable compound of helium and sodium at high pressure. *Nature Chemistry* **2017,** *9*, 440.

90.   Somayazulu, M.; Dera, P.; Smith, J.; Hemley, R. J., Structure and stability of solid Xe(H2)n. *The Journal of Chemical Physics* **2015,** *142* (10), 104503.

91.   Zhang, W.; Oganov, A. R.; Zhu, Q.; Lobanov, S. S.; Stavrou, E.; Goncharov, A. F., Stability of numerous novel potassium chlorides at high pressure. *Scientific reports* **2016,** *6*, 26265-26265.

92.   Bykov, M.; Bykova, E.; Aprilis, G.; Glazyrin, K.; Koemets, E.; Chuvashova, I.; Kupenko, I.; McCammon, C.; Mezouar, M.; Prakapenka, V.; Liermann, H. P.; Tasnádi, F.; Ponomareva, A. V.; Abrikosov, I. A.; Dubrovinskaia, N.; Dubrovinsky, L., Fe-N system at high pressure reveals a compound featuring polymeric nitrogen chains. *Nature Communications* **2018,** *9* (1), 2756.

93.   Fu, Y.; Du, X.; Zhang, L.; Peng, F.; Zhang, M.; Pickard, C. J.; Needs, R. J.; Singh, D. J.; Zheng, W.; Ma, Y., High-Pressure Phase Stability and Superconductivity of Pnictogen Hydrides and Chemical Trends for Compressed Hydrides. *Chemistry of Materials* **2016,** *28* (6), 1746-1755.

94.   Drozdov, A. P.; Eremets, M. I.; Troyan, I. A.; Ksenofontov, V.; Shylin, S. I., Conventional superconductivity at 203 kelvin at high pressures in the sulfur hydride system. *Nature* **2015,** *525*, 73.

95.   Hemley, R.; Ahart, M.; Liu, H.; Somayazulu, M., *Road to Room-Temperature Superconductivity: Tc above 260 K in Lanthanum Superhydride under Pressure*. 2019.

96.   Geballe, Z.; Liu, H.; Mishra, A.; Ahart, M.; Somayazulu, M.; Meng, Y.; Baldini, M.; Hemley, R., Synthesis and Stability of Lanthanum Superhydrides. *Angewandte Chemie* **2017,** *130*.

97.   Kumar, N. R. S.; Shekar, N. V. C.; Sharat, C.; Joysurya, B.; Divakar, R.; Sahu, P. C., Synthesis of novel Ru2C under high pressure–high temperature conditions. *Journal of Physics: Condensed Matter* **2012,** *24* (36), 362202.

98.   Kumar, N. R. S.; Sharat, C.; Amirthapandian, S.; Shekar, N. V. C.; Sahu, P. C., Investigations of the high pressure synthesized osmium carbide by experimental and computational techniques. *Materials Research Express* **2015,** *2* (1), 016503.

99.   Ono, S.; Kikegawa, T.; Ohishi, Y., A high-pressure and high-temperature synthesis of platinum carbide. *Solid State Communications* **2005,** *133* (1), 55-59.

100.   Yasui, N.; Sougawa, M.; Hirai, M.; Yamamoto, K.; Okada, T.; Yamazaki, D.; Kojima, Y.; Ohfuji, H.; Kunitsugu, S.; Takarabe, K.; Ahuja, R., *High-pressure and high-temperature synthesis of rhenium carbide using rhenium and nanoscale amorphous two-dimensional carbon nitride*. 2015; Vol. 2, p 1076702.

101.   Bundy, F. P.; Hall, H. T.; Strong, H. M.; Wentorf, R. H., Man-Made Diamonds. *Nature* **1955,** *176* (4471), 51-55.

102.   Hazen, R. M., *The New Alchemists: Breaking Through the Barriers of High Pressure*. Times Books: 1993.

103.   Eremets, M. I., *High Pressure Experimental Methods*. Oxford University Press: 1996.

104.   Bridgman, P. W., New high pressures reached with multiple apparatus. *Physical Review* **1940,** *57* (4), 342.

105.   Bridgman, P. W., Recent work in the field of high pressures. *Reviews of Modern Physics* **1946,** *18* (1), 1.

106.   Sherman, W. F.; Stadtmuller, A. A., *Experimental Techniques in High-Pressure Research*. John Wiley & Sons Australia, Limited: 1987.

107.   Wang, Y.; Uchida, T.; Westferro, F.; Rivers, M.; Nishiyama, N.; Gebhardt, J.; Lesher, C.; R. Sutton, S., High-pressure x-ray tomography microscope: Synchrotron computed microtomography at high pressure and temperature. *Review of Scientific Instruments* **2005,** *76*.

108.   Prigogine, I.; Rice, S. A., *Advances in chemical physics*. John Wiley & Sons: 2003; Vol. 125.

109.   Hall, H. T., Ultra‐High‐Pressure, High‐Temperature Apparatus: the``Belt''. *Review of Scientific Instruments* **1960,** *31* (2), 125-131.

110.   Bundy, F., Direct conversion of graphite to diamond in static pressure apparatus. *The Journal of Chemical Physics* **1963,** *38* (3), 631-643.

111.   Jayaraman, A., Diamond anvil cell and high-pressure physical investigations. *Reviews of Modern Physics* **1983,** *55* (1), 65-108.

112.   Dewaele, A.; Loubeyre, P.; Occelli, F.; Marie, O.; Mezouar, M., Toroidal diamond anvil cell for detailed measurements under extreme static pressures. *Nature Communications* **2018,** *9* (1), 2913.

113.   Letoullec, R.; Pinceaux, J. P.; Loubeyre, P., The membrane diamond anvil cell: A new device for generating continuous pressure and temperature variations. *High Pressure Research* **1988,** *1* (1), 77-90.

114.   Sahu, P. C.; N. V, C. S., High pressure research on materials: 1. Production and measurement of high pressures in the laboratory. *Resonance* **2007,** *12*.

115.   N.V.Ch, r. S., P.Ch.Sahu, K.Govinda Rajan, Laser-Heated Diamond-Anvil Cell (LHDAC) in Materials Science Research. *J. Mater. Sci. Technol.* **2003,** *19* (06), 518-525.

116.   Mao, H. K.; Bell, P. M.; Hadidiacos, C., Experimental Phase Relations of Iron to 360 Kbar, 1400°C, Determined in an Internally Heated Diamond-Anvil Apparatus. *High‑Pressure Research in Mineral Physics: A Volume in Honor of Syun‑iti Akimoto* **1987**, 135-138.

117.   Friedrich, A.; Winkler, B.; Juarez-Arellano, E. A.; Bayarjargal, L., Synthesis of Binary Transition Metal Nitrides, Carbides and Borides from the Elements in the Laser-Heated Diamond Anvil Cell and Their Structure-Property Relations. *Materials (Basel, Switzerland)* **2011,** *4* (10), 1648-1692.

118.   McMillan, P. F., Chemistry of materials under extreme high pressure-high-temperature conditions. *Chemical Communications* **2003,** (8), 919-923.

119.   A. Bassett, W., The birth and development of laser heating in diamond anvil cells. *Review of Scientific Instruments* **2001,** *72*, 1270-1272.

120.   Schubert, G., *Treatise on geophysics*. Elsevier: 2015.

121.   Klotz, S.; Chervin, J. C.; Munsch, P.; Le Marchand, G., Hydrostatic limits of 11 pressure transmitting media. *Journal of Physics D: Applied Physics* **2009,** *42* (7), 075413.

122.   http://www.rrcat.gov.in/technology/accel/indus2.html#.

123.   Yang, L., *Recent Progress in Silicon-based Spintronic Materials*. 2015.

124.   Sekar, M.; Chandra Shekar, N. V.; Appalakondaiah, S.; Shwetha, G.; Vaitheeswaran, G.; Kanchana, V., Structural stability of ultra-incompressible Mo2B: A combined experimental and theoretical study. *Journal of Alloys and Compounds* **2016,** *654*, 554-560.

125.   Kvashnin, A. G.; Oganov, A. R.; Samtsevich, A. I.; Allahyari, Z., Computational Search for Novel Hard Chromium-Based Materials. *The Journal of Physical Chemistry Letters* **2017,** *8* (4), 755-764.

126.   Vajeeston, P.; Ravindran, P.; Ravi, C.; Asokamani, R., Electronic structure, bonding, and ground-state properties of AlB2-type transition-metal diborides. *Physical Review B* **2001,** *63* (4), 045115-12.

127.   Yao, T.; Wang, Y.; Li, H.; Lian, J.; Zhang, J.; Gou, H., A universal trend of structural, mechanical and electronic properties in transition metal (M=V, Nb, and Ta) borides: First-principle calculations. *Computational Materials Science* **2012,** *65*, 302-308.

128.   Yan, H.-y.; Wei, Q.; Chang, S.-m.; Guo, P., A first-principle calculation of structural, mechanical and electronic properties of titanium borides. *Transactions of Nonferrous Metals Society of China* **2011,** *21* (7), 1627-1633.

129.   E., G. D. *Sandia National Laboratories Report 91-0147, UC-704*; Sandia National l.aboratories,

Albuquerque, NM, USA, 1991; p 55.

130.   Gilman, J. J.; Roberts, B. W., Elastic Constants of TiC and TiB2. *Journal of Applied Physics* **1961,** *32* (7), 1405-1405.

131.   Wright, S., Estimation of single-crystal elastic constants from textured polycrystal measurements. *Journal of Applied Crystallography* **1994,** *27* (5), 794-801.

132.   Wiley, D. E.; Manning, W. R.; Hunter, O., Elastic properties of polycrystalline TiB2, ZrB2 and HfB2 from room temperature to 1300 °K. *Journal of the Less Common Metals* **1969,** *18* (2), 149-157.

133.   P.S Spoor, J. D. M., M.J Pan, D.J Green, J. R. Hellmann and T. Tanaka, Elastic constants and crystal anisotropy of titanium diboride. *Applied Physics Letters* **1997,** *70* (15), 1959-1961.

134.   Dodd, S. P.; Cankurtaran, M.; Saunders, G. A.; James, B., Ultrasonic determination of the temperature and hydrostatic pressure dependences of the elastic properties of ceramic titanium diboride. *Journal of Materials Science* **2001,** *36* (16), 3989-3996.

135.   Dandekar, D. P.; Benfanti, D. C., Strength of titanium diboride under shock wave loading. *Journal of Applied Physics* **1993,** *73* (2), 673-679.

136.   Gust, W. H.; Holt, A. C.; Royce, E. B., Dynamic yield, compressional, and elastic parameters for several lightweight intermetallic compounds. *Journal of Applied Physics* **1973,** *44* (2), 550-560.

137.   BSKNR, S.; Sekar, M.; Chandra Shekar, N., A novel micro-focus high pressure high temperature x-ray diffraction technique. *J. Instrum. Soc. India* **2016,** *46*, 75-7.

138.   Hammersley, A. P.; Svensson, S. O.; Hanfland, M.; Fitch, A. N.; Hausermann, D., Two-dimensional detector software: From real detector to idealised image or two-theta scan. *High Pressure Research* **1996,** *14* (4-6), 235-248.

139.   Rodríguez-Carvajal, J., FullProf. *CEA/Saclay, France* **2001**.

140.   Momma, K.; Izumi, F., VESTA 3 for three-dimensional visualization of crystal, volumetric and morphology data. *Journal of applied crystallography* **2011,** *44* (6), 1272-1276.

141.   Kresse, G.; Furthmüller, J., Efficient iterative schemes for ab initio total-energy calculations using a plane-wave basis set. *Physical Review B* **1996,** *54* (16), 11169-11186.

142.   Ceperley, D. M.; Alder, B. J., Ground State of the Electron Gas by a Stochastic Method. *Physical Review Letters* **1980,** *45* (7), 566-569.

143.   Perdew, J. P.; Zunger, A., Self-interaction correction to density-functional approximations for many-electron systems. *Physical Review B* **1981,** *23* (10), 5048-5079.

144.   Perdew, J. P.; Burke, K.; Ernzerhof, M., Generalized Gradient Approximation Made Simple. *Physical Review Letters* **1996,** *77* (18), 3865-3868.

145.   Chung, H.-Y.; B Weinberger, M.; B Levine, J.; Cumberland, R.; Kavner, A.; Yang, J.-M.; H Tolbert, S.; Kaner, R., *Synthesis of Ultra-Incompressible Superhard Rhenium Diboride at Ambient Pressure*. 2007; Vol. 316, p 436-9.

146.   Ma, S.; Bao, K.; Tao, Q.; Li, L.; Huang, Y.; Huang, X.; Zhao, Y.; Xu, C.; Zhu, P.; Cui, T., Revealing the Unusual Rigid Boron Chain Substructure in Hard and Superconductive Tantalum Monoboride. *Chemistry – A European Journal* **2019,** *25* (19), 5051-5057.

147.   N. JAHAN, M. A. A., A THEORETICAL STUDY OF ELASTIC, ELECTRONIC, OPTICAL AND THERMODYNAMIC PROPERTIES OF AlB$_2$ AND TaB$_2$. *Bangladesh Journal of Physics* **2014,** *15*, 93-103.

148.   Zhang, J.-D.; Cheng, X.-L.; Li, D.-H., First-principles calculations of structural, elastic and electronic properties of TaB2 with AlB2 structure under high pressure. *Computational Materials Science* **2010,** *50* (2), 474-478.

149.   Zhao, E.; Meng, J.; Ma, Y.; Wu, Z., Phase stability and mechanical properties of tungsten borides from first principles calculations. *Physical Chemistry Chemical Physics* **2010,** *12* (40), 13158-13165.

150.   Liang, Y.; Yuan, X.; Zhang, W., Thermodynamic identification of tungsten borides. *Physical Review B* **2011,** *83* (22), 220102.

151.   Dong, H.; Dorfman, S. M.; Chen, Y.; Wang, H.; Wang, J.; Qin, J.; He, D.; Duffy, T. S., Compressibility and strength of nanocrystalline tungsten boride under compression to 60 GPa. *Journal of Applied Physics* **2012,** *111* (12), 123514.

152.   Qi, C.-J.; Feng, J.; Zhou, R.-F.; Jiang, Y.-H.; Zhou, R., First Principles Study on the Stability and Mechanical Properties of MB (M=V, Nb and Ta) Compounds. *Chinese Physics Letters* **2013,** *30* (11), 117101.

153.   Angel, R. J., Equations of State. *Reviews in Mineralogy and Geochemistry* **2000,** *41* (1), 35-59.

154.   Okada, S.; Kudou, K.; Higashi, I.; Lundström, T., Single crystals of TaB, Ta5B6, Ta3B4 and TAB2, as obtained from high-temperature metal solutions, and their properties. *Journal of Crystal Growth* **1993,** *128* (1, Part 2), 1120-1124.

155.   TaB$_2$ ICDD PDF no. 00-038-1462. *TaB$_2$ ICDD PDF no. 00-038-1462*.

156.   Chen, H.-H.; Bi, Y.; Cheng, Y.; Ji, G.; Cai, L., Elastic stability and electronic structure of tantalum boride investigated via first-principles density functional calculations. *Journal of Physics and Chemistry of Solids* **2012,** *73* (10), 1197-1202.

157.   Arya, A.; Carter, E. A., Structure, bonding, and adhesion at the TiC(100)/Fe(110) interface from first principles. *The Journal of Chemical Physics* **2003,** *118* (19), 8982-8996.

158.   Kittel, C., *INTRODUCTION TO SOLID STATE PHYSICS, 7TH ED*. Wiley India Pvt. Limited: 2007.

159.   Mouhat, F.; Coudert, F.-X., Necessary and sufficient elastic stability conditions in various crystal systems. *Physical Review B* **2014,** *90* (22), 224104.

160.   Voigt, W., *Lehrbuch der kristallphysik*. Teubner Leipzig: 1928; Vol. 962.

161.   Pugh, S., XCII. Relations between the elastic moduli and the plastic properties of polycrystalline pure metals. *The London, Edinburgh, and Dublin Philosophical Magazine and Journal of Science* **1954,** *45* (367), 823-843.

162.   Hadi, M. A.; Nasir, M. T.; Roknuzzaman, M.; Rayhan, M. A.; Naqib, S. H.; Islam, A., First‑principles prediction of mechanical and bonding characteristics of new T2 superconductor Ta5GeB2. *physica status solidi (b)* **2016,** *253* (10), 2020-2026.

163.   Tian, D.-C.; Wang, X.-B., Electronic structure and equation of state of TiB2. *Journal of Physics: Condensed Matter* **1992,** *4* (45), 8765-8772.

164.   Perottoni, C. A.; Pereira, A. S.; Jornada, J. A. H. d., Periodic Hartree-Fock linear combination of crystalline orbitals calculation of the structure, equation of state and elastic properties of titanium diboride. *Journal of Physics: Condensed Matter* **2000,** *12* (32), 7205-7222.

165.   Larson, A. C., & Von Dreele, R. B. *General Structure Analysis System (GSAS)*; Los Alamos National Laboratory LAUR: 2004; pp 86-748.

166.   Toby, B., EXPGUI, a graphical user interface for GSAS. *Journal of Applied Crystallography* **2001,** *34* (2), 210-213.

167.   TiB2. *ICDD pdf 00-035-0741.*

168.   Angel, R. J., Equations of State. *Reviews in Mineralogy and Geochemistry* **2000,** *41* (1), 35.

169.   Pereira, A. S.; Perottoni, C. A.; Jornada, J. A. H. d.; Léger, J. M.; Haines, J., Compressibility of AlB 2 -type transition metal diborides. *Journal of Physics: Condensed Matter* **2002,** *14* (44), 10615-10618.

170.   Jorgensen, J. D.; Hinks, D. G.; Short, S., Lattice properties of MgB_2 versus temperature and pressure. *Physical Review B* **2001,** *63* (22), 224522.

171.   Halevy, I.; Beck, A.; Yaar, I.; Kahane, S.; Levy, O.; Auster, E.; Ettedgui, H.; Caspi, E. N.; Rivin, O.; Berant, Z.; Hu, J., XRD, TDPAC and LAPW study of Hf10B2 under high pressure. *Hyperfine Interactions* **2007,** *177* (1), 57-64.

172.   Meng, X.-X.; Fan, J.; Bao, K.; Li, F.-F.; Huang, X.-L.; Li, Y.; Tian, F.-B.; Duan, D.-F.; Jin, X.-L.; Zhu, P.-W.; He, Z.; Zhou, Q.; Gao, C.-X.; Liu, B.-B.; Cui, T., Structural stability and electrical properties of AlB 2 -type MnB 2 under high pressure. *Chinese Physics B* **2014,** *23* (1), 016102-5.

173.   Loa, I.; Kunc, K.; Syassen, K.; Bouvier, P., Crystal structure and lattice dynamics of AlB_2 under pressure and implications for MgB_2. *Physical Review B* **2002,** *66* (13), 134101.

174.   Milman, V.; Warren, M. C., Elastic properties of TiB 2 and MgB 2. *Journal of Physics: Condensed Matter* **2001,** *13* (24), 5585-5595.

175.   Grady, D. E. Sandia National Lboratories: Albuquerque, NM, USA, 1991; p 55.

176.   Marsh, S. P., LASL Shock Hugoniot Data. University of California Press: Berkeley, Los Angeles, London, 1980; p 354.

177. Okamoto, N. L.; Kusakari, M.; Tanaka, K.; Inui, H.; Yamaguchi, M.; Otani, S., Temperature dependence of thermal expansion and elastic constants of single crystals of ZrB2 and the suitability of ZrB2 as a substrate for GaN film. *Journal of Applied Physics* **2002,** *93* (1), 88-93.

178. Chen, Y.; He, D.; Qin, J.; Kou, Z.; Bi, Y., Ultrasonic and hardness measurements for ultrahigh pressure prepared WB ceramics. *International Journal of Refractory Metals and Hard Materials* **2011,** *29* (2), 329-331.

179. Boer, F. R., *Cohesion in metals: transition metal alloys*. North-Holland: 1988.

180. De-Cheng, T.; Xiao-Bing, W., Electronic structure and equation of state of TiB 2. *Journal of Physics: Condensed Matter* **1992,** *4* (45), 8765-8772.

181. Chandra Shekar, N. V.; Kathirvel, V.; Sahu, P. C., Structural stability, phase transformations and band-tuning of actinide and rare earth based intermetallics under high pressure: a perspective. *Indian Journal of Physics* **2010,** *84* (5), 485-499.

182. Segall, M. D.; Lindan, P. J. D.; Probert, M. J.; Pickard, C. J.; Hasnip, P. J.; Clark, S. J.; Payne, M. C., First-principles simulation: ideas, illustrations and the CASTEP code. *Journal of Physics: Condensed Matter* **2002,** *14* (11), 2717-2744.

183. Clark Stewart, J.; Segall Matthew, D.; Pickard Chris, J.; Hasnip Phil, J.; Probert Matt, I. J.; Refson, K.; Payne Mike, C., First principles methods using CASTEP. In *Zeitschrift für Kristallographie - Crystalline Materials*, 2005; Vol. 220, p 567.

184. Payne, M. C.; Teter, M. P.; Allan, D. C.; Arias, T. A.; Joannopoulos, J. D., Iterative minimization techniques for ab initio total-energy calculations: molecular dynamics and conjugate gradients. *Reviews of Modern Physics* **1992,** *64* (4), 1045-1097.

185. Blaha, P.; Schwarz, K.; Madsen, G. K. H.; Kvasnicka, D.; Luitz, J., WIEN2k, An Augmented Plane Wave Plus Local Orbitals Program for Calculating Crystal Properties (Vienna University of Technology, Austria, 2001). *There is no corresponding record for this reference* **2002**.

186. Blaha, P.; Schwarz, K.; Sorantin, P.; Trickey, S. B., Full-potential, linearized augmented plane wave programs for crystalline systems. *Computer Physics Communications* **1990,** *59* (2), 399-415.

187. Wang, M., The investigation of dependences of mechanical and electronic properties of TiB2on pressure using the first-principles method. *Physica Scripta* **2014,** *89* (11), 115702.

188. Shwetha, G.; Aparajita, A. N. A.; Chandra, S.; Chandra Shekar, N. V.; Kalavathi, S., Bond length anomaly in TiB2 at high pressure: first principles calculations. *Materials Research Express* **2018,** *6* (2), 026531.

189. Toth, L. E., *Transition metal carbides and nitrides*. Academic Press: 1971.

190. Djurovic, D.; Hallstedt, B.; von Appen, J.; Dronskowski, R., Thermodynamic assessment of the Mn–C system. *Calphad* **2010,** *34* (3), 279-285.

191.	Kroupa, A., Modelling of phase diagrams and thermodynamic properties using Calphad method – Development of thermodynamic databases. *Computational Materials Science* **2013,** *66*, 3-13.

192.	Subramanian, N.; N. V, C. S.; Kumar, S.; Sahu, P. C., *Development of laser-heated diamond anvil cell facility for synthesis of novel materials*. 2006; Vol. 91, p 175-182.

193.	Sekar, M.; Kumar, N. R. S.; Sahu, P. C.; Chandra Shekar, N. V.; Subramanian, N., Cryogenic gas loading in a Mao–Bell-type diamond anvil cell for high pressure-high temperature investigations. *Review of Scientific Instruments* **2008,** *79* (7), 076103.

194.	*$Mn_{23}C_6$ Crystal Structure: Datasheet from "PAULING FILE Multinaries Edition – 2012" in SpringerMaterials*, Springer-Verlag Berlin Heidelberg & Material Phases Data System (MPDS), Switzerland & National Institute for Materials Science (NIMS), Japan.

195.	Mn_3C: ICDD PDF No. 04-004-3127.

196.	*Mn_7C_3 Crystal Structure: Datasheet from "PAULING FILE Multinaries Edition – 2012" in SpringerMaterials* Springer-Verlag Berlin Heidelberg & Material Phases Data System (MPDS), Switzerland & National Institute for Materials Science (NIMS), Japan.

197.	Mn_5C_2 : ICDD PDF No. 04-007-1125.

198.	Barron, A. R., Physical methods in chemistry and nano science. **2015**.

199.	Togo, A.; Oba, F.; Tanaka, I., First-principles calculations of the ferroelastic transition between rutile-type and $CaCl_2$-type SiO_2 at high pressures. *Physical Review B* **2008,** *78* (13), 134106.

200.	Kresse, G.; Hafner, J., Ab initio molecular dynamics for liquid metals. *Physical Review B* **1993,** *47* (1), 558-561.

201.	Guillermet, A. F.; Grimvall, G., Cohesive properties and vibrational entropy of 3d transition-metal compounds: MX (NaCl) compounds (X=C, N, O, S), complex carbides, and nitrides. *Physical review. B, Condensed matter* **1989,** *40* (15), 10582-10593.

202.	Haglund, J.; Grimvall, G.; Jarlborg, T.; Guillermet, A. F., Band structure and cohesive properties of 3d-transition-metal carbides and nitrides with the NaCl-type structure. *Physical review. B, Condensed matter* **1991,** *43* (18), 14400-14408.

203.	Wang, J.; Chen, X.; Yang, N.; Fang, Z., Formation of NaCl-type Cr carbide by carbon ion implantation. *Applied Physics A* **1993,** *56* (4), 307-309.

204.	Cusenza, S.; Schaaf, P., Formation and characterization of NaCl-type FeC. *Materials Letters* **2009,** *63* (16), 1445-1447.

205.	Juarez-Arellano, E.; Winkler, B.; Bayarjargal, L.; Friedrich, A.; Milman, V.; Kammler, D.; Clark, S.; Yan, J.; Koch-Müller, M.; Schroder, F.; Avalos-Borja, M., *Formation of scandium carbides and scandium oxycarbide from the elements at high-(P, T) conditions*. 2010; Vol. 183, p 975-983.

206.	Christensen, A., A neutron diffraction investigation on single crystals of titanium carbide, titanium nitride and zirconium nitride. *Acta Chem. Scand., Ser. A* **1975,** *29*, 2.

207. *VC Crystal Structure: Datasheet from "PAULING FILE Multinaries Edition – 2012"* *in SpringerMaterials* Springer-Verlag Berlin Heidelberg & Material Phases Data System (MPDS), Switzerland & National Institute for Materials Science (NIMS), Japan.

208. Li, Q.; Zhang, X.; Liu, H.; Wang, H.; Zhang, M.; Li, Q.; Ma, Y., Structural and Mechanical Properties of Platinum Carbide. *Inorganic Chemistry* **2014,** *53* (11), 5797-5802.

209. Aleksandra, V.; Carlo, R., Trends in bulk electron-structural features of rocksalt early transition-metal carbides. *Journal of Physics: Condensed Matter* **2010,** *22* (37), 375501.

210. Šimůnek, A., How to estimate hardness of crystals on a pocket calculator. *Physical Review B* **2007,** *75* (17), 172108.

211. Šimůnek, A.; Vackář, J., Hardness of Covalent and Ionic Crystals: First-Principle Calculations. *Physical Review Letters* **2006,** *96* (8), 085501.

212. *TiC Crystal Structure: Datasheet from "PAULING FILE Multinaries Edition – 2012"* *in SpringerMaterials*, Springer-Verlag Berlin Heidelberg & Material Phases Data System (MPDS), Switzerland & National Institute for Materials Science (NIMS), Japan.

213. Schmuecker, S.; Albert Clouser, D.; Kraus, T.; Leonard, B., *Synthesis of Metastable Chromium Carbide Nanomaterials and their Electrocatalytic Activity for the Hydrogen Evolution Reaction*. 2017; Vol. 46.

214. Zaslavskaya, L. V.; Ivanova, N. V.; Lashko, N. F., Separation of Alloyed Chromium Carbides of the Cr2C (Metastable) and Cr23C6 or Cr7C3 Types Isolated from Steels and Alloys. In *Chemical Properties and Analysis of Refractory Compounds / Khimicheskie Svoistva I Metody Analiza Tugoplavkikh Soedinenii / Химические Свойства И Методы Анализа Тугоплавких Соединений*, Samsonov, G. V., Ed. Springer US: Boston, MA, 1972; pp 68-71.

215. Wu, L.; Guo, X.; Zhang, J., *Abrasive Resistant Coatings—A Review*. 2014; Vol. 2, p 66-89.

216. Epprecht, W., CRYSTAL CHEMISTRY OF METAL CARBIDES AND THEIR IMPORTANCE IN METALLURGY. *Translated from Chimia* **1951,** *5*, 49-60.

217. Bouzy, E.; Buer-Grosse, E.; Le Caer, G., NaCl and filled Re3B-type structures for two metastable chromium carbides. *Philosophical Magazine B* **1993,** *68* (5), 619-638.

218. Bewilogua, K.; Heinitz, H.-J.; Rau, B.; Schulze, S., A chromium carbide phase with B1 structure in thin films prepared by ion plating. *Thin Solid Films* **1988,** *167* (1-2), 233-244.

219. Sekar, M.; Kumar, S.; Sahu, P. C.; N. V, C. S.; Natarajan, S., Cryogenic gas loading in a Mao-Bell-type diamond anvil cell for high pressure-high temperature investigations. *The Review of scientific instruments* **2008,** *79*, 076103.

220. Wierzbicki, M.; Jaworski, S.; Kutwin, M.; Grodzik, M.; Strojny, B.; Kurantowicz, N.; Zdunek, K.; Chodun, R.; Chwalibog, A.; Sawosz, E., Diamond, graphite, and graphene oxide nanoparticles decrease migration and invasiveness in glioblastoma cell lines by impairing extracellular adhesion. *International journal of nanomedicine* **2017,** *12*, 7241.

221. Wu, E., POWD, an interactive program for powder diffraction data interpretation and indexing. *Journal of Applied Crystallography* **1989,** *22* (5), 506-510.

222.   Fe3C - ICDD PDF 01-089-2005.

223.   Re$_3$N - ICDD PDF No.

 04-020-4353

224.   Friedrich, A.; Winkler, B.; Bayarjargal, L.; Morgenroth, W.; Juarez-Arellano, E. A.; Milman, V.; Refson, K.; Kunz, M.; Chen, K., Novel Rhenium Nitrides. *Physical Review Letters* **2010,** *105* (8), 085504.

225.   Ru$_2$C - ICDD PDF 04-019-7840.

226.   Nb$_2$C - ICDD PDF 01-077-9683.

227.   **Ta$_2$C - ICDD PDF 04-001-2147**.

228.   Re$_2$C - ICDD PDF 01-080-3301.

229.   Arpita Aparajita, A. N.; Sanjay Kumar, N. R.; Chandra, S.; Amirthapandian, S.; Shekar, N. V. C.; Sridhar, K., High-Pressure Synthesis of Manganese Monocarbide: A Potential Superhard Material. *Inorganic Chemistry* **2018**.

230.   Kempter, C. P.; Nadler, M. R., Preparation and Crystal Structures of RuC and OsC. *The Journal of Chemical Physics* **1960,** *33* (5), 1580-1581.

231.   Yang, J.; Gao, F., Hardness calculations of 5d transition metal monocarbides with tungsten carbide structure. *physica status solidi (b)* **2010,** *247* (9), 2161-2167.

232.   Schuster, J.; Rudy, E.; Nowotny, H., Die "MoC"-phase mit WC-struktur. *Monatshefte für Chemie/Chemical Monthly* **1976,** *107* (5), 1167-1176.

233.   KuO, K.; HÄGg, G., A New Molybdenum Carbide. *Nature* **1952,** *170* (4319), 245-246.

234.   MoC - ICDD PDF 00-008-0384.

235.   Mo$_{1.2}$ C$_{0.8}$ - ICDD PDF 04-006-2272.

236.   Kumar, N. R. S.; Chandra, S.; Amirthapandian, S.; Chandra Shekar, N. V.; Ch Sahu, P., Investigations of the high pressure synthesized osmium carbide by experimental and computational techniques. *Materials Research Express* **2015,** *2* (1), 016503.

237.   Sanjay Kumar, N. R.; Chandra Shekar, N. V.; Sahu, P. C., *Novel metastable form of ruthenium carbide at high pressure*. Bhabha Atomic Research Centre: India, 2011.

238.   Juarez-Arellano, E.; Winkler, B.; Friedrich, A.; Wilson, D.; Koch-Müller, M.; Knorr, K.; Vogel, S.; Wall, J.; Reiche, H.; Crichton, W.; Ortega, M.; Avalos-Borja, M., Reaction of rhenium and carbon at high pressures and temperatures. *Zeitschrift für Kristallographie* **2008,** *223*, 492-501.

239.   Venkateswaran, T.; Basu, B.; Golla, B. R.; Kim, D.-Y., Densification and Properties of Transition Metal Borides-Based Cermets Via Spark Plasma Sintering. *Journal of the European Ceramic Society* **2006,** *26*, 2431-2440.

240.   Telle, R.; Petzow, G., Strengthening and toughening of boride and carbide hard material composites. *Materials Science and Engineering: A* **1988,** *105-106*, 97-104.

241.	Atkinson, H. V.; Davies, S., Fundamental aspects of hot isostatic pressing: An overview. *Metallurgical and Materials Transactions A* **2000,** *31* (12), 2981-3000.

242.	Fahrenholtz, W. G.; Hilmas, G. E.; Zhang, S. C.; Zhu, S., Pressureless Sintering of Zirconium Diboride: Particle Size and Additive Effects. *Journal of the American Ceramic Society* **2008,** *91* (5), 1398-1404.

243.	Demirskyi, D.; Agrawal, D.; Ragulya, A., Tough ceramics by microwave sintering of nanocrystalline titanium diboride ceramics. *Ceramics International* **2014,** *40* (1, Part B), 1303-1310.

244.	Yeung, M. T.; Lei, J.; Mohammadi, R.; Turner, C. L.; Wang, Y.; Tolbert, S. H.; Kaner, R. B., Superhard Monoborides: Hardness Enhancement through Alloying in W1−xTaxB. *Advanced Materials* **2016,** *28* (32), 6993-6998.

245.	Takagi, K.-i.; Koike, W.; Momozawa, A.; Fujima, T., Effects of Cr on the properties of Mo2NiB2 ternary boride. *Solid State Sciences* **2012,** *14* (11), 1643-1647.

246.	Suresh, S.; Shenbag, N.; Moorthi, V., Aluminium-Titanium Diboride (Al-TiB2) Metal Matrix Composites: Challenges and Opportunities. *Procedia Engineering* **2012,** *38*, 89-97.

247.	Sahoo, S.; Majhi, J.; Patnaik, S.; Behera, A.; Sahoo, J. K.; Prasad Sahoo, B., Characterisation of Al-Si-TiB2 In-situ Composite Synthesised by Stir Casting Method. *Elixir Materials Science* **2017,** *113*, 49066-49069.